

# Effect of Cu and die geometry on the extrudability of AA6xxx Alloys

by

Xiaoying Wang

A thesis

presented to the University of Waterloo

in fulfillment of the

thesis requirement for the degree of

Doctor of Philosophy

in

Mechanical and Mechatronics Engineering

Waterloo, Ontario, Canada, 2023

© Xiaoying Wang 2023

## **Examining Committee membership**

The following served on the Examining Committee for this thesis. The decision of the Examining Committee is by majority vote.

External Examiner

Corbin Stephen, Ph.D., Adjunct Professor,  
Dalhousie University, Department of  
Mechanical engineering

Supervisor

Mary Wells, Ph.D., Professor, University of  
Waterloo, Department of Mechanical  
Engineering

Internal Member

Kaan Inal, Ph.D., Professor, University of  
Waterloo, Department of Mechanical  
Engineering

Adrian Gerlich, Ph.D., Professor, University  
of Waterloo, Department of Mechanical  
Engineering

Internal-external Member

Scott Walbridge, Ph.D., Professor, University  
of Waterloo, Department of Civil Engineering

## **Author's declaration**

I hereby declare that I am the sole author of this thesis. This is a true copy of the thesis, including any required final revisions, as accepted by my examiners.

I understand that my thesis may be made electronically available to the public.

## Abstract

A series of extrusion trials were conducted with AA6xxx aluminum alloys with different Copper (Cu) levels to understand the influence of alloy content, die geometry, extrusion ratio and extrusion process parameters (ram speed) on surface cracking and extrudability. In addition, a mathematical model was developed of the extrusion process to complement the experimental trials and provide quantitative information on the thermal mechanical history experienced by the material as a way to help understand the linkages between the extrusion process history, the microstructure formed and surface cracking.

The extrusion trials were conducted at Rio Tinto's facility in Jonquiere, Quebec using their instrumented extrusion press to produce an extruded rod. In these trials, dies with different die bearing geometries and different extrusion ratios were used and the ram speed was increased until surface cracking occurred. These trials were conducted for two (0.6% and 0.9%) of the three different compositions of AA6xxx aluminum alloys with different levels of Cu.

The experimental results indicate that die geometry significantly affects surface morphology and crack occurrence. The trials with dies with different die bearing geometries, reveals that choked dies enabled crack-free extrusion at higher speeds, particularly the 12 mm choked die with a 1° angle, outperforming the 25 mm flat die and zero-bearing die. The 35 mm choked die achieved crack-free extrusion even at maximum press speed, yielding smoother surfaces than the other dies. The trials using dies with a higher extrusion ratio generate surface cracks at a lower extrusion speed than the trials using dies with a lower extrusion ratio; this has to do with the higher temperatures that occur at these higher extrusion speeds due to a great amount of work imparted to the material. Finally, the material with higher Cu addition shows surface cracks occur at a lower extrusion speed compared to the material with lower Cu addition.

The mathematical model of the extrusion process was developed using the commercial Finite Element Method (FEM) package DEFORM™ 2D. The results from the model predictions were verified by comparing them to the measured extrusion load and temperature. Using a combination of model results and experimental measurements a threshold was determined by analyzing the tensile stress and temperature on the extrudate surface, beyond which surface cracking occurs for different die geometries. This threshold can also be applied to the effect of Cu on the surface cracking. However, for the effect of Cu, the temperature in the extrusion process plays a more important role in surface cracking occurrence.

Finally, the extrusion limit diagrams were also constructed based on both the simulation results and the extrusion trial data. The extrusion limit diagram shows the influence of the die bearing geometry, extrusion ratio and Cu content and provide guidance for choosing appropriate extrusion parameters for future studies.

## **Acknowledgements**

First, I want to convey my gratitude to Professor Mary Wells, my supervisor, for her encouragement and support during the entire Ph.D. journey. I deeply appreciate her assistance, guidance, trust, and patience. Without her invaluable assistance, I would not have been able to make this extensive journey on my own.

I would also like to express my gratitude to Professor Warren Poole from the University of British Columbia and Dr. Nick Parson from Rio Tinto Alcan for their invaluable assistance and support. Furthermore, I want to thank Dr. Zhijun Zhang, from the University of British Columbia, for helping me with sample preparation and conducting microscopic analyses.

I'm also appreciative of the financial support extended by NSERC. Additionally, I extend my thanks to the dedicated team at the Arvida Research and Development Center (ARDC) in Jonquière, QC. They conducted all the extrusion trials, supplied the samples for subsequent analysis, and conducted the metallography analysis.

I would like to thank Dr. Yu Wang, a fellow member of my research group, deserves my gratitude for his invaluable assistance in numerical simulations. I am thankful for Dr. Shehryar Khan's support and guidance in the final year of my study. I am also appreciative of Mark Whitney and Jared Uramowski for their assistance with the hot compression test. Dr. Yuquan Ding and the team at Watlab were incredibly helpful in the field of scanning electron microscopy (SEM).

I would like to extend my heartfelt thanks to the staff in the Mechanical and Mechatronics Engineering department at the University of Waterloo.

Finally, I am grateful for my husband and kids, my parents and brother and sisters for their support and encouragement during this long journey.

# Table of Contents

<b>Examining Committee membership.....</b>	<b>ii</b>
<b>Author’s declaration.....</b>	<b>iii</b>
<b>Abstract.....</b>	<b>iv</b>
<b>Acknowledgements.....</b>	<b>vi</b>
<b>List of Figures.....</b>	<b>xi</b>
<b>List of Tables .....</b>	<b>xix</b>
<b>Chapter 1 Introduction .....</b>	<b>1</b>
<b>Chapter 2 Literature Review.....</b>	<b>6</b>
2.1 Extrusion process of AA6xxx aluminum alloys.....	6
2.1.1 Extrusion process .....	6
2.1.2 Intermetallic phases formation in DC casting.....	9
2.1.3 Homogenization.....	11
2.2 Material flow and microstructure during extrusion.....	15
2.3 Extrusion defects .....	17
2.4 Extrusion limit diagram (ELD) .....	19
2.5 Hot deformation behavior and constitutive models for Al-Mg-Si-Cu alloys.....	24
2.5.1 Hot deformation behavior of AA6xxx aluminum alloys with Cu additions.....	24
2.5.2 Constitutive equations.....	26
2.6 Modeling of AA6xxx alloy extrusion process .....	29

2.7 Summary .....	31
<b>Chapter 3 Scope and Objectives .....</b>	<b>32</b>
<b>Chapter 4 Materials and Methodology.....</b>	<b>34</b>
4.1 Start material .....	34
4.2 Characterization.....	37
4.2.1 Differential Scanning Calorimetry.....	37
4.2.2 Hot compression test.....	38
4.3 Extrusion trials .....	42
4.3.1 Die configurations.....	43
4.3.2 Extrusion parameters .....	46
4.4 Mathematical model .....	48
4.4.1 Thermo-mechanical model .....	48
4.4.1.1 Finite Element formulation .....	49
4.4.1.2 Material properties .....	51
4.4.1.3 Boundary and initial conditions .....	53
4.4.1.4 Mesh size sensitivity .....	54
4.4.1.5 Friction coefficient justification .....	57
4.4.1.5.1 Friction coefficient of the flat die.....	58
4.4.1.5.2 Friction coefficient of the choked die.....	59
4.4.2 Experimental verification of the model .....	62
<b>Chapter 5 Results and Discussion .....</b>	<b>64</b>
5.1 Material properties .....	64
5.1.1 DSC.....	64



5.1.1.1	DSC results .....	64
5.1.1.2	Determination of the solidus temperature .....	67
5.1.2	Hot deformation behavior .....	71
5.1.2.1	Hot compression test .....	71
5.1.2.2	Constitutive model .....	74
5.2	Extrusion trials .....	78
5.2.1	Measured load and temperature .....	78
5.2.2	Extrudate characterization .....	80
5.2.2.1	Surface visual observation.....	89
5.2.2.1.1	Effect of extrusion ratio.....	89
5.2.2.1.2	Effect of die geometry .....	91
5.2.2.1.3	Effect of Cu .....	92
5.2.2.2	Surface observation by SEM.....	94
5.2.2.2.1	Effect of die geometry .....	94
5.2.2.2.2	Effect of Cu .....	101
5.2.2.3	PCG layer .....	104
5.2.2.3.1	Effect of die geometry .....	104
5.2.2.3.2	Effect of Cu .....	105
5.2.2.4	Surface roughness.....	107
5.2.2.4.1	Effect of die geometry .....	107
5.2.2.4.2	Effect of Cu .....	109
5.3	Model predictions.....	111
5.3.1	Effect of extrusion ratio .....	111

5.3.2 Effect of die geometry .....	116
5.3.3 Stress and temperature conditions that lead to cracking .....	123
5.4 Construction of extrusion limit diagram (ELD) .....	127
5.4.1 Effect of die geometries on ELD .....	131
5.4.2 Effect of extrusion ratio on ELD .....	136
5.4.3 Effect of Cu content on ELD .....	140
<b>Chapter 6 Summary, Conclusions, and Future Work .....</b>	<b>143</b>
6.1 Summary .....	143
6.2 Conclusions .....	144
6.3 Future Work .....	146
<b>References .....</b>	<b>148</b>

## List of Figures

Figure 1-1 Experimental data from Rio Tinto on the fracture strain vs. yield strength (YS) for a wide range of aluminum alloys, including AA6xxx and AA7xxx (WQ = water quench) [13].	5
Figure 2-1 Process steps related to manufacturing an extrusion part from aluminum [15].	7
Figure 2-2 Sketch of temperature history in each step of the extrusion process [15].	7
Figure 2-3 Typical grain structure of as-cast Al-Mg-Si alloy [17].	8
Figure 2-4 Microstructures of as-cast Al9Si0.5Mg alloys by SEM with (a) 0% Cu, (b) 0.4% Cu, (c) 0.85% Cu, and (d) 1.25% Cu. [19].	9
Figure 2-5 Chinese-script $\alpha$ -AlFeSi (left) and plate-like $\beta$ -AlFeSi (right) [25].	10
Figure 2-6 Microstructure of homogenized AA6005 at different cooling rate: (a) water quenching (~500000 °C/h); (b) air cooling (3000 °C/h); (c) furnace cooling (130 °C/h) [33].	13
Figure 2-7 The microstructure of AA6063 samples soaked at 540-560°C for different times: 2 hours, 4 hours and 6 hours [31].	14
Figure 2-8 Schematic diagram of a simple bar direct extrusion [41].	15
Figure 2-9 Material flow pattern of AA6061 during extrusion (DMZ indicates the dead metal zone) [42].	16
Figure 2-10 Four different zones formed during the extrusion of AA6082 [43].	17
Figure 2-11 Schematic Extrusion Limit Diagram (ELD) proposed by Hirst and Ursell [51].	20
Figure 2-12 Extrusion limit diagram of AA6063, AA5456, and AA2014 [52].	21
Figure 2-13 Extrusion limit diagram of AA7075 alloys with different Sc additions: 0% Sc (left), 0.11%Sc (middle), 0.3%Sc (right) [53].	22
Figure 2-14 ELD for small feeder (left) and big feeder (right) [54].	23
Figure 2-15 Measured stress-strain curves for Al-Mg-Si-Cu alloy at different temperatures and strain rates [64].	25
Figure 2-16 Measured flow stress curves of AA6061 at different deformation temperatures and strain rates [66].	26
Figure 2-17 Model predicted temperature and strain rate distribution during a bar extrusion [87].	30
Figure 4-1 Optical microstructure of as-cast materials with different Cu additions.	35
Figure 4-2 Constituent particles of as-cast materials characterized by FEG-SEM.	35

Figure 4-3 Thermal history of the homogenization process used on the billets (WQ = water quench). .....	36
Figure 4-4 Microstructure of the billets after homogenization with different Cu contents: (a)A611, (b) A612, and (c) A613. ....	37
Figure 4-5 Schematic showing DSC sample locations on the billet. ....	38
Figure 4-6 Schematic of the jaw set for high temperature compression test done using the Gleeble™ 3500 with dilatometer to measure the change in diameter for the sample. ....	40
Figure 4-7 Temperature history of the sample when tested on Gleeble™ 3500 and cam plastometer. .....	40
Figure 4-8 Schematic of the compression sample used for the cam plastometer. ....	42
Figure 4-9 A schematic view of the extrusion setup, water quenching tank, and the sample location. .....	43
Figure 4-10 A schematic view of the extrusion process with five parts including ram, die, billet, container, and feeder. ....	44
Figure 4-11 Schematic of the bar extrusion (left) and the model and mesh in DEFORM™ 2D (right). ....	49
Figure 4-12 Volumetric heat capacity of aluminum alloy and tooling material H-13 [94]. ....	53
Figure 4-13 Mesh windows at die corner. ....	56
Figure 4-14 Model-predicted temperature from the center to the surface of the bar at the die corner (left) and model-predicted breakthrough load (right) showing the influence of minimum element size. ....	56
Figure 4-15 Effect of minimum element sizes on the predicted effective strain rate (left) and effective strain (right). ....	57
Figure 4-16 Three types of die geometries and their contact condition with the billet: (a) choked die bearing, (b) flat die bearing, (c) relief bearing [96]. ....	58
Figure 4-17 Comparisons of the measured loads (a) and temperatures (b) to the measured load and temperature at an extrusion speed of 26 mm/s for the 25 mm flat die respectively (Extrusion ratio = 17:1 and A612 material). ....	59
Figure 4-18 Three friction conditions along the die bearing of the 35 mm choked die (Extrusion ratio = 17:1). ....	60

Figure 4-19 Comparison of the measured load history to the model predicted load history using different friction conditions at the extrusion speed of 26 mm/s for the 35 mm choked die. .... 61

Figure 4-20 Comparison of the measured temperature histories at the (a) TC1 and (b) TC2 to the model predicted temperature histories using different friction conditions at the extrusion speed of 26 mm/s for the 35 mm choked die with material A612 respectively. .... 61

Figure 4-21 Model verification for different die geometries at varying extrusion speeds by comparing the measured load and temperature to the predicted load: (a) and (b) show the comparisons of a typical predicted and measured temperature history and a typical predicted and measured load history, respectively, for the 25 mm flat die with an extrusion speed of 26 mm/s, and (c) presents the calculated error between the predicted temperatures and loads and the corresponding measured values for all dies at a stroke of 150 mm. The data incorporated 2-3 different extrusion speeds. .... 63

Figure 5-1 DSC traces of the as-cast A576 material and the homogenized A576 material. .... 65

Figure 5-2 DSC traces of the as-cast A611 material and the homogenized A611 material. .... 66

Figure 5-3 DSC traces of (a) as-cast A612 material and (b) the homogenized A612 material. ... 66

Figure 5-4 DSC traces of (a) as-cast A613 material and (b) the homogenized A613 material. ... 67

Figure 5-5 Measured DSC curve of homogenized A612 obtained from the C80 calorimeter. .... 67

Figure 5-6 DSC results and determination of the solidus temperature of the homogenized material: (a) shows the DSC traces of both samples from the edge and center of the billet going from room temperature to melting; (b-c) shows how the solidus temperature is determined for the material [99]. .... 69

Figure 5-7 Comparison of the estimated solidus temperature as a function of Cu content for as-cast and homogenized A576, A611, A612 and A613 from center of the billet and model-predictions using thermo-calc. .... 70

Figure 5-8 Measured flow stress at the deformation temperature of 450°C for three materials with varying Cu contents (solid line: A611, dash line: A612, dot line: A613) at different strain rates (0.1/s-black, 1/s-red, and 10/s-blue) on Gleeble™ 3500. .... 72

Figure 5-9 Measured flow stress at the deformation temperature of 500°C for three materials with varying Cu contents (solid line: A611, dash line: A612, dot line: A613) at different strain rates (0.1/s-black, 1/s-red, and 10/s-blue) on Gleeble™ 3500. .... 73

Figure 5-10 Measured flow stress at the deformation temperature of 550°C for three materials with varying Cu contents (solid line: A611, dash line: A612, dot line: A613) at different strain rates (0.1/s-black, 1/s-red, and 10/s-blue) on Gleeble™ 3500. .... 73

Figure 5-11 Measured flow stress at the deformation temperature of 550°C for three materials with varying Cu contents (solid line: A611, dash line: A612, dot line: A613) at different strain rates of 50/s (black) and 100/s (red,) on cam plastometer. .... 74

Figure 5-12 Relationship of (a)  $\ln\epsilon$  vs.  $\ln\sigma$ ; (b)  $\ln\epsilon$  vs.  $\sigma$ ;  $\ln\epsilon$  vs.  $\ln[\sinh(\alpha\sigma)]$ ; (d)  $\ln[\sinh(\alpha\sigma)]$  vs.  $1/T$ . .... 77

Figure 5-13 Comparison of model predicted flow stress and measured flow stress for A611, A612, and A613. The dotted lines represent +/- 10% of the measured data. .... 78

Figure 5-14 Typical measured temperature (a) and load (b) histories of the extrusion trials at different extrusion speeds for A612 material and with an extrusion ratio of 70:1 in extrusion trial #1..... 80

Figure 5-15 Schematic sample locations from the extrudate for analysis. .... 81

Figure 5-16 Visual observation of the extrudate surfaces extruded by the 12 mm flat die with an extrusion ratio of 70:1, the material is A612: (a) the as-extruded surface images of the extrudates from the back of the extrusion with the extrusion speed change from 4-10 mm/s; (b) and (c) show how the extrudate surface changes from the beginning to the end of the extrusion process at the extrusion speed of 9 mm/s and 10 mm/s respectively. .... 82

Figure 5-17 Surface morphology of the back of the extrudates produced by a 12 mm flat die with an extrusion ratio of 70:1 using A612 at varying extrusion speed: (a) 4 mm/s, (b) 6 mm/s, (c) 7 mm/s, (d) 8 mm/s, (e) 9 mm/s, and (f) 10 mm/s by SEM. (ED = Extrusion Direction). .... 83

Figure 5-18 PCG layer in the cross-section area along the extrusion direction of the extrudates produced by the 12 mm flat die with A612 at varying extrusion speed: (a) 4 mm/s, (b) 6 mm/s, (c) 8 mm/s, (d) 9 mm/s, (e) 10 mm/s by microscope with polarized light. .... 85

Figure 5-19 Correlation of the measured temperature in the die bearing when the stroke is 150 mm and the PCG layer thickness of the extrudates produced by the 12 mm flat die using A612 at various extrusion speeds using A612. .... 86

Figure 5-20 Surface cracks picked from the extrudates generated by the 25 mm flat die with the material of A612 and the extrusion speed ranging from 20 mm/s to 31 mm/s for measurement of the crack size..... 87

Figure 5-21 Surface maximum cracks change with extrusion speed in length (a) and width (b). 87

Figure 5-22 Relationship between the natural logarithm of (a) the maximum crack length width and the extrusion speeds, and (b) the maximum crack width and the extrusion speeds. .... 88

Figure 5-23 Electron backscatter diffraction (EBSD) inverse pole figure (IPF) map in RD-ND plane of the extrudates produced by a zero-bearing die at an extrusion speed of 28 mm/s using A612 material..... 89

Figure 5-24 Surface visual observations of the samples from the back of the extrudates produced with A612 at various extrusion speed by dies with different extrusion ratios: (a) extrudates produced by 12 mm flat die with extrusion ratio of 70:1, (b) extrudates produced by 25 mm flat die with extrusion ratio of 17:1..... 90

Figure 5-25 Surface visual observation of the samples from the back of the extrusion profiles extruded by four different die geometries at varying extrusion speed with the same extrusion ratio of 17:1 using A612: (a) 25 mm flat die, (b) 35 mm choked die, (c) zero-bearing die, and (d) 12 mm choked die..... 92

Figure 5-26 Surface visual observation of the samples from the back of the extrusion profiles extruded by 25 mm flat die using materials with different Cu contents: (a) A612 with extrusion speed varying from 20-31 mm/s, and (b) A613 with extrusion speed varying from 5-20 mm/s.. 94

Figure 5-27 Surface morphology of extrudates produced by a 25 mm flat die using A612 with an extrusion speed of (a) 20 mm/s, (b) 22 mm/s, (c) 24 mm/s, (d) 26 mm/s, (e) 28 mm/s, and (f) 31 mm/s. Figures (g-i) show the surface morphology of the extrudate from the front, middle, and back of the sample produced with an extrusion speed of 31 mm/s, respectively. Extrusion direction from bottom to top. .... 96

Figure 5-28 Surface crack locations of the extrudate produced by a 25 mm flat die using A612 at an extrusion speed of (a) 20 mm/s and (b) 26 mm/s, suggests that surface cracking occurs at exposed grain boundaries..... 97

Figure 5-29 Surface morphology of extrudates produced by a 35 mm choked die using A612 material with an extrusion speed of (a) 22 mm/s, (b) 26 mm/s, (c) 30 mm/s, (d) 34 mm/s, and (e) 40 mm/s..... 98

Figure 5-30 Surface morphology of extrudates produced by a 12 mm choked die using A612 with an extrusion speed of (a) 28 mm/s, (b) 32 mm/s, and (c) 34 mm/s. .... 99

Figure 5-31 Surface morphology of extrudates produced by a zero-bearing die using A612 with an extrusion speed of (a) 26 mm/s, (b) 28 mm/s, and (c) 29 mm/s. .... 99

Figure 5-32 Surface morphology comparison of extrusion profiles produced by four die geometries from the back of the extrudates and at a similar extrusion speed using A612 material: (a) 25 mm flat die at 26 mm/s; (b) 35 mm choked die at 26 mm/s; (c) zero-bearing die at 26 mm/s; and (d) 12 mm choked die at 28 mm/s. Extrusion direction from bottom to top. .... 101

Figure 5-33 Surface morphology of extrudates produced using materials with different Cu contents. (a) and (b) are surface morphology images of A612 and A613, respectively, extruded by a flat die at an extrusion speed of 20 mm/s, (a1) and (b1) are the high magnification images of (a) and (b) showing the crack location respectively; (c) and (d) are surface morphology images of A612 and A613 extruded by 35 mm choked die at an extrusion speed of 22 mm/s and 20 mm/s respectively. .... 103

Figure 5-34 Microstructure images of the cross section perpendicular to the extrusion direction of the back extrudates produced by: (a) 25 mm flat die (b) zero-bearing die, (c) 12 mm choked die, and (d) 35 mm choked die at an extrusion speed of 26 mm/s for all die except the zero-bearing die (28 mm/s) using A612. .... 105

Figure 5-35 Microstructure images of the cross section perpendicular to the extrusion direction using materials with different Cu contents: (a) and (b) are microstructure images of A612 and A613, respectively, extruded by a flat die at an extrusion speed of 20 mm/s; (c) and (d) are microstructure images of A612 and A613 extruded by choked die at an extrusion speed of 22 mm/s and 20 mm/s respectively..... 107

Figure 5-36 3D surface roughness and laser confocal micrography images showing the comparison of extrusion profiles produced by four die geometries using A612 at a similar extrusion speed: (a) 25 mm flat die at 26 mm/s; (a) 35 mm choked die at 26 mm/s; (a) zero-bearing die at 26 mm/s; and (a) 12 mm choked die at 28 mm/s. Extrusion direction is from the bottom to the top of the figure. .... 109

Figure 5-37 Surface roughness images of the samples taken from the back of the extrudates with different Cu contents: (a) and (b) are surface roughness of A612 and A613, respectively, extruded by a flat die at an extrusion speed of 20 mm/s; (c) and (d) are surface roughness of A612 and A613 extruded by choked die at an extrusion speed of 22 mm/s and 20 mm/s respectively. .... 110



Figure 5-38 Model-predicted stress components from the center to the surface at the die corner at an extrusion speed of 6 mm/s for dies with an extrusion ratio of: (a) 17:1, (b) 70:1 at a stroke of 150 mm using A612..... 112

Figure 5-39 Model-predicted temperature distribution from the center to the surface of the billet at die corner at an extrusion speed of 6 mm/s by dies with an extrusion ratio of 17:1 and 70:1 at a stroke of 150 mm. The starting billet temperature is 480°C and material is A612. .... 113

Figure 5-40 Model-predicted  $\sigma_z$  and temperature contour map at the die bearing region for die with extrusion ratio of 17:1 (a and a1) and 70:1 (b and b1) at the extrusion speed of 6 mm/s at a stroke of 150 mm with A612..... 115

Figure 5-41 Model-predicted (a)  $\sigma_z$  and (b) temperature distribution along the die bearing for dies with extrusion ratio of 17:1 and 70:1 at a stroke of 150 mm at the extrusion speed of 6 mm/s with material A612..... 116

Figure 5-42 Model-predicted stress components from the center to the surface at the die corner at an extrusion speed of 26 mm/s for: (a) 25 mm flat die, (b) 35 mm choked die, (c) zero-bearing die, and (d) 12 mm choked die using the material A612 and a starting billet temperature of 500°C. .... 118

Figure 5-43 Model-predicted temperature distribution from the center to the surface of the billet at die corner for all die geometries using A612 at an extrusion speed of 26 mm/s..... 119

Figure 5-44 Model-predicted  $\sigma_z$  and temperature contour map at the die bearing region for the different die types using A612: the 25 mm flat die (a, a1), the 35 mm choked die (b, b1), the zero-bearing die (c, c1), and the 12 mm choked die (d, d1) at a stroke of 150 mm. .... 121

Figure 5-45 Model-predicted (a)  $\sigma_z$  and (b) temperature distribution along the die bearing for all four dies using A612 at the stroke of 150 mm at an extrusion speed of 26 mm/s..... 122

Figure 5-46 Model predicted temperature and corresponding  $\sigma_z$  at the die corner at varying extrusion speeds for all die geometries for A612. For die with ER=17:1 the data at the front, middle and back of the extrusion is extracted. For die with ER=70:1 the data at the front, middle and back of the extrusion is extracted. Different colors refer to the corresponding surface morphology observed in the extrusion trial with **Green** indicating no surface cracks, **Orange** indicating micro cracks, and **Red** indicating visible surface cracks. For the 35 mm choked die, both the data at the die corner and middle of the die bearing is plotted..... 125

Figure 5-47 Model predicted  $\sigma_z$  at the die corner and temperature (corresponding homologous temperature) at the die corner at varying extrusion speeds for materials A612 and A613 using the 25 mm flat die. .... 126

Figure 5-48 Model predicted relationship between the predicted maximum temperature and the extrusion speed at the stroke of 150 mm for different starting billet temperature by 25mm flat die using A612. The symbols represent the model predicted. .... 128

Figure 5-49 Model predicted linear relationship between the breakthrough load and the corresponding mean flow stress at the same starting billet temperatures and extrusion speeds by 25mm flat die using A612 material. .... 130

Figure 5-50 Model predicted ELD for an A612 alloy using the 25 mm flat die with the temperature limits: 590°C (Red line), 580°C (Orange line), and 570°C (Green line) and the extrusion press limits: 700MPa (Black solid curve) and 600MPa (Black dash curve)..... 131

Figure 5-51 Model predicted ELDs (lines and curves) and experimental observations of surface morphology conditions (“x”) for A612 at the back of the extrudate with the same extrusion ratio of 17:1 for different die geometries: (a) 25m flat die, (b) zero-bearing die, (c) 12 mm choked die, and (d) 35 mm choked die. .... 134

Figure 5-52 The effect of die geometries on the extrudability of A612 with black represents 25 mm flat die, red represents zero-bearing die, blue represents 12 mm choked die, and white represents the 35 mm choked die..... 136

Figure 5-53 Model predicted ELDs (lines) and experimental observations of surface morphology conditions (“x”) extruded by flat dies using A612 with extrusion ratio of (a)17:1 and (b)70:1. 138

Figure 5-54 Model-predicted ELD for A612 extruded using the flat die showing the effect of extrusion ratio with the black-shaded area representing the workable area of the die with an extrusion ratio of 17:1 and the red-shaded area representing the workable area of the die with an extrusion ration of 70:1..... 139

Figure 5-55 Model predicted ELDs (lines and curves) and experimental observations of surface morphology conditions (“x”) at the back of the extrudates extruded using the 25 mm flat die with: (a) material A612 and (b) material A613..... 141

Figure 5-56 Comparison of the model predicted ELD for three materials with different Cu additions extruded using the 25 mm flat die. .... 142

## List of Tables

Table 1-1 Mechanical properties of some common AA6xxx alloys (T6) [10].....	3
Table 1-2 Chemical composition of AA6056, AA6066 and AA6082 (%) [10–12].....	4
Table 4-1 Chemical compositions of different Al-Mg-Si-Cu alloys (wt.%) used in this research. .....	34
Table 4-2 Calculated Mg <sub>2</sub> Si solvus temperature and melting temperatures of different alloys via Thermo-Calc using the TTAL6 database.....	36
Table 4-3 Summary of the compression tests on Gleeble <sup>TM</sup> 3500 and cam plastometer. ....	42
Table 4-4 Die bearing geometries (blue lines) used for different extrusion trials and illustrations showing the locations of the thermocouples (green dots) for the different die geometries (TC = thermocouple). Extrusion direction is from top to bottom, and red line is the die bearing. ....	45
Table 4-5 Extrusion parameters for extrusion trial #1 (Extrusion ratio = 70:1).....	46
Table 4-6 Extrusion parameters for extrusion trial #2 (Extrusion ratio = 17:1).....	47
Table 4-7 Extrusion parameters for extrusion trial #2 (Extrusion ratio = 17:1).....	48
Table 4-8 Material data requirements for extrusion process simulation [94].....	51
Table 4-9 Material thermal physical properties used in the model [94].....	52
Table 5-1 Estimated solidus temperature of each material based on DSC tests (°C).....	70
Table 5-2 Average flow stress data calculated between the true strain of 0.1 to 0.4 for A611, A612, and A613 at different deformation temperatures and different strain rates (MPa).....	74
Table 5-3 Constitutive model parameters of A612.....	78
Table 5-4 Extrusion simulations run for 25 mm flat die (A612) to construct ELD.....	127
Table 5-5 Model predicted maximum extrusion speed (to reach the temperature limit) for different starting billet temperature by 25mm flat die using A612 material. ....	129
Table 5-6 Summary of the extrusion profile surface quality at different extrusion speeds for different die geometries with the same extrusion ratio 17:1 and the same material A612, <b>Green</b> means good surface, <b>Orange</b> means micro crack, <b>Red</b> means visible cracks.....	132
Table 5-7 Summary of the extrusion profile surface quality at different extrusion speeds for the two flat dies with different extrusion ratio and the same material A612, “Green” means good surface, “Orange” means micro crack, “Red” means visible cracks. ....	138

Table 5-8 Summary of the extrusion profile surface quality of A612 and A613 at different extrusion speeds extruded by 25 mm flat die, **green** means good surface, **orange** means micro crack, **red** means visible cracks. .... 141

## Chapter 1 Introduction

The focus on low carbon emissions in recent years is driving customers to move away from high fuel consumption and heavy vehicles. Energy-saving and lightweight automobiles are becoming more and more popular. The government-mandated Corporate Average Fuel Economy (CAFE) also set the new standard of reaching the average fuel economy of 54.5 mpg (23.2 km/liter) by 2025 compared to 36.7 mpg (15.6 km/liter) in 2017 [1]. Both factors have driven automotive manufacturers to seek ways to improve the fuel economy of vehicles. From the perspective of material manufacturers, one of the easiest ways to reach these targets and improve fuel efficiency is to develop lighter weight materials with high strength and acceptable ductility.

Aluminum alloys have been widely used in many car parts, such as wheels, bumpers, suspension parts and the body parts [2] in recent years and the percentage of aluminum usage in vehicles continues to increase. Figure 1- shows the anticipated future amount of aluminum used in vehicles in North America [3]. It has been reported that every 10% reduction of vehicle weight can improve the fuel economy by 7%, which will also reduce the greenhouse gas emissions [4]. The 2015 Ford-150 pickup truck is an example of using AA6xxx aluminum alloys in its body to reduce the weight of the truck by about 300kg [5].

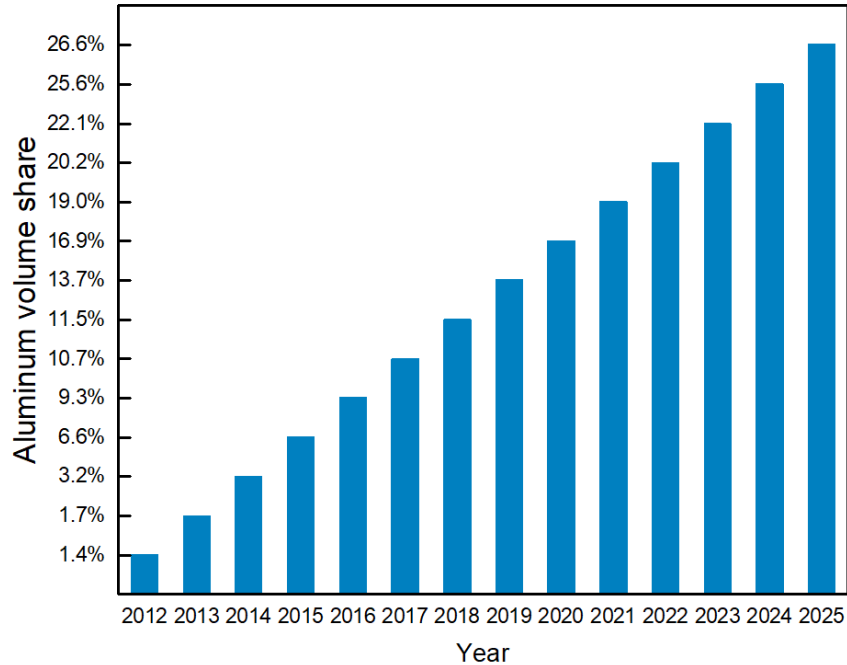


Figure 1-Usage of aluminum’s volume share in body and closure components of vehicles in North America in recent years and the anticipated usage in the future [6].

Extrusion is a process of producing products with a constant cross-sectional profile. This method has been extensively used in the production of aluminum car parts, such as extruded tubes and multi-hole profiles for engine, extruded hollow profiles for structural components[7].

With the aim of further reducing the weight of vehicles, it is anticipated that the amount of aluminum used in cars will increase in the future. To support this growth, the development and use of a comprehensive process model which links the microstructure and the mechanical properties to the extrusion process can help further alloy development and understand their manufacturability.

Currently, the most widely used aluminum alloys in car manufacturing are the AA6xxx alloys due to their low density, good formability, high corrosion resistance, and high strength/weight ratio [8]. These alloys are age hardening aluminum alloys that obtain their high strength by artificial aging and their main alloy elements are Mg and Si. Their mechanical

properties depend on the detailed chemical composition, microstructure, manufacturing methods and heat treatment [9]. Table 1-1 shows the mechanical properties of some common AA6xxx alloys in the T6 condition. AA6082 has a relatively high yield strength and ultimate tensile strength compared with other AlMgSi alloys, such as AA6063 and AA6016 that have trace Cu or no Cu in their chemical composition, while AA6066 with Cu (1%) addition has much higher yield strength and ultimate tensile strength.

Table 1-1 Mechanical properties of some common AA6xxx alloys (T6) [10].

Material	Y.S.(MPa)	U.T.S.(MPa)	EL. (%)
AA6063	214	235	11
AA6016	210	280	11
AA6053	220	255	13
AA6082 (no Cu)	260	310	10
AA6066 (0.7-1.2% Cu)	360	388	12

Rio Tinto also has done some development work by examining a series of water quenched AA6xxx and AA7xxx alloys for both yield strength and the true strain to fracture, which is shown in Figure 1-1. Both series of alloys can obtain yield strength above 350 MPa and fracture strain greater than 0.2 indicated by a blue box in the figure.

This research will focus on the AA6xxx alloys with Cu additions as they are easy to cast and extrude, are corrosion resistant and the addition of Cu means they can attain higher strength. Specifically, AA6066 and AA6056 both with a Cu addition are high-strength AA6xxx alloys of interest. Referring to Table 1-2, the chemical compositions of AA6066, AA6056 and AA6082 are

given and as can be seen the chemical compositions of the three alloys are similar except for the addition of Cu in AA6056 and AA6066, which is in the range of 0.5-1.2%.

Based on the work done in Rio Tinto and the aim to improve the strength of the next-generation aluminum alloys, four different materials with different Cu additions were developed by Rio Tinto. Study was done on these materials to show the effect of Cu at each step of the manufacturing process to produce an extruded product.

Table 1-2 Chemical composition of AA6056, AA6066 and AA6082 (%) [10–12].

Alloys	Si	Mg	Cu	Mn	Cr	Fe	Other
AA6056	0.7-1.3	0.6-1.2	0.5-1.1	0.4-1	≤0.25	≤0.5	Bal.
AA6066	0.9-1.8	0.8-1.4	0.7-1.2	0.6-1.1	≤0.4	≤0.5	Bal.
AA6082	0.7-1.3	0.6-1.2	≤0.1	0.4-1.0	≤0.25	≤0.5	Bal.



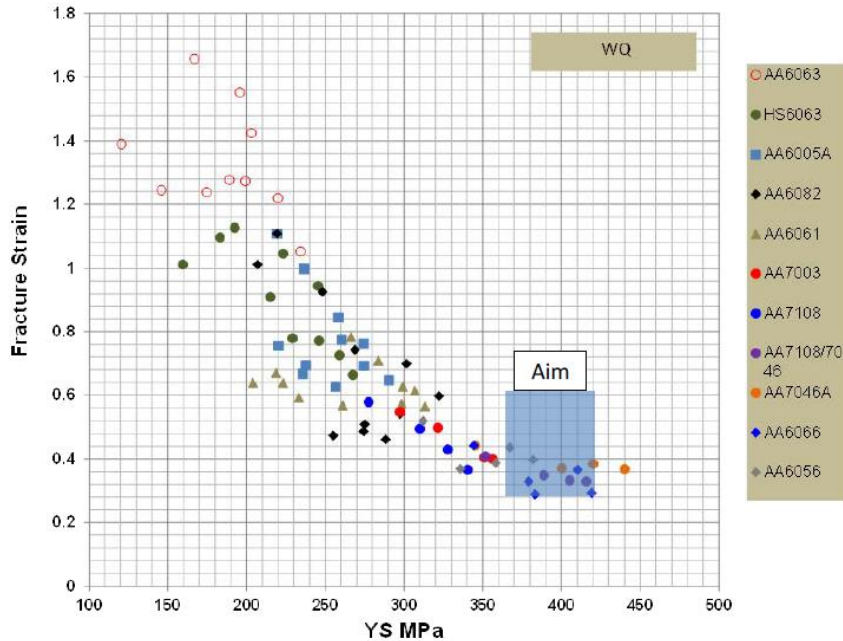


Figure 1-1 Experimental data from Rio Tinto on the fracture strain vs. yield strength (YS) for a wide range of aluminum alloys, including AA6xxx and AA7xxx (WQ = water quench) [13].

This research is a collaborative research and development project involving the University of Waterloo (UWaterloo) in Waterloo, ON, the University of British Columbia (UBC) in Vancouver, BC and Rio Tinto in Jonquiere, Quebec with the goal to develop a thorough process model of the homogenization, extrusion, quenching and artificial aging for AA6xxx alloys containing different Cu additions.

Extrusion is a complicated material process in which the material undergoes a large amount of plastic deformation. There are many parameters that can influence the extrusion process and the final extruded material properties including: die geometry, ram speed, extrusion ratio, extrusion temperature and the material being extruded. This research will focus on understanding the effect of Cu additions to the AA6xxx aluminum alloys and die geometry on the extrusion process and microstructure in the final extrudate produced and the material extrudability.

## **Chapter 2 Literature Review**

This chapter includes the current state of knowledge regarding extrusion of AA6xxx aluminum alloys, hot deformation behavior and constitutive models of these alloys, finite element analysis of extrusion process and construction of the extrusion limit diagram (ELD). Based on the literature, research knowledge gaps in these areas are indicated.

### **2.1 Extrusion process of AA6xxx aluminum alloys**

AA6xxx alloys are typical heat treatable alloys with medium strength and are widely used for production of extrusion products due to their good formability and machinability. About 80% of the extruded aluminum parts are made of 6xxx series aluminum alloy [14]. The detailed chemical composition, second phases and heat treatment methods have a close relationship with the extrusion process parameters, the extrusion mechanical properties, and extrusion defects.

#### **2.1.1 Extrusion process**

Manufacturing associated with the extrusion process of aluminum alloy involves several steps, which are shown in Figure 2-1 [15]. The temperature history that the material experiences in different process steps is shown in Figure 2-2. The extrusion process starts with melting, in which all the chemical substances and grain refiners are added into the melting mold. The chemical composition of the material is established in this step. The following steps are the Direct Chill (DC) casting and homogenization.

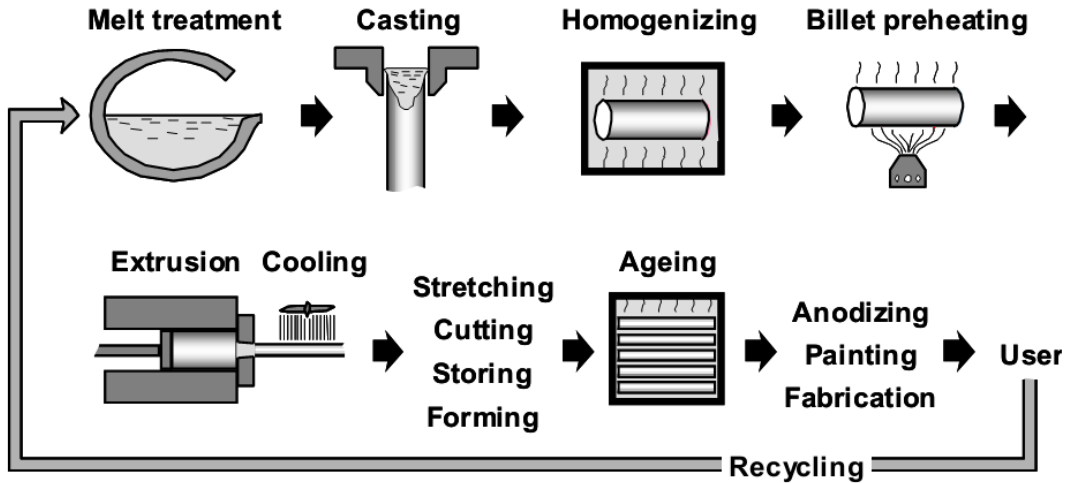


Figure 2-1 Process steps related to manufacturing an extrusion part from aluminum [15].

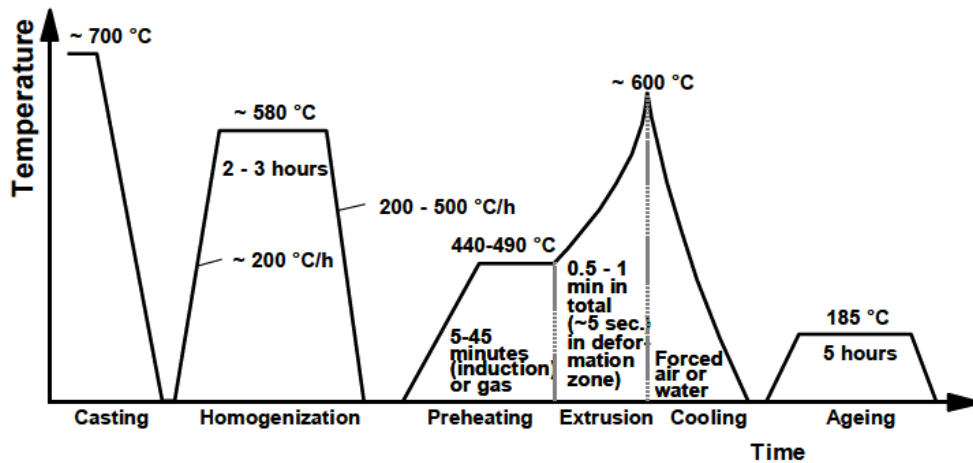


Figure 2-2 Sketch of temperature history in each step of the extrusion process [15].

In the DC casting step, the molten metal mixture is poured into a DC casting mold cooled by water and solid ingots, either billets or rectangular ingots, are formed. Billets are commonly used during extrusion and come in a variety of sizes with diameters in the range of 2-20 inches (50-500 mm) and lengths of 160-320 inches (4-8 m) [16]. The DC casting process typically produces equiaxed grains that has a size of  $\sim 100\text{ }\mu\text{m}$  with a dendritic structure that has a secondary

dendrite arm spacing (SDAS) of about 20  $\mu\text{m}$ [17], as shown in Figure 2-3, which is a typical equiaxed grain microstructure with dendrite structure of as-cast AA6082.

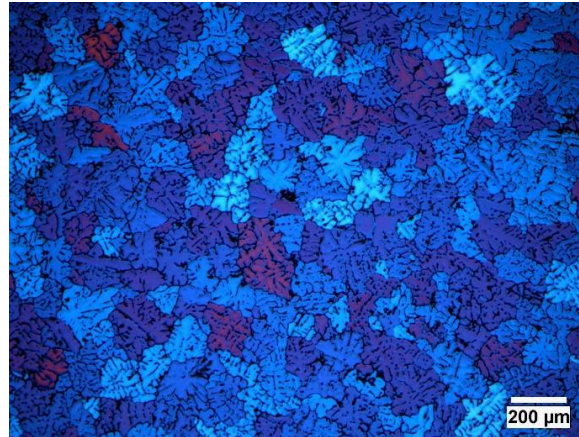


Figure 2-3 Typical grain structure of as-cast Al-Mg-Si alloy [17].

The as-cast material from DC casting process shows microstructural inhomogeneities, including alloying elements segregation into the inter-dendritic region and the grain boundaries, and the formation of the low-melting eutectics and intermetallic compounds due to the non-equilibrium characteristic of DC casting [18], all of which harm the extrudability of the as-cast billet. Figure 2-4 (a) shows a typical as-cast optical microstructures of Al-Mg-Si alloys, where the primary matrix of  $\alpha$ -Al, eutectic Si phase and  $\text{Mg}_2\text{Si}$  intermetallic phase could be observed [19]. With Cu added as shown in Figure 2-4 (b), Cu containing Q intermetallic phase and  $\theta$  intermetallic phase can also be observed. It is also observed that with the further increasing of Cu addition, the volume of  $\text{Mg}_2\text{Si}$  intermetallic phase decreases, while the fraction of Q and  $\theta$  phases increase. When the Cu in  $\text{Al}_9\text{Si}_0.5\text{Mg}$  reaches 0.85%, there is hardly  $\text{Mg}_2\text{Si}$  observed, which is due to the consumption of Mg and Si when Q phase is formed.

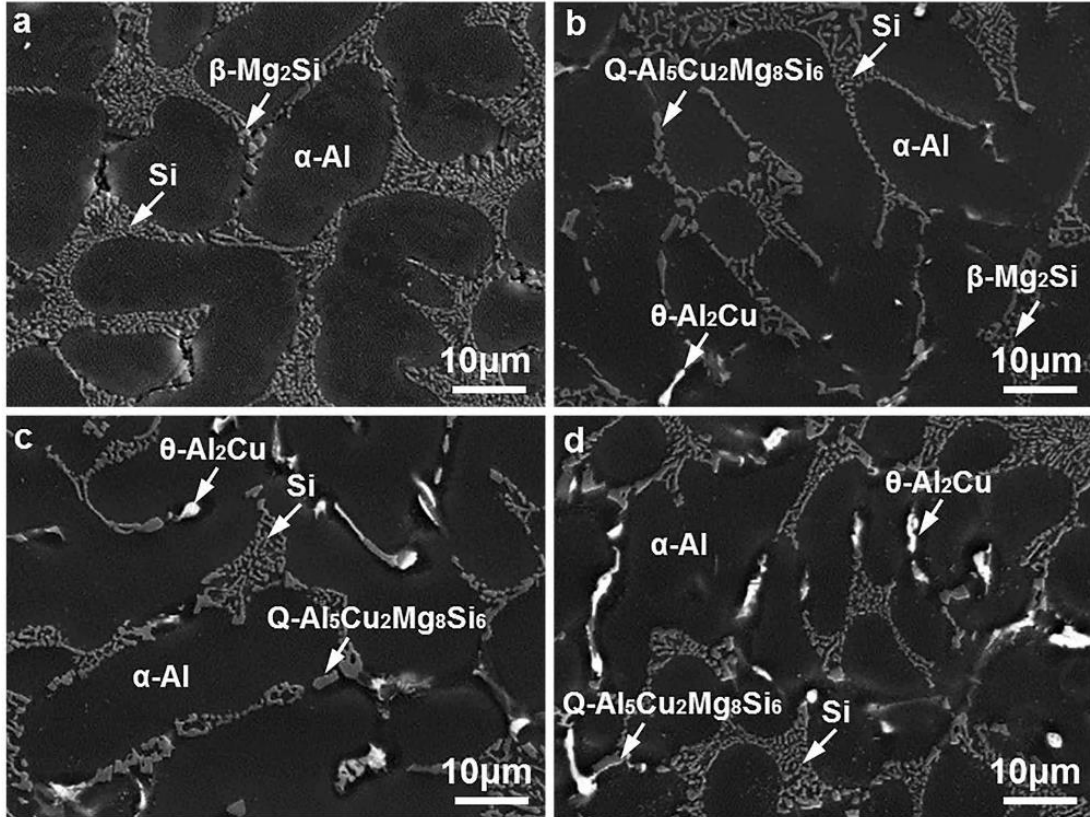


Figure 2-4 Microstructures of as-cast Al9Si0.5Mg alloys by SEM with (a) 0% Cu, (b) 0.4% Cu, (c) 0.85% Cu, and (d) 1.25% Cu. [19].

### 2.1.2 Intermetallic phases formation in DC casting

Solidification of AA6xxx alloys takes place dendritically with Mg<sub>2</sub>Si, AlFeSi phase and some eutectic phases, such as Al-Mg<sub>2</sub>Si and Al-Si depending on the alloy chemical composition [20]. The Mg<sub>2</sub>Si phase usually forms during the solidification. Its amount and morphology depend on the specific chemical composition and the cooling rate during the solidification [21,22]. The nonequilibrium solidification rates during casting can result in the formation of coarse eutectic Mg<sub>2</sub>Si particles [23].

Another common element in Al-Mg-Si alloys is Fe that is present at a trace level as an impurity. Fe has a low solubility in aluminum. It can combine with Al and Si to form brittle and hard Fe containing intermetallics, which exist mostly within the inter-dendritic region. The Fe bearing phase can exist commonly in two forms:  $\alpha$ -AlFeSi and  $\beta$ -AlFeSi [24]. As shown in Figure 2-5,  $\alpha$ -AlFeSi is commonly observed to have a cubic structure and Chinese-script morphology, while  $\beta$ -AlFeSi usually has a monoclinic structure and platelet-like morphology, which is more detrimental to the extrudability by inducing cracks and surface defects and lowering the mechanical properties such as ductility and strength [18,25,26].

Some AA6xxx aluminum alloys also contain Mn and Cr. Both of them have a relatively low diffusion rate and are prone to segregate into the inter-dendritic region and grain boundaries in the solidification process [27].

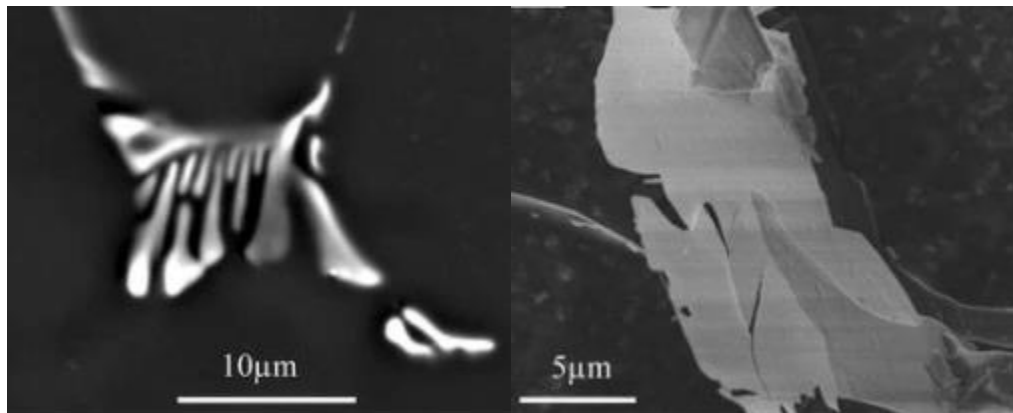


Figure 2-5 Chinese-script  $\alpha$ -AlFeSi (left) and plate-like  $\beta$ -AlFeSi (right) [25].

When Cu is added in the Al-Mg-Si alloys, the solidification process can be affected in two ways primarily. Addition of Cu decreases the solidus temperature and the eutectic point of the alloy [28]. Cu also promotes the formation of new phases such as  $\theta$  ( $\text{Al}_2\text{Cu}$ ) and/or Q phase or the

metastable Q' phase (Al-Cu-Mg-Si). The exact stoichiometry of the Q/Q' phase is still debatable and may have the following possible forms:  $\text{Al}_5\text{Cu}_2\text{Mg}_8\text{Si}_6$ ,  $\text{Al}_4\text{CuMg}_5\text{Si}_4$ ,  $\text{Al}_4\text{Cu}_2\text{Mg}_8\text{Si}_7$  and  $\text{Al}_3\text{Cu}_2\text{Mg}_9\text{Si}_7$  [29]. Dong et al. [19] studied the effect of different Cu content on the as-cast microstructure of the AA6xxx alloys, as shown in Figure 2-4. As the Cu content increases from 0-1.25%, the volume fractions of Q and  $\theta$  increase. The formation of Q phase consumes Mg which makes the volume fraction of  $\text{Mg}_2\text{Si}$  phase decrease.

### **2.1.3 Homogenization**

The manufacturing step following DC casting is homogenization. This homogenization process involves heating the ingot to a predetermined temperature, usually 20-50°C below the solidus temperature [30], holding at this temperature for a certain period of time (usually 2-4 hours), and then cooling at a controlled rate [31].

The metallurgical changes that occur during homogenization include decreasing the element micro-segregation, dissolution of low-melting eutectics, transformation of Fe-containing intermetallic phase to rounder phase, dissolution of  $\text{Mg}_2\text{Si}$  phase, and precipitation of Mn/Cr containing dispersoids. Industrial extrusion trials have shown that the homogenized billet can be extruded more easily compared to simply extruding the preheated as-cast billet. The extruded surface condition is also improved with less pick-up defects after homogenization [32]. After homogenization, a more uniform microstructure is obtained, by which the good extrusion surface finish and mechanical properties can be achieved.

#### ***Dissolution of $\text{Mg}_2\text{Si}$ phase***

One of the main roles of the homogenization process is to dissolve the  $\text{Mg}_2\text{Si}$  particles into the solid solution. The undissolved  $\text{Mg}_2\text{Si}$  precipitates can cause eutectic melting of Al and  $\text{Mg}_2\text{Si}$  during extrusion, which can result in surface defects and limit the extrudability. On the other hand,

a microstructure with Mg and Si fully dissolved into the Al matrix is also not desired because the extrusion pressure can increase significantly due to solid solution strengthening [33]. The size and number of  $Mg_2Si$  precipitates can be controlled via the cooling rate after homogenization. The most desirable structure after homogenization is one in which there are as many  $Mg_2Si$  precipitates that have formed as possible but they can also be easily redissolved during extrusion to achieve good surface quality and high extrudability [31].

The number and size of the  $Mg_2Si$  precipitates are sensitive to the cooling rate during homogenization. A slow cooling rate is likely to form coarse  $Mg_2Si$  particles. Coarse  $Mg_2Si$  particles are hard to solutionize during preheating before extrusion and can lead to incipient melting and surface tearing defects during extrusion. This gives the extrusion a poor surface finish and tensile properties. A fast-cooling rate after homogenization tends to trap the Mg and Si with little  $Mg_2Si$  precipitates. The solid solution strengthening effect increases the material flow stress and thus the pressure during extrusion [31]. Sun et al. [33] revealed that the  $Mg_2Si$  increases both in size and number as the cooling rate decreases as shown in Figure 2-6. The  $Mg_2Si$  precipitate number and size are relatively small in the water quenched sample because most of the  $Mg_2Si$  is retained in the Al matrix with a fast-cooling rate. In contrast, the furnace cooled sample shows a relatively high density of  $Mg_2Si$  particles and the  $Mg_2Si$  particles have relatively larger size due to the long cooling time. The larger  $Mg_2Si$  precipitates formed at a slow cooling rate in the sample may still exist after extrusion and decrease the strengthening extent of the  $Mg_2Si$  compared to that cooled by water quenching and air cooling.



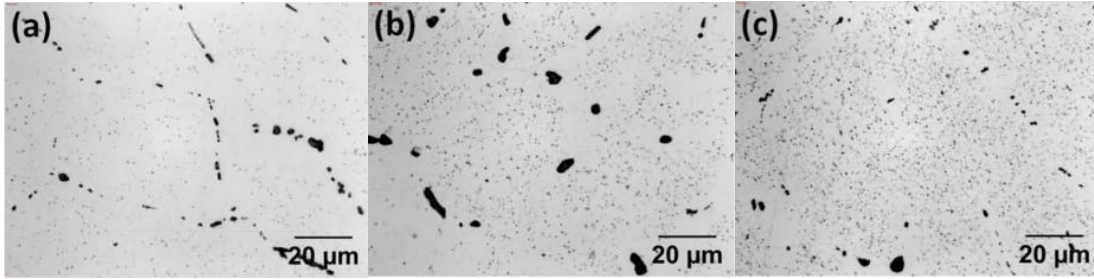


Figure 2-6 Microstructure of homogenized AA6005 at different cooling rate: (a) water quenching ( $\sim 500000$  °C/h); (b) air cooling (3000 °C/h); (c) furnace cooling (130 °C/h) [33].

### *Transformation of Fe-containing intermetallic phase*

Another aim of the homogenization is to modify the phase type and morphology of the Fe bearing intermetallics to improve the extrudability. In the Al-Mg-Si alloys, two dominant Fe bearing intermetallics are  $\alpha$ -AlFeSi and  $\beta$ -AlFeSi formed during DC casting. The  $\alpha$ -AlFeSi is more compact and spherical and is less harmful to the extrusion process and the mechanical properties of the products, while  $\beta$ -AlFeSi shows a platelet-like morphology with sharp edge that is especially detrimental and can cause surface tears during extrusion and affect the mechanical properties of extrusion products [25]. The homogenization treatment can transform the  $\beta$ -AlFeSi phase into  $\alpha$ -AlFeSi [30]. The alloying element Mn/Cr can also accelerate this transformation [34].

The soaking temperature and cooling rate during homogenization affect the transformation of  $\beta$ -AlFeSi to  $\alpha$ -AlFeSi. Birol [31] studied the soaking temperature and time on the transformation of Fe bearing phases. As shown in Figure 2-7, at soaking temperature of 540°C, the dominant Fe bearing phase is still  $\beta$ -AlFeSi after 6 hours. While when the soaking temperature is 580°C, the platelet like  $\beta$ -AlFeSi phase becomes the minor phase and shows a “necklace” configuration in the grain boundary after 2 hours. This means that soaking temperature and time affect the transformation of  $\beta$ -AlFeSi to  $\alpha$ -AlFeSi.

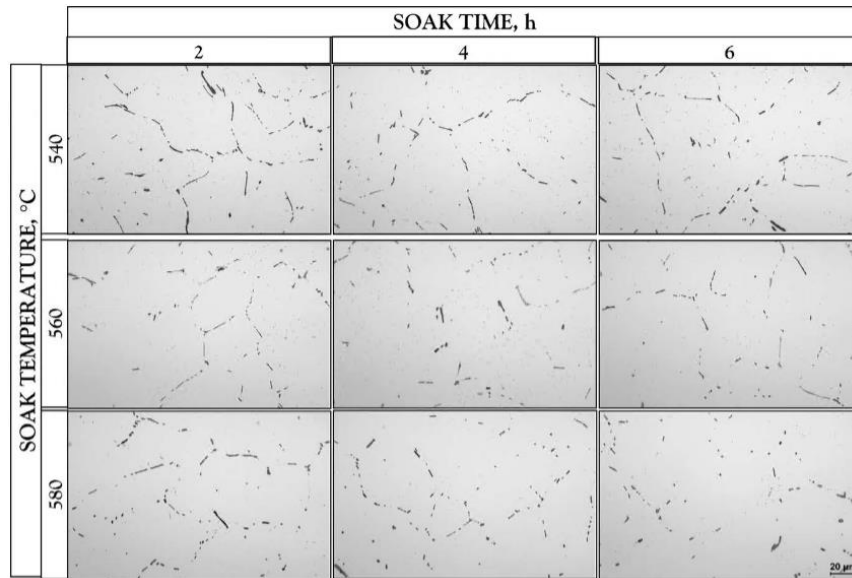


Figure 2-7 The microstructure of AA6063 samples soaked at 540-560°C for different times: 2 hours, 4 hours and 6 hours [31].

### *Mn/Cr dispersoids*

Another transformation during homogenization is the formation of Mn/Cr containing dispersoids. The dispersoids can inhibit the recovery, recrystallization, and grain growth during extrusion thus improve the properties of the alloys [35,36].

### *Cu containing Q/Q' and Al<sub>2</sub>Cu phases*

When Cu is added, the Q/Q' phase and the Al<sub>2</sub>Cu phase formed during solidification dissolve or partially dissolves into the Al matrix during homogenization depending on the homogenization temperature and time [37–39]. There is little information available on the effect of Cu on other phases during the homogenization process.

## 2.2 Material flow and microstructure during extrusion

Extrusion is a manufacturing process which involves a ram pushing a billet through a die with a smaller opening and a certain cross-sectional profile. Figure 2-8 shows a diagram of the simple bar extrusion. The billet undergoes severe plastic deformation due to the interaction between the material and the tooling. This technology has been used for more than 100 years and still attracts the interest of the manufacturing industry due to its advantages like the ability to produce complex cross-section parts, low cost, and continuous production. The parameters that can affect the extrusion process including the material chemical composition and starting microstructure, extrusion type, length of billet, the extrusion temperature, extrusion ratio (ER), extrusion speed and the die geometry [40], where the combination of material type, extrusion ratio, and die geometry has not been comprehensively explored.

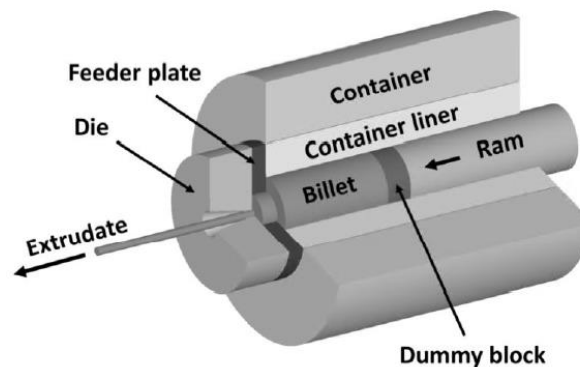


Figure 2-8 Schematic diagram of a simple bar direct extrusion [41].

Extrusion is a thermal mechanical process in which the material being extruded undergoes severe plastic deformation at elevated temperature due to the force exerted on the billet by the

tooling. Figure 2-9 shows how the material flows into the die in the flat die extrusion process. The material in different areas has different flow velocities and a dead metal zone (DMZ) is formed between the die face and the container wall. The material between the DMZ and the flowing part of the billet undergoes severe shear deformation due to the different flow velocities.

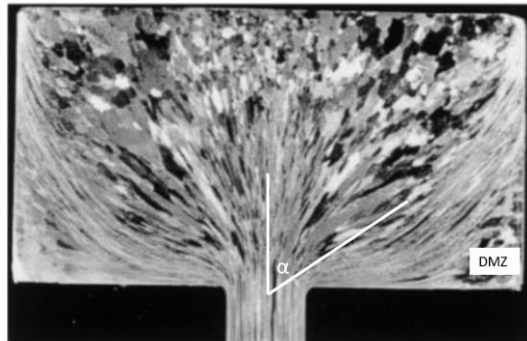


Figure 2-9 Material flow pattern of AA6061 during extrusion (DMZ indicates the dead metal zone) [42].

Schikorra et al. [43] classified the material near the die into four different zones, as shown in Figure 2-10. Zone I is the dead metal zone and the material in that zone experiences no deformation, but it still endures high hydrostatic pressure and high temperature. Materials in Zone II undergo the most severe shear deformation and the grains here are rotated and elongated with the material flowing into the die orifice, so the strain and strain rate is also high in this area. The material in zone III almost flows directly into the die and as the material gets closer to the die, the strain and strain rate increases rapidly. Zone VI is the area inside the die. Because material from the other three zones meet here, the microstructure can be dramatically different in different regions of zone VI. The temperature close to the die bearing in this area is high and recrystallization can also occur.

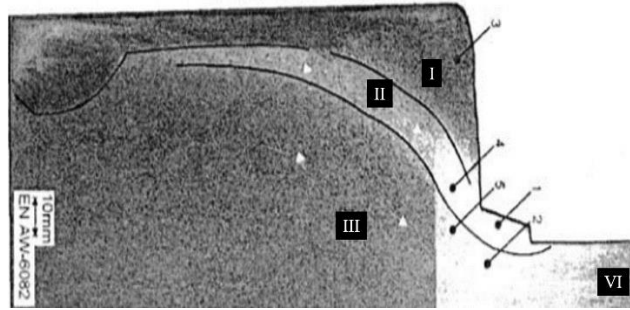


Figure 2-10 Four different zones formed during the extrusion of AA6082 [43].

## 2.3 Extrusion defects

There are numerous defects occurring during the extrusion of aluminum alloys due to a variety of reasons. The defects that are most relevant to this research are surface cracks. Some research has been done on the extrudate surface cracks and they primarily focused on the AA7xxx alloys. A few pieces of literature are on the surface cracking of AA2014 and AA5456. There is little information in the literature about the surface cracking of AA6xxx alloys.

Ngernbamrung et al. [44] studied the surface cracking in the extrusion of AA7075. In this research they indicate that the surface cracking is caused by melting at high temperature coupled with surface tension stress and zinc-segregated concentration at the grain boundary, which increases the sensitivity of surface tearing. Funazuka et al. [45] also reported that surface cracking of AA7075 is prone to happen at high temperature and high extrusion speed and caused by localization of zinc similarly.

Peng and Sheppard [46] applied quite a few crack criteria by finite element method to explain the surface cracking that occurred in AA2014 alloy, among which only the temperature

criteria and the empirical criteria could predict the surface cracking well. The same empirical criteria is also applied to predict the surface cracking behavior of AA5456 [47]. This empirical criterion is a function of extrusion speed and extrusion temperature.

Arif et al. [48] reported that surface cracking arises from localized tensile failure occurring in regions where melting happened. The initiation of the tearing usually occurs at the die edge and then propagates into the surface. Sheppard and Terry [30] also mentioned that surface cracking is closely related to the extrudate surface temperature rise when extruded at high speed. Surface cracking is caused by the tensile stress present at the edge of the die bearing, where local melting occurs.

From the above literature, it can be concluded that the extrusion speed, temperature, and the stress can all affect the occurring of the surface cracking during extrusion for the aluminum alloy studied. The high temperature caused mainly by high extrusion speed leads to the local melting of the material, and the local melting often happens at the grain boundary of the material. This melting plus the tensile stress at the edge of the die causes the initiation of the surface cracking. Subsequently the cracks propagate into the extrusion profile. However, little study was done on the surface cracking of AA6xxx alloys.

Different crack criteria have been developed to predict the occurrence of surface cracks. Pend and Sheppard [46] used different crack criteria to predict the surface cracks of AA2014. Those criteria include Oyane criterion, Cockcroft and Latham criterion, Normalized Cockcroft criterion and Latham criterion, Ayada criterion, Freudenthal criterion, temperature criterion, and the empirical criterion, among which only the temperature criterion and the empirical criterion can successfully predict all the four phenomena in the extrusion. The four phenomena are: 1) the cracks only appear on the profile surface; 2) high temperature can result in more severe cracks; 3) the

crack is getting more serious as the extrusion keeps going; 4) the cracks in indirect extrusion are less serious. The criteria used in the literature are usually one of the criteria mentioned above or one that incorporated some variables in it. Wang et al. [49] thought that when the extrusion profile surface temperature of AA2195 Al-Li alloy is high, and the accumulated plastic work reached a critical value the surface cracks will occur. Subsequently they change the Freundenthal criterion to incorporate the temperature and strain rate into it to predict the surface cracking. Kim et al. used the Cockcroft and Latham criterion to predict the fracture initiation in the extrusion of AA7075 alloy. Duan et al. [50] used the normalized Cockcroft and Latham criterion to predict the surface cracking sensitivity of AA2014 with different die geometry. They found that the choked die shows the least possibility of surface cracking.

The literature mentioned above is mainly about AA7xxx AA2xxx alloys, and a few AA5xxx alloys. Little research was done on the surface cracking criteria of AA6xxx alloys.

## **2.4 Extrusion limit diagram (ELD)**

In the extrusion process, it is important to use the proper process variables to ensure a high-quality product that satisfies the strict geometric, cosmetic and property requirements. The process variables that can be controlled in the extrusion process include the extrusion ratio, extrusion speed, and the initial billet temperature. The adjustment of those process variables is limited by two factors: the extrusion press capacity and the maximum temperature that can be tolerated by the material. The load needed to push the material cannot exceed the upper limit of the extrusion press capacity. The highest temperature during extrusion must be lower than the incipient melting temperature of the billet material, otherwise the surface quality and the mechanical properties of the extrusion will be affected [30].

The ELD that presents the two limits on one diagram was first proposed by Hirst and Ursell [51] and is schematically shown in Figure 2-11, where the pressure line is the limit of the press capacity and the surface locus represents the limit where surface defects occur.  $\ln R$  in the diagram can be the extrusion ratio or the extrusion speed.

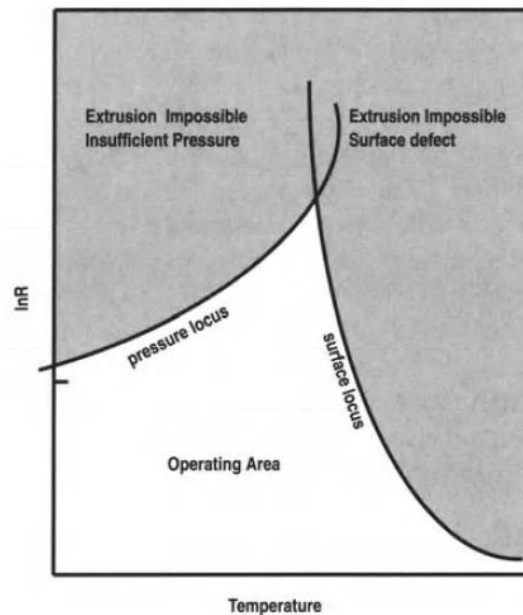


Figure 2-11 Schematic Extrusion Limit Diagram (ELD) proposed by Hirst and Ursell [51].

Based on the limit diagram proposed by Hirst and Ursell, the ELDs of different materials were developed. Figure 2-12 shows the ELD of AA6063, AA5456, and AA2014 at a ram speed of 14 mm/s in direct extrusion [52]. The line on the left represents the limit of the pressure and the line on the right is the boundary showing where surface tearing occurs. Notably, AA6063 has a large process window for extrusion relative to the other alloys, which makes it a highly extrudable material. This is because AA5456 and AA2014 are heavily alloyed alloy and lots of low melting phases present. In addition, AA6063 is easier to recover than the other two alloys.



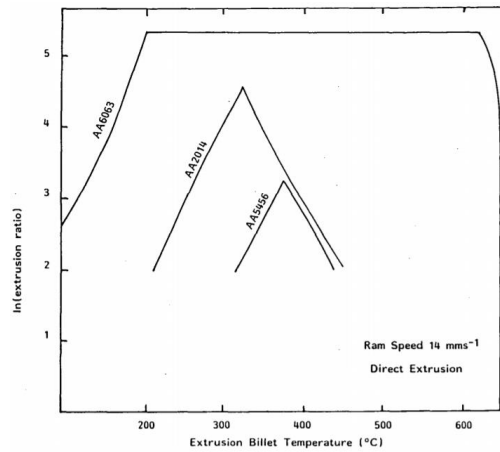


Figure 2-12 Extrusion limit diagram of AA6063, AA5456, and AA2014 [52].

Kim et al. [53] investigated the effect of scandium (Sc) additions on the hot extrudability of AA7075 alloys by experiment and numerical modelling. The ELDs is presented in Figure 2-13. The symbols '×' and '○' indicate the occurrence of surface cracking and a good extrusion condition, respectively. The black dash line between symbols '×' and '○' is the extrusion limit line obtained from simulation and the vertical dash line is the incipient melting temperature. The result shows that the surface crack occurred more easily to the material with a higher Sc content.

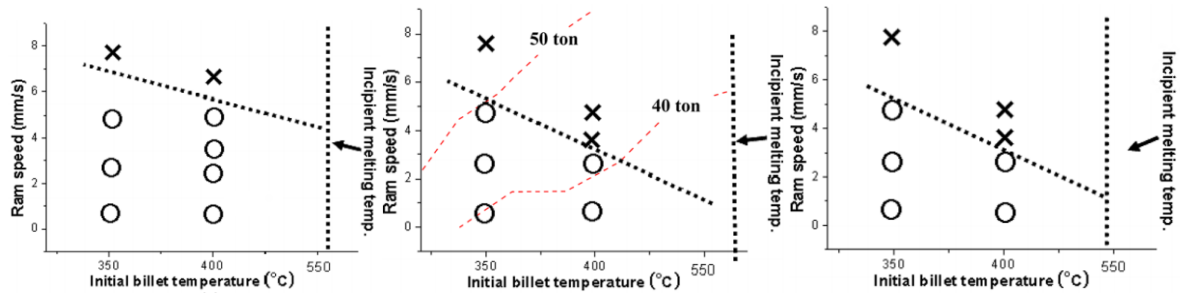


Figure 2-13 Extrusion limit diagram of AA7075 alloys with different Sc additions: 0% Sc (left), 0.11%Sc (middle), 0.3%Sc (right) [53].

Some extrusion limit diagrams incorporating other information were also developed. Clade and Sheppard [52] developed an ELD that contains the contour maps of the subgrain and surface roughness to describe how the extrusion process variables affect the microstructure and the surface quality of the extrusion profile. Donati and Tomesani [54] investigated the correlation between the die geometry and the production limit. The feeder dimensions (cross section areas of 13000 mm<sup>2</sup> and 7000 mm<sup>2</sup>) and welding chamber heights (10 mm, 23 mm, and 36 mm) were investigated in this literature. The ELD is shown in Figure 2-14, where the defect limit curves were obtained by those experimental points with defects labeled by red circle. The bigger feeder size can make the material extrude at a higher extrusion speed. When the feeder size is constant, a larger chamber height allows higher extrusion speed.

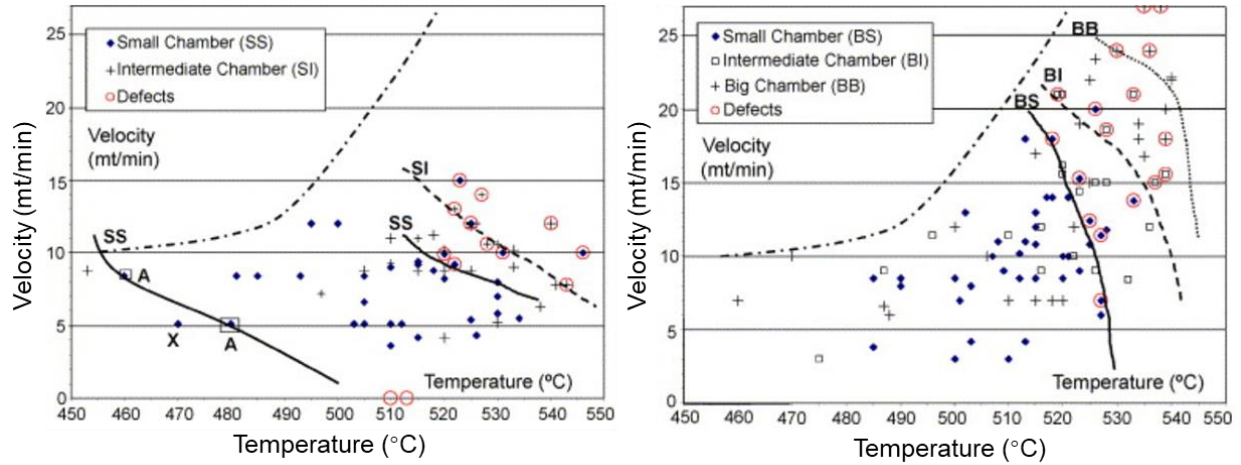


Figure 2-14 ELD for small feeder (left) and big feeder (right) [54].

Except aluminum alloy, ELD was also constructed for other material to guide the parameters choosing during the extrusion process. Sun et al. constructed an ELD for the superalloy Inconel 690 with a high nickel content, based on hot processing map. Bai et al.[55] constructed the ELD for magnesium alloy by using artificial neural network method. YeLapovok [56] built the ELD of AZ31 by FE simulations and the extrusion speeds and ratios were qualified as a function of the initial billet temperature. Barnett et al. [57] built the ELDs of Mg-Al-Zn alloys using the empirical models. It was found that a higher Al content shrank the extrusion process windows by comparing the limit diagrams of the alloys with different Al contents. Wang et al. developed the ELDs for AZ31 and AM30 by using their flow stress data and found that AM30 shows a better extrudability than AZ31. Lee et al. [58] constructed the ELD for AZ91-0.9Ca-0.6Y-0.5MM alloy using the extrusion data and when the material is extruded using the parameter with the safe extrusion zone, products with high surface quality were obtained.

In conclusion, most of the literature on ELDs are focused on magnesium alloy. A few pieces of the literature are about aluminum alloy. However, little work was done on the ELD of AA6xxx, especially AA6xxx alloys with Cu additions.

## **2.5 Hot deformation behavior and constitutive models for Al-Mg-Si-Cu alloys**

A good understanding of the hot deformation behavior and accurate constitutive model of the material is needed to understand the deformation in the actual manufacturing process. The constitutive model fitted from the hot deformation behavior is a necessary input for mathematical modelling. During the hot extrusion process, homogenized billets are preheated to a high temperature and then extruded immediately. The material goes through significant deformation during a very short time.

### **2.5.1 Hot deformation behavior of AA6xxx aluminum alloys with Cu additions**

Much research has been done on the hot deformation behavior of AA6xxx alloys [59–62]. The flow stress of the material is closely related to the detailed chemical composition and initial microstructure and is also very sensitive to the temperature and strain rate. The flow stress usually increases quickly with the increase of the strain and reaches a peak flow stress at a small strain. For AA6xxx aluminum alloys, a flow stress close to steady follows the peak stress due to the high stacking fault energy of aluminum that is favorable to dislocation glide or slip [63], which counteracts the strain hardening effect during the deformation.

Xu et al. [64] studied the hot deformation behavior of Al-0.85Mg-1.0Si-0.44Cu alloy containing Mn and Cr. The material was obtained by DC casting, and then homogenized at 560°C for 4 hours followed by air cooling. Hot compression tests were carried out using the Gleeble™

3500. Referring to Figure 2-15, the flow stress increased with the decrease of the temperature and increase of the strain rate. The flow stress shows a steady state after the peak stress at deformation temperatures higher than 500°C.

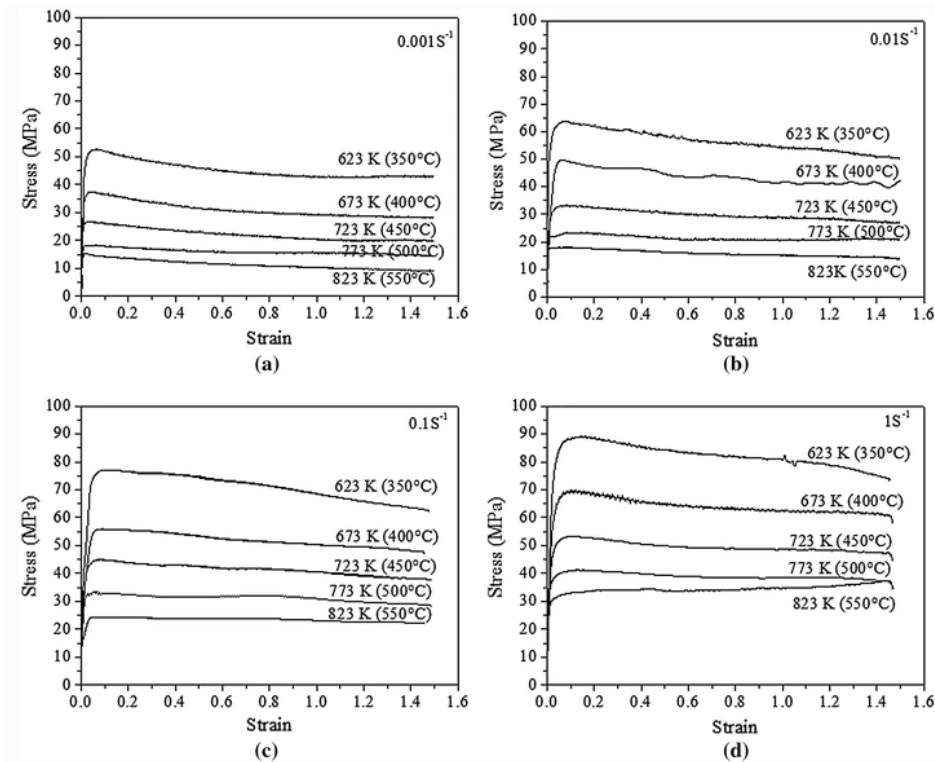


Figure 2-15 Measured stress-strain curves for Al-Mg-Si-Cu alloy at different temperatures and strain rates [64].

Yang et al. [65] studied the hot deformation behavior of 6A82 containing 0.46% Cu. The material was homogenized at 560°C for 6h followed by water quenching. The flow stress curves showed a similar trend as that of Xu [64]. Wang et al. [66] studied the hot deformation behavior of AA6061(1.08Mg-1.06Si-0.34Cu) that was homogenized at 555°C for 6h followed by air cooling as shown in Figure 2-16. The true stress reaches a plateau following the rapid increase at

the initial stage of the deformation. The plateau is due to the equilibrium between the work hardening and dynamic softening.

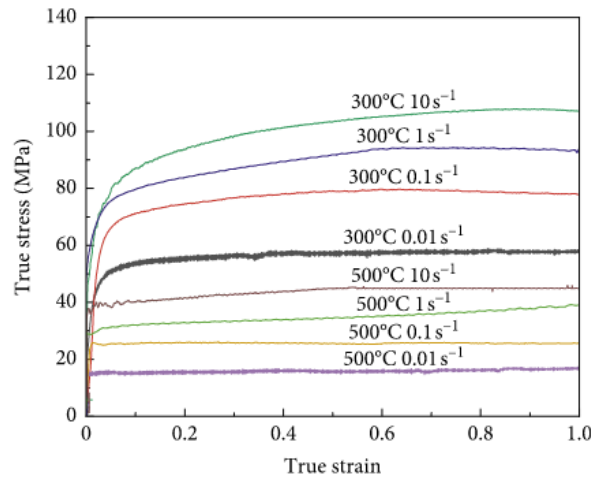


Figure 2-16 Measured flow stress curves of AA6061 at different deformation temperatures and strain rates [66].

In summary, some research has been done to measure the hot flow stress curves of Al-Mg-Si-Cu alloys, and at a higher deformation temperature, the flow stress curves reach a steady state. However, the effect of different levels of Cu in these alloys on the hot flow stress has not been systematically investigated.

### 2.5.2 Constitutive equations

Choosing the right constitutive model is important to understand the flow behavior of the material and model the manufacturing process the material undergoes accurately. During the extrusion process, the AA6xxx alloys experience high temperatures that can be up to 600°C and high strain rates [67]. Many different constitutive models have been developed to predict the plastic flow behavior of the 6xxx aluminum alloys at different temperatures and strain rates.

According to their construction processes and principles, those models can be classified into three categories: physical models, artificial neural network (ANN) models, and phenomenological models. The physical model mainly considers the effect of microstructure evolution on the mechanical properties [68,69]. The ANN models usually use artificial intelligence methods to simulate the complex nonlinear deformation behavior of the material [70]. The phenomenological models usually use empirical equations to describe the relationship between the flow stress and the deformation parameters, including the strain rate, the deformation temperature, and the strain. The material constants in the equation are few and can be obtained using mathematical methods easily. So, the phenomenological models are widely used. The most common phenomenological models include Johnson-Cook (JC) model, modified JC model, Arrhenius-type model, strain-compensated Arrhenius-type model, and Sellar-Tegart hyperbolic sine-type model. In aluminum alloys, two commonly used empirical constitutive models are Johnson-Cook model [71] and Sellar-Tegart model [72].

### **Johnson-Cook (JC) Model**

JC model was first proposed by Johnson and Cook in 1983 and is widely used due to its mathematical simplicity and high accuracy, which can be expressed as the form:

$$\sigma = (A + B\varepsilon^n)\left(1 + C \ln \frac{\dot{\varepsilon}}{\dot{\varepsilon}_0}\right)\left(1 - \frac{T - T_r}{T_m - T_r}\right)^m \quad 2-1$$

Where  $\sigma$  is the flow stress,  $\varepsilon$  is the plastic strain,  $\dot{\varepsilon}$  is the plastic strain rate,  $\dot{\varepsilon}_0$  is the reference strain rate,  $T_m$  and  $T_r$  are melting temperature and room temperature respectively, A, B, C, n and m are material constants. In this model the first expression is the strain hardening effect, the second expression represents the strain rate hardening effect and the third expression accounts for the thermal soft effect. This model is good for describing the constitutive behavior of material

experiencing large deformation, high strain rate and high temperature [73]. The parameters in this model are coupled due to the multiplicative nature of the model [74]. Three effects are independent of each other from Eq. 2-1. Based on this model, lots of modified JC model have been developed [73,75,76] and can predict the flow stress more accurately.

### **Sellars-Tegart model**

The constitutive model proposed by Sellars and Tegart [72] can be used to describe the steady state deformation behavior of material and is expressed as the Eq.2-2:

$$\dot{\epsilon} = A[\sinh(\alpha\sigma)]^n \exp\left(-\frac{Q}{RT}\right) \quad 2-2$$

Where  $\dot{\epsilon}$  is the strain rate of deformation, A, n and  $\alpha$  are material constants, Q is the deformation activation energy (kJ/mol), R is the gas constant (8.318 J/mol/K), T is the absolute deformation temperature (K). The Zener-Holloman parameter is the temperature compensated strain rate and can be expressed as Eq. 2-3

$$Z = \dot{\epsilon} \exp\left(\frac{Q}{RT}\right) \quad 2-3$$

By combining Eq. 2-2 and Eq. 2-3, the final expression of Sellars and Tegart is shown in Eq. 2-4, which can be used on a wide range of strain rates and temperatures [72].

$$\sigma = \frac{1}{\alpha} \ln \left[ \left(\frac{Z}{A}\right)^{\frac{1}{n}} + \left(\left(\frac{Z}{A}\right)^{\frac{2}{n}} + 1\right)^{\frac{1}{2}} \right] \quad 2-4$$

This model has been successfully used to predict the steady state flow stress influenced by strain rate and temperature for aluminum alloys [61,77]. Some literature also incorporated other factors into the model. Langkruis et al. [78] determined the parameter A in the model as a function of the amount of Mg and Si in solid solution of the AA6xxx alloys that went through different pretreatment conditions. Haghdam et al. [79] developed the constitutive model of A356 aluminum



alloy based on the Sellar Tegart model. They believed that the deformation activation energy and other material constants were strain dependent and incorporated strain into the model.

## **2.6 Modeling of AA6xxx alloy extrusion process**

The extrusion process is very complicated and can be affected by many factors, such as the chemical composition of the billets, the microstructure before extrusion, the initial billet temperature, ram speed, and die geometry, etc. Modeling is an effective way to reveal in a quantitative way how these parameters can influence the temperature distribution, strain and strain rate experienced by the material in this process.

Many studies have been done on the thermomechanical modeling of extrusion process of aluminum alloys, including AA1xxxx, AA2xxx, AA3xxx, AA6xxx, AA7xxx [80–87], especially for AA6xxx alloys. The temperature history, material flow speed, load, strain, and strain rate during extrusion process could be determined via mathematical modeling. Figure 2-17 demonstrates the model predicted temperature and strain rate of a bar extrusion using the zero-bearing die and the choked die.

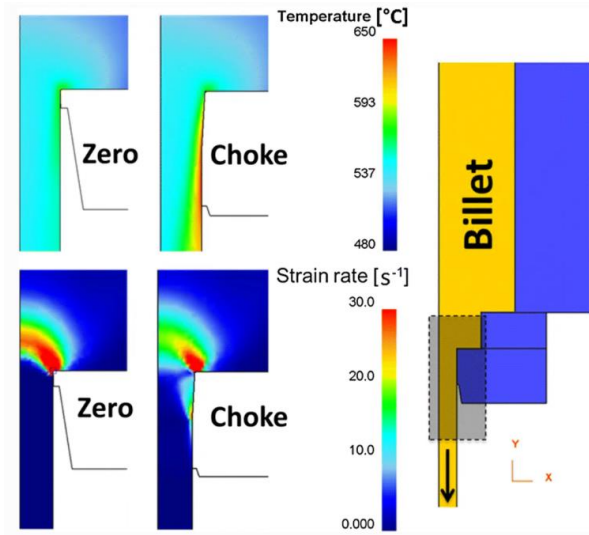


Figure 2-17 Model predicted temperature and strain rate distribution during a bar extrusion [87].

In addition, the extrusion modeling could also be used to optimize the die geometry [88], and study the effect of different extrusion speeds and initial billet temperature on the extrusion process [81].

Two important parameters during extrusion process are the heat transfer coefficient and the friction coefficient between the billet and the tooling. The heat transfer coefficient is considered to be in the range of 11-25 kW/(m<sup>2</sup>·K) and the convective heat transfer coefficient usually takes the value of 10 W/(m<sup>2</sup>·K) [50,81]. Friction exists between the billet and the tooling, which can affect the load needed, the temperature distribution and the material flow pattern. The friction has not been studied thoroughly and its quantitative expression is still not clear. Different friction coefficients have been used in literature. Some researchers [50,81,89] considered the friction between the billet and the container as shear friction and the friction coefficient is 0.8-0.9, whereas

some consider the contact relationship as sticking [90]. For the friction between the billet and the die, the friction coefficient is between 0.3-0.4 [50,81,90,91].

Much research has been done on the simulation of extrusion by using commercial finite element software, such as DEFORM<sup>TM</sup>, FORGE<sup>TM</sup>, HyperXtrude<sup>TM</sup> [50,81,83,89,91]. DEFORM<sup>TM</sup> is a popular one in all of the software.

## **2.7 Summary**

Significant research work has been done on the extrusion of AA6xxx alloys with and without Cu additions. However, most of the work for the Cu containing AA6xxx alloys has focused on the microstructure changes and mechanical properties after different heat treatment methods. Some work has been done on the effect of different Cu additions in AA6xxx alloys on the hot deformation behavior of the material. The surface defects, especially the surface cracking of the AA6xxx alloys during the extrusion process using different die geometries, are not studied systematically. The impacts of Cu addition in AA6xxx alloy, die geometry, and extrusion ratio on the extrudability of the materials are not studied systematically yet.

## Chapter 3 Scope and Objectives

Currently the most widely used AA6xxx aluminum alloy in the automotive industry with the highest extrusion strength is AA6082, which is processed to have an un-recrystallized, fibrous microstructure. This alloy has a yield stress of 320 MPa and a true strain to failure of 0.6. This research is being conducted with the aim of developing extruded AA6xxx aluminum alloys with higher strength while maintaining satisfactory ductility to satisfy the future market demand for aluminum alloy extrusions. The overall scope of this research is to study the effect of different Cu additions and die geometries on the extrudability of AA6xxx alloys. To better understand the effect of Cu, it is necessary to perform a series of experiments and develop and verify a mathematical model of the extrusion process.

This research focuses on understanding the effect of Cu and die geometries on the extrudability of AA6xxx alloys. A more scientific objective of this research is to gain a better understanding of the conditions that lead to surface cracking during the extrusion of AA6xxx aluminum alloys. The research includes experiments in the form of extrusion trials, numerical modelling of the extrusion process using DEFORM<sup>TM</sup> 2D, and characterization of the extruded material. With different percentages of Cu added into AA6xxx alloys, the properties of each material are different, which influences the variables during extrusion. In addition, a variety of die bearing geometries were used to produce the same final extrudate shape to understand how the local strain rate, stress, and temperature affect surface cracking of these alloys. Although some research has been done on the effect of Cu on the mechanical properties and microstructure, little research has been done on the modelling and the construction of extrusion limit diagram with various Cu additions or different die geometries. The detailed objectives of this work are as follows:

- Measure the solidus temperatures of the materials with different Cu levels and develop constitutive models for each material to represent the material behavior by hot compression test on Gleeble™ 3500 and cam plastometer.
- Run extrusion trials for materials with A612 (0.6% Cu) with the extrusion ratio of 70:1 and 17:1, run extrusion trials with different die geometries to see how the die geometries affect the extrusion process with A612 (0.6% Cu), run extrusion trials using 25 mm flat die and 35 mm choked die with A612 (0.6% Cu) and A613 (0.9% Cu) respectively to see how the Cu additions affect the extrudability.
- Examine the surface characteristics of the extrudates with different Cu contents and the extrudates extruded by different die geometries.
- Develop and verify FEM models to represent the extrusion trials for the AA6xxx aluminum alloys with varying Cu levels and the extrusion trials with different die geometries.
- Construct and verify the ELD to show the impact of extrusion ratio, Cu levels, and die geometries on the extrudability of AA6xxx aluminum alloys.
- Understand the stress and temperature distribution where surface cracking is experienced during extrusion in the trials with different Cu additions in AA6xxx alloys and the different die bearing geometries and extrusion ratios.

## Chapter 4 Materials and Methodology

### 4.1 Start material

The materials studied in this research were all provided by the Rio Tinto Alcan's Research and Development center (ARDC) in Arvida, Quebec. Three different Al-Mg-Si-Cu alloys were cast into extrusion billets with 101.6 mm in diameter and 200 mm in height. The chemical compositions of these alloys are listed in Table 4-1. This research focuses on the study of A611, A612, and A613 with Cu additions of 0.3%, 0.6%, and 0.9%, respectively. The optical microstructures and SEM images of the three materials are shown in Figure 4-1 and Figure 4-2. The as-cast aluminum alloys show a dendritic structure with the micro-segregation of constituent particles in the inter-dendritic area. The SEM images in Figure 4-2 were obtained by our co-workers at UBC.

Table 4-1 Chemical compositions of different Al-Mg-Si-Cu alloys (wt.%) used in this research.

Alloys	Cu	Fe	Mg	Mn	Si	Ti	Cr	V	Al
A576	0	0.19	0.69	0.52	1.01	0.02	0.15	0.01	Bal.
A611	0.3	0.20	0.71	0.51	1.04	0.02	0.15	0.01	Bal.
A612	0.59	0.20	0.69	0.51	1.02	0.02	0.15	0.01	Bal.
A613	0.9	0.22	0.70	0.51	1.03	0.02	0.15	0.01	Bal.

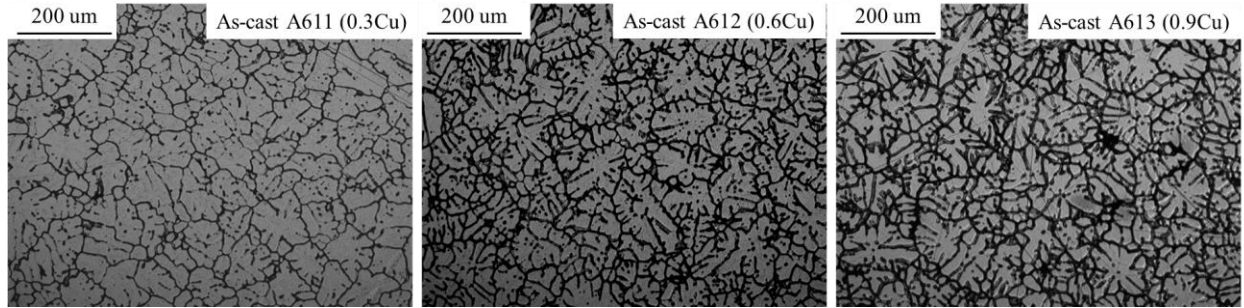


Figure 4-1 Optical microstructure of as-cast materials with different Cu additions.

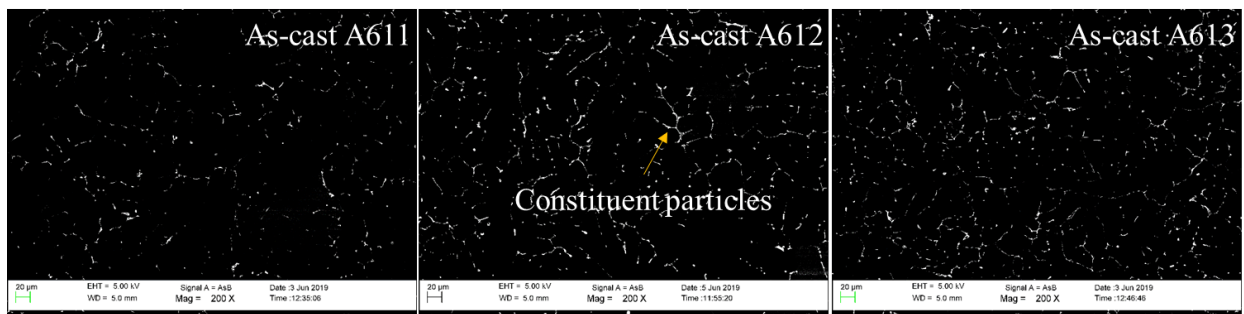


Figure 4-2 Constituent particles of as-cast materials characterized by FEG-SEM.

The as-cast billets were homogenized before extrusion [92]. The homogenization temperature was chosen so that it is below the solidus temperature of the bulk material and above the solvus temperature of the  $Mg_2Si$  so that  $Mg_2Si$  can go into the solid solution. Thermo-Calc<sup>TM</sup> software was used to calculate the  $Mg_2Si$  solvus temperature and melting temperature of different alloys studied in this work. The solvus temperatures of  $Mg_2Si$  and the predicted melting temperatures for the different alloys are shown in Table 4-2. The homogenization temperature was chosen based on the Thermo-Calc results. The thermal history of the homogenization process is shown in Figure 4-3. The billets were heated to 500°C at the rate of 250°C /h, and then heated up to 550°C at a heating rate of 50°C /h. The billets were held at 550°C for 2h. Then the billets were water-quenched immediately to maintain the homogenized microstructure. This procedure was

done at UBC to provide samples for characterization but also at Rio Tinto for any billets that were subsequently extruded. Both UBC and Rio Tinto used the same material.

Figure 4-4 are the microstructures of the billets with different Cu additions after homogenization. Notably, less dendrites were observed after homogenization.

Table 4-2 Calculated Mg<sub>2</sub>Si solvus temperature and melting temperatures of different alloys via Thermo-Calc using the TTAL6 database.

Alloys	A576	A611	A612	A613
Mg <sub>2</sub> Si solvus temperature (°C)	540.1	543.9	538.9	538.9
Equilibrium melting point (°C)	592.9	583.9	578.9	571.9

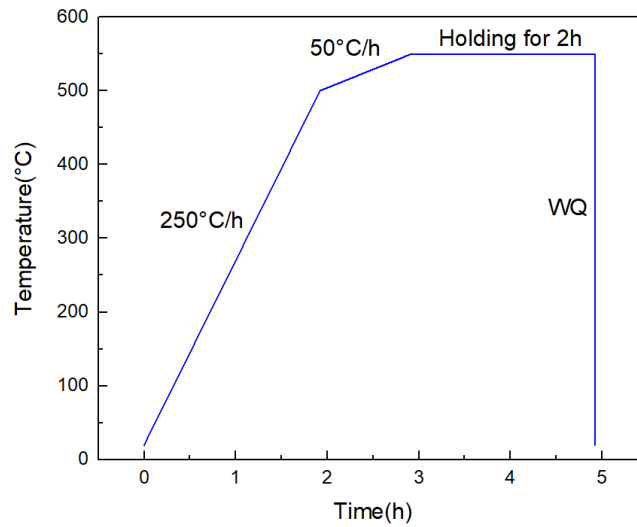


Figure 4-3 Thermal history of the homogenization process used on the billets (WQ = water quench).



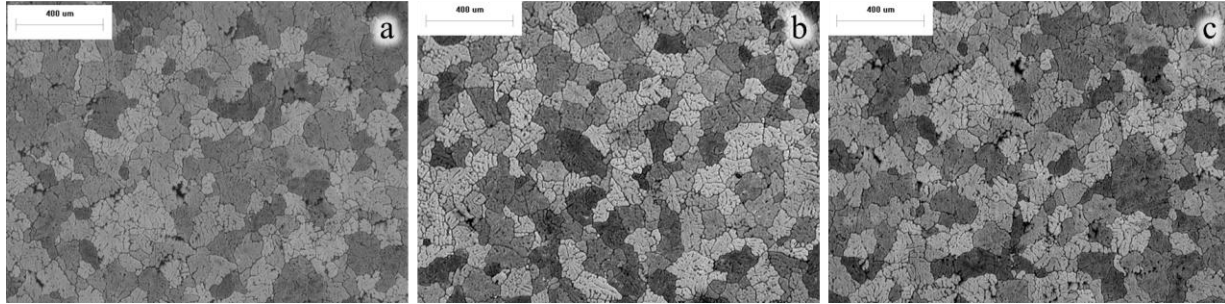


Figure 4-4 Microstructure of the billets after homogenization with different Cu contents:  
(a)A611, (b) A612, and (c) A613.

## 4.2 Characterization

### 4.2.1 Differential Scanning Calorimetry

Differential Scanning Calorimetry (DSC) is a thermal analytical technique in which the difference in heat to increase the temperature of the sample and the reference material is measured as a function of temperature. The heat absorbed or released is indicated in the form of endothermic or exothermic peaks, from which the solidus temperature can be determined.

In order to obtain the solidus temperature of the homogenized material and analyze the phase change before and after homogenization, DSC tests were done on both the as cast and homogenized A576, A611, A612, and A613 using NETZSCH™ DSC 404C Pegasus thermal analyzer. The A576 is included to provide a baseline result with no Cu. There are two crucibles in the equipment chamber, one for the sample and the other for the reference sample. In this research, the empty crucible was used as the reference. The machine was calibrated using high-purity material (Indium) prior to the measurements.

As shown in Figure 4-5, the received billet has a diameter of 101.6 mm. One slice around 3 mm was taken from one end of the billet first, then two samples ~50 g were taken out from the slice, one from the center and one from the edge of the billet. Samples were cut from the bulk material and ground so that the material can fit in the crucible and touch the crucible bottom well. Argon gas was used as protective gas. After the sample was placed into the DSC machine, the chamber was evacuated twice before it was refilled with argon gas. The sample was heated at the rate of 10°C/min up to 700°C under the protection of argon atmosphere and the flow rate of the protection gas is 150 ml/min. Three tests were repeated for each location.

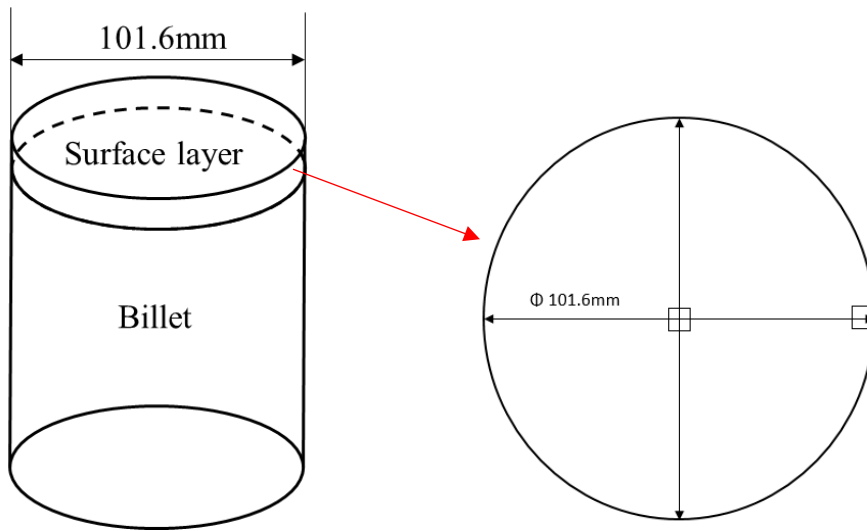


Figure 4-5 Schematic showing DSC sample locations on the billet.

#### 4.2.2 Hot compression test

To obtain the true stress-true strain curves of the alloys, hot compression tests at the strain rates of 0.1/s, 1/s and 10/s and the deformation temperatures of 450°C, 500°C, and 550°C were conducted on the Gleeble™ 3500 thermal-mechanical testing machine at the University of

Waterloo. The tests at strain rates of 50/s and 100/s and a deformation temperature of 550°C were performed on the cam plastometer at the University of Tokyo in Japan.

For the compression tests on the Gleeble<sup>TM</sup> 3500, since the testing temperature was at or greater than 500°C, a low force jaw setup was used since it can measure the force more accurately for low force conditions. A thermocouple was welded in the middle of the test sample to monitor the temperature change during the test. A C-strain dilatometer was used to record the change of the sample in diameter during compression, as shown in Figure 4-6. A certain amount of nickel paste as lubrication was manually and uniformly applied between the anvils and the specimen to reduce the friction. The dimensions of the hot compression samples are 8 mm in diameter and 12 mm in height. All test samples were heated up at the rate of 250°C/min to the test temperature, and then held for 1 min to ensure the temperature distribution of the sample is uniform before being compressed, as shown in Figure 4-7. Hot compression tests were conducted on the homogenized A611, A612, and A613. The true strain and true stress were calculated using the following equations:

$$\varepsilon = \ln\left(\frac{d_0}{d_0 + \Delta d}\right) \quad 4-1$$

$$\sigma = \frac{F}{\frac{\pi(d_0 + \Delta d)^2}{4}} \quad 4-2$$

Where  $\varepsilon$  and  $\sigma$  is the true strain and true stress,  $d_0$  is the initial sample diameter before compression,  $\Delta d$  is the change in diameter and  $F$  is the force applied to the sample.

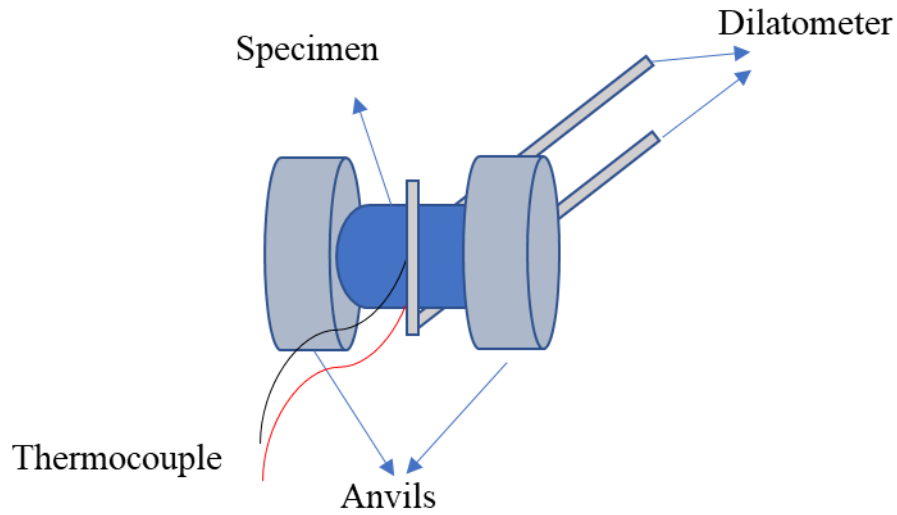


Figure 4-6 Schematic of the jaw set for high temperature compression test done using the Gleeble™ 3500 with dilatometer to measure the change in diameter for the sample.

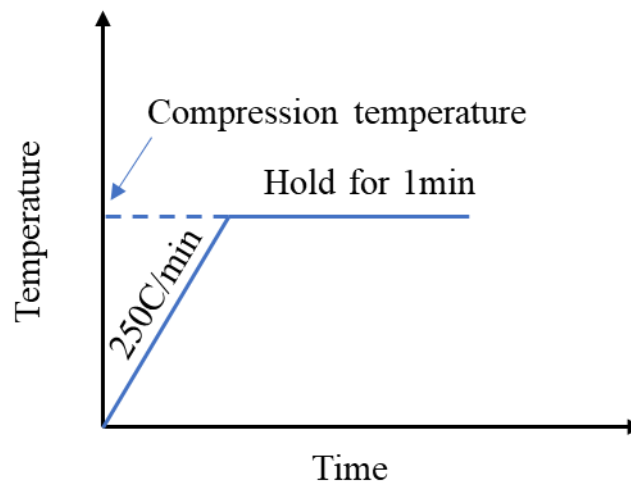


Figure 4-7 Temperature history of the sample when tested on Gleeble™ 3500 and cam plastometer.

During the extrusion process the material goes through large deformation in a short period of time, which means the material deforms at strain rate that can reach several hundreds per second.

The maximum strain rate the Gleeble™ 3500 can obtain is typically 10/s, while Cam plastometer testing machine can operate at a true strain rate of up to 200/s. With both the low strain rate and the high strain rate compression data, a more precise constitutive model can be obtained.

For the compression test on the cam plastometer, the sample size is the same as that of the sample for the Gleeble™ 3500 test. Before compression, a K-type thermocouple is welded in the middle of the sample to monitor the temperature. Then the sample is heated up at a rate of 250C/min to the test temperature, held for 1 min before being compressed. The sample is protected by Nitrogen to avoid oxidation on the sample surface. The total compression is 8 mm, as shown in Figure 4-8. Because the C gauge dilatometer is not used, the equations that are used to calculate the true stress and true strain are different from the ones that are used for the test on Gleeble™ 3500. The assumption is that the volume of the sample keeps constant during the test. The equations used to calculate the true stress and true strain are as following:

$$\varepsilon = \ln\left(\frac{l_0}{l_0 - \Delta l}\right) \quad 4-3$$

$$\sigma = \frac{F}{\frac{\pi d_0^2 l_0}{4(l_0 - \Delta l)}} \quad 4-4$$

Where  $\varepsilon$  and  $\sigma$  is the true strain and true stress,  $d_0$  is the initial sample diameter before compression,  $l_0$  is the initial height of the sample,  $\Delta l$  is the change in height and  $F$  is the force applied to the sample.

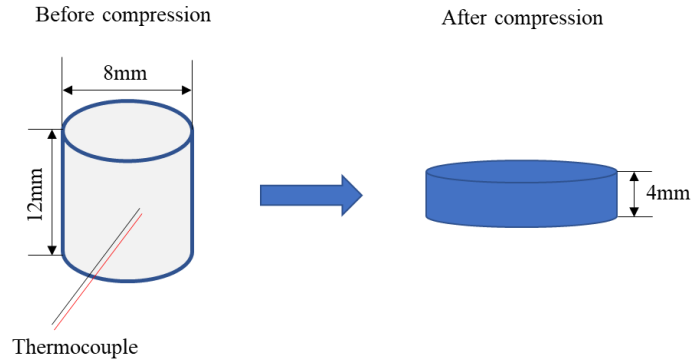


Figure 4-8 Schematic of the compression sample used for the cam plastometer.

Table 4-3 summarizes the tests that were run on the Gleeble™ 3500 and the cam plastometer. For each condition, three tests are repeated.

Table 4-3 Summary of the compression tests on Gleeble™ 3500 and cam plastometer.

Material	Tests on Gleeble™ 3500		Tests on cam plastometer	
	Temperature (°C)	Strain rates (1/s)	Temperature (°C)	Strain rates (1/s)
A611 (0.3%Cu)	450, 500, 550	0.1, 1, 10	550	50, 100
A612 (0.6%Cu)	450, 500, 550	0.1, 1, 10	550	50, 100
A613 (0.9%Cu)	450, 500, 550	0.1, 1, 10	550	50, 100

### 4.3 Extrusion trials

Three extrusion trials were run at Rio Tinto Alcan's Arvida Research and Development Center (ARDC) in Jonquiere, Quebec. A 750-ton extrusion press was used. A schematic view of

the setup of the extrusion process and the water quench tank is shown in Figure 4-9. For all the extrusion trials, the billets have a diameter of 101.6 mm, and a length of 400 mm or 200 mm. 20 mm of the billet was scraped to avoid back-end defects. A certain amount of the front extrusion bar was cut for scrap. The water quenching tank is located 2.5m away from the die exit. The purpose of these extrusion trials was to help understand the conditions under which surface cracking will occur for each of the alloys, die configurations and extrusion conditions. Hence for each of the extrusion trials the extrusion speed was increased to try and induce surface cracking.

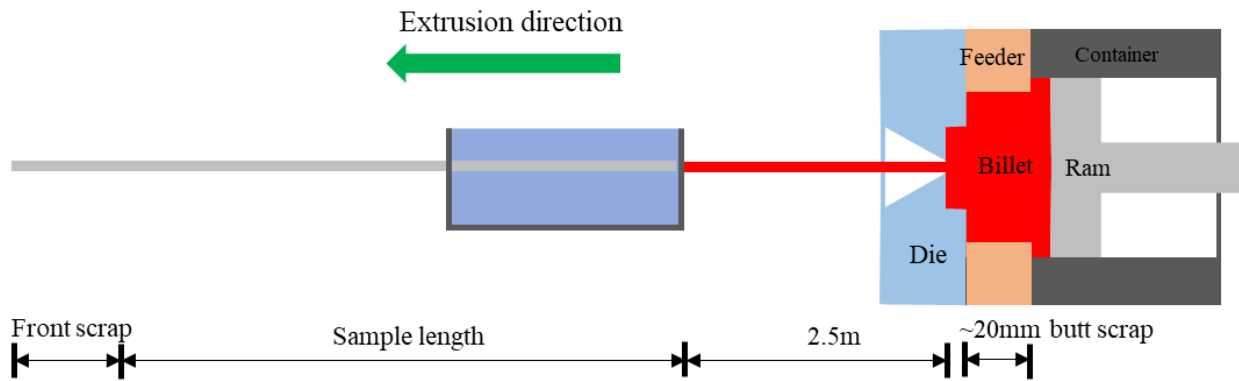


Figure 4-9 A schematic view of the extrusion setup, water quenching tank, and the sample location.

### 4.3.1 Die configurations

There are five parts in the extrusion process as shown in Figure 4-10, which is a schematic view of the extrusion process. There are five main parts in the extrusion process, and they are ram, die, billet, container, and feeder. The red line in the figure indicates the die bearing. In this work different die bearing geometries were used.

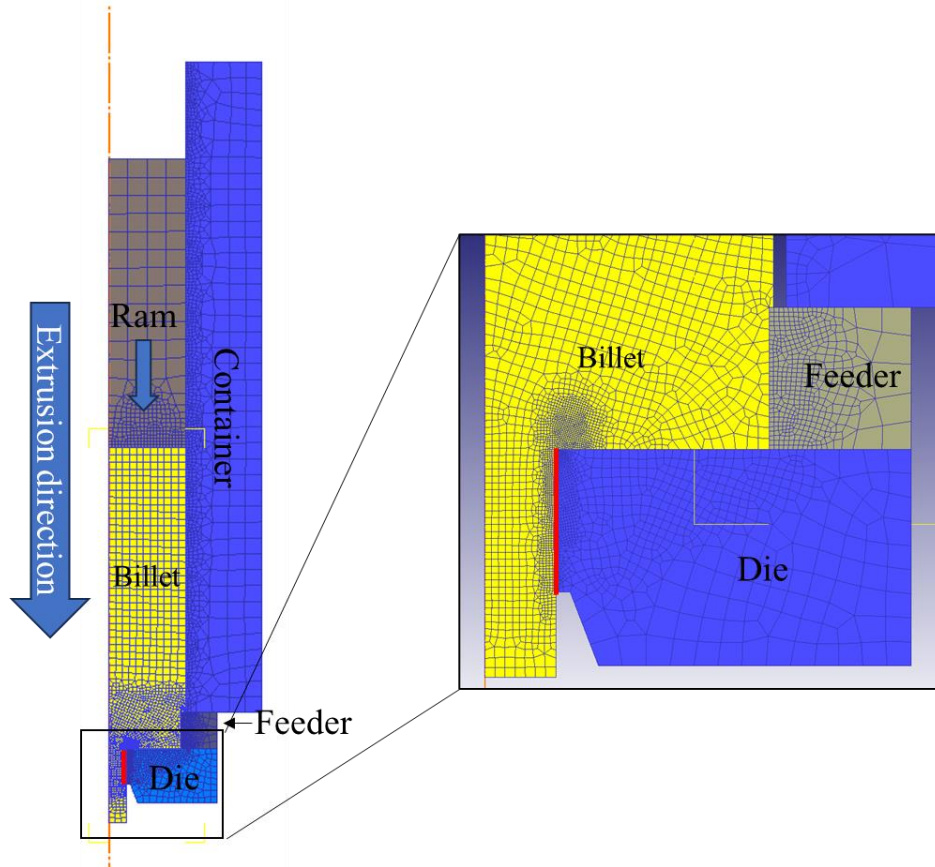


Figure 4-10 A schematic view of the extrusion process with five parts including ram, die, billet, container, and feeder.

The die geometries used for the different extrusion trials and the thermocouple locations in the die bearing regions are shown in Table 4-4.

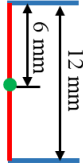
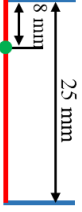
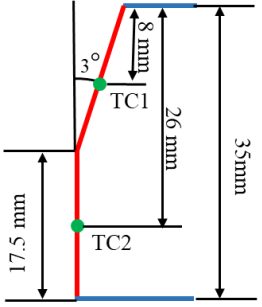
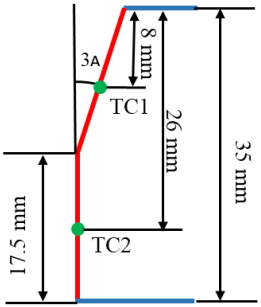
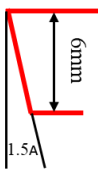
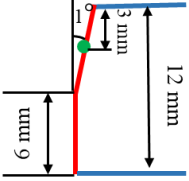

In extrusion trial #1, the billet length is 400 mm, and the feeder has a diameter of 60 mm and height of 25 mm. The extrusion bar diameter is 12.5 mm. The die bearing length is 12 mm. In extrusion trial #2, four different die geometries are used, which are 25 mm flat die, 35 mm choked die with 3 degrees choked angle for half of the die bearing close to the die front, zero-bearing die, and 12 mm choked die with a 1 degree choked angle for half of the die bearing close to the die front. The extrusion bar diameter is 25 mm, and the feeder size is 100 mm in diameter and 25 mm



in height. Both the extrusion trial #1 and #2 use A612 material and there is no stopping during the whole extrusion process. In extrusion trial #3, 35 mm choked die and 25 mm flat die are used. The extrusion material is A613. The feeder size is the same as that in extrusion trial #2.

For each extrusion trial, four starting extrusions were run to warm up the extrusion press. After extrusion the profiles were water quenched in the water tank to the room temperature, and then cut to 1m length to be shipped to University of Waterloo to be examined and characterized.

Table 4-4 Die bearing geometries (blue lines) used for different extrusion trials and illustrations showing the locations of the thermocouples (green dots) for the different die geometries (TC = thermocouple). Extrusion direction is from top to bottom, and red line is the die bearing.

Extrusion trial #1 (A612)	Extrusion trial #2 (A612)		Extrusion trial #3 (A613)
Feeder size: $\Phi 60$ mmx25 mm	Feeder size: $\Phi 100$ mm x 25 mm		Feeder size: $\Phi 100$ mmx25 mm
12 mm flat die	25 mm flat die	35 mm choked die	35 mm choked die
			
	Zero bearing die	12mm choked die	25mm flat die
			

### 4.3.2 Extrusion parameters

Table 4-5, Table 4-6, and Table 4-7 show the extrusion billet temperature, extrusion speed, and material used for each extrusion trial. For extrusion trial #1, the initial billet temperature and the container and die temperature was both 475°C and the extrusion speed is from 4 mm/s to 10 mm/s. The extrusion ratio is 70:1. For extrusion trial #2, four different die geometries were used. The initial billet temperature was all set to be 500°C and the container and die temperature were both 480°C. The extrusion ratio is 17:1. Both the extrusion trial #1 and #2 used the A612 material. Extrusion trial #3 was conducted on A613 using both the 25 mm flat and 35 mm choked dies.

Table 4-5 Extrusion parameters for extrusion trial #1 (Extrusion ratio = 70:1).

No.	Material	Billet temperature (°C)	Extrusion speed (mm/s)
1	A612	475	4
2	A612	475	5
3	A612	475	6
4	A612	475	7
5	A612	475	8
6	A612	475	9
7	A612	475	10

Table 4-6 Extrusion parameters for extrusion trial #2 (Extrusion ratio = 17:1).

25 mm flat die	Material	Billet temperature (°C)	Extrusion speed (mm/s)
1	A612	500	20
2	A612	500	22
3	A612	500	24
4	A612	500	26
5	A612	500	28
6	A612	500	31
35 mm flat die	Material	Billet temperature (°C)	Extrusion speed (mm/s)
1	A612	500	22
2	A612	500	24
3	A612	500	26
4	A612	500	28
5	A612	500	30
6	A612	500	32
7	A612	500	34
8	A612	500	36
9	A612	500	38
10	A612	500	40
12 mm choked die	Material	Billet temperature (°C)	Extrusion speed (mm/s)
1	A612	500	24
2	A612	500	26
3	A612	500	28
4	A612	500	28
5	A612	500	30
6	A612	500	29
7	A612	500	27
8	A612	500	26
Zero-bearing die	Material	Billet temperature (°C)	Extrusion speed (mm/s)
1	A612	500	26
2	A612	500	28
3	A612	500	30
4	A612	500	32
5	A612	500	28
6	A612	500	34
7	A612	500	27
8	A612	500	36
9	A612	500	38

Table 4-7 Extrusion parameters for extrusion trial #2 (Extrusion ratio = 17:1).

25 mm flat die	Material	Billet temperature (°C)	Extrusion speed (mm/s)
1	A613	500	10
2	A613	500	15
3	A613	500	20
4	A613	500	15
35 mm choked die	Material	Billet temperature (°C)	Extrusion speed (mm/s)
1	A613	500	5
2	A613	500	10
3	A613	500	20
4	A613	500	30
5	A613	500	40
6	A613	500	15

## 4.4 Mathematical model

### 4.4.1 Thermo-mechanical model

The commercial software DEFORM™ 2D is used to simulate the extrusion process for the different die geometries and different materials. DEFORM™ 2D, based on the Lagrangian approach has the advantage of modelling the large-scale deformation with the ability of remeshing and being able to simulate both the transient phase when the billet breaks through the die and the subsequent steady state.

The geometry and mesh of the extruded bar (using the 12 mm flat die simulation model as an example, others are similar as this one) are schematically shown in Figure 4-11. The DEFORM™ 2D model consists of five objects: ram, billet, die, feeder, and container. Since the round bar is axisymmetric, only half of the bar is needed in the model. The billet is assumed to be a rigid-viscoplastic material, and the tooling is defined to be rigid. The billet features a finer mesh closer to the die corner, transitioning into a gradually coarser mesh as it moves away from the die

corner. This design has the potential to enhance both the accuracy and speed of the extrusion process. All other objects are also meshed due to the calculation of the heat transfer between tools.

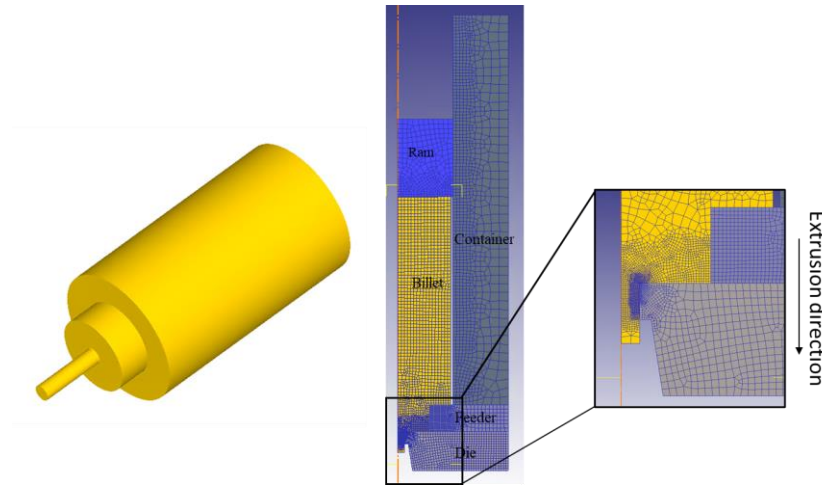


Figure 4-11 Schematic of the bar extrusion (left) and the model and mesh in DEFORM™ 2D (right).

#### 4.4.1.1 Finite Element formulation

For the 2D axisymmetric modelling of extrusion of round bars, the billet was meshed with four-node quadrilateral elements, as shown in Figure 4-11. The metal flow in DEFORM™ simulation is founded upon the minimum work rate principle, which is the velocity distribution that anticipates the lowest work rate represents the most accurate approximation of the actual velocity distribution. This principle states that the material always flows in the path of least resistance. The minimum work rate principal can be expressed mathematically by Equation 4-5 and Equation 4-6. Equation 4-5 describes the work difference between the body forces and the surface tractions, where  $\int_V \bar{\sigma} \dot{\epsilon} dV$  represents the work that is done by the body force or plastic work, and  $\int_S F_i u_i dS$  represents the work done by surface traction. Equation 4-6 demonstrates the way

used to solve for the velocities. The velocities are determined by identifying when the variation in the function becomes zero. This is achieved by integrating the volumetric strain rate and multiplying it with a substantial constant. As the overall solution should equate to zero, it tends to minimize the volumetric strain rate to minimize this integral value.

$$\pi = \int_V \bar{\sigma} \dot{\epsilon} dV - \int_S F_i u_i dS \quad 4-5$$

$$\delta\pi = \int_V \bar{\sigma} \delta\dot{\epsilon} dV - \int_S F_i \delta u_i dS + K \int_V \epsilon_V \delta\epsilon_V dV = 0 \quad 4-6$$

The solutions in Equation 4-6 are the velocities at the nodes, which are four corners of the quadrilateral elements. The velocities can be solved by solving a simultaneous set of equations using a Newton-Raphson iteration method. The convergence criteria were established by considering both velocity and force convergence, with a velocity error limit set at 0.001 and a force error limit set at 0.01.

For the heat transfer analysis in the finite element analysis, the energy balance equation can be written as Equation 4-7, where  $\mathbf{C}$  is the heat capacity matrix,  $\mathbf{K}_C$  is the heat conduction matrix,  $\mathbf{Q}$  is the heat flux vector,  $\mathbf{T}$  is the vector of nodal point temperatures, and  $\dot{\mathbf{T}}$  is the vector of nodal point temperature rate. The  $\mathbf{Q}$  includes a few components and can be expressed with the interpolation function  $\mathbf{N}$  as Equation 4-8. The first item on the right is the heat generated by plastic deformation inside the deforming body with  $k$  being the heat generation efficiency of the heat transferred from mechanical energy to heat.  $k$  is usually with a value of 0.9. The second item is the heat radiated from the environment to the deforming body, where  $\sigma$  is the Stefan-Boltzman constant,  $\epsilon$  is the emissivity,  $T_e$  is the environment temperature,  $T_s$  is the surface temperature. The third item describes the heat convected from the deforming body to the environment, where  $h$  is the convection coefficient. The fourth item is the heat transferred from the deforming body to the tooling through the interface, where  $T_w$  is the workpiece temperature,  $T_d$  is the tooling temperature,

and  $h_l$  is the heat transfer coefficient. The last item is the heat generated by friction between the workpiece and the tooling. The thermal equation is also solved by the Newton-Raphson iteration method with an error limit of 0.00001. [93]

$$C\dot{T} + K_c T = Q \quad 4-7$$

$$Q = \int_V k(\bar{\sigma}\dot{\epsilon})NdV + \int_{S_r} \sigma\epsilon(T_e^4 - T_s^4)NdS + \int_{S_t} h(T_e - T_s)NdS \quad 4-8$$

$$+ \int_{S_c} h_l(T_d - T_w)NdS + \int_{S_c} q_f NdS$$

Both the metal flow equation and the heat transfer equation are solved at each step until the finish of the simulation. The data at the end of each step is saved and used as the initial value for the next step.

#### 4.4.1.2 Material properties

The material data needed in the mathematical model is listed in Table 4-8.

Table 4-8 Material data requirements for extrusion process simulation [94].

	Billet	Tooling
Flow stress	√	
Heat capacity	√	√
Thermal conductivity	√	√
Emissivity	√	√

In this research, the commonly used constitutive model proposed by Sellars and Tegart [72] is used to describe the relationship of the steady flow stress, strain rate and temperature in the simulation of hot extrusion, as is shown in Equation 4-9:

$$A[\sinh(\alpha\sigma)]^n = \dot{\epsilon} \exp\left(-\frac{Q}{RT}\right) \quad 4-9$$

Where  $\dot{\epsilon}$  is the strain rate,  $\sigma$  is the flow stress (MPa),  $T$  is the deformation temperature (K),  $Q$  is the activation energy (kJ/mol),  $R$  is the gas constant (J/mol/K),  $A$ ,  $\alpha$ , and  $n$  are the material constants. The material constants required in this equation were determined from our experimental data, which is in Chapter 5.

The thermal physical properties of AA6xxx and the tooling material H13 are from the material library of DEFROM™ 2D. The thermal physical properties of the studied material and die material are listed in Table 4-9 and the volumetric heat capacity is shown in Figure 4-12, which is the function of the temperature.

Table 4-9 Material thermal physical properties used in the model [94].

Material	Thermal conductivity/(W/m/K)
AA6xxx	180.2
H13	24.3



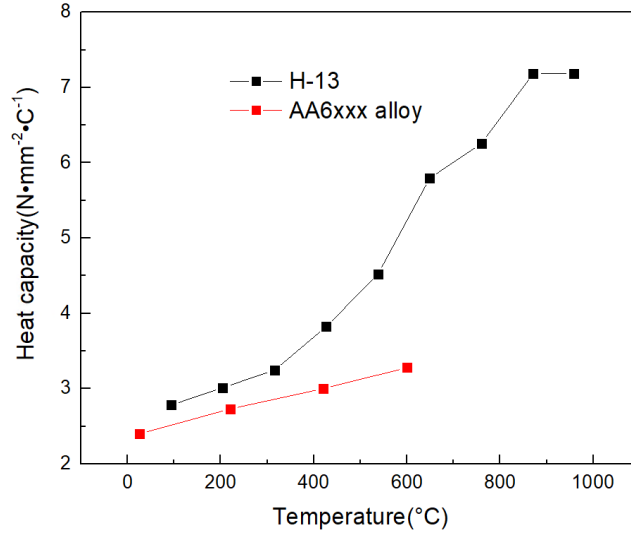


Figure 4-12 Volumetric heat capacity of aluminum alloy and tooling material H-13 [94].

#### 4.4.1.3 Boundary and initial conditions

Two important boundary conditions in the finite element model of extrusion are the friction between billet and the tooling and the thermal exchange between billet and its surrounding environment. Friction is a complicated physical phenomenon. It depends on the material to be extruded and the material of the die, and the interface roughness as well as lubrication and temperature. To model the friction between billet and the tooling, a constant shear friction model was used. The frictional force in the constant shear definition is defined by Eq. 4-10 [94]:

$$f_s = mk \quad 4-10$$

Where  $f_s$  the is frictional stress,  $k$  is the shear yield stress,  $m$  is the friction factor, which usually varies between 0 (frictionless condition) and 1 (full sticking condition). In the simulation, different friction coefficients were defined in the die bearing for different die geometries, which is explained in the friction coefficient justification section 4.4.1.5. The remaining interface of the

billet and tooling used a friction coefficient of 1. The heat transfer coefficient between the billet and the tooling is assumed to be  $25 \text{ kW/m}^2/\text{K}$ . The convective heat transfer coefficient with air is  $0.02 \text{ kW/m}^2/\text{K}$  [94]. It was assumed that 90% of the mechanical work was converted to heat.

#### **4.4.1.4 Mesh size sensitivity**

Mesh size is one of the parameters in the FEM simulation that needs to be determined. If the mesh size is too big, the simulation results are not accurate enough. While smaller size will take longer computation time. It is necessary to study the mesh sensitivity to determine the most suitable element size, at which the accuracy of the simulation results such as temperature, strain rate and extrusion load in this research are not affected significantly by a further decrease of the mesh size and in the meanwhile the results can be obtained in reasonable time.

In this study, the smallest elements are positioned in the die bearing corner, which experiences high strain rates and temperatures as the material passes through. Consequently, several simulations were conducted using various element sizes at the die corner. The die employed is the 25 mm flat die. As depicted in Figure 4-13 mesh windows have been applied to the billet at the die corner. In this arrangement, there are three mesh windows near the die corner, and the ratio between the sizes of adjacent mesh windows remains constant. The innermost mesh window possesses the smallest mesh size. Specifically, minimum element sizes of 0.1 mm, 0.15 mm, 0.25 mm, and 0.5 mm were selected. Figure 4-14 illustrates the effect of the element size on the predicted load from the initial stage of the extrusion to a specific stroke and the temperature distribution from the billet's center to its surface at the die corner. It was observed that the element sizes showed almost no effect on the predicted load, whether it was the initial breakthrough load or the load during subsequent stages of the extrusion process.

Figure 4-15 Effect of minimum element sizes on the predicted effective strain rate (left) and effective strain (right).displays the variations in predicted effective strain rates from the center to the surface of the billet at the die corner. Notably, as the element size increases, there is minimal alteration in the effective strain rates when the distance from the center of the billet is less than 10 mm. On the other hand, as the position approaches the surface, there is an increase in the effective strain rate as the minimum element size decreases. The highest effective strain rates at the surface are as follows: 153/s for an extrusion with a minimum element size of 0.1 mm, 150/s for 0.15 mm, 135/s for 0.25 mm, and 106/s for 0.5 mm. When comparing the effective strain rate between a 0.25 mm element size and a 0.1 mm element size, there is an approximate 10% change in the effective strain rate. Conversely, the effective strains displayed on the right side of Figure 4-14 exhibit nearly identical values for minimum element sizes of 0.1 mm, 0.15 mm, and 0.25 mm. Given computational efficiency concerns, a minimum element size of 0.25 mm has been selected for all the simulations done for this research.

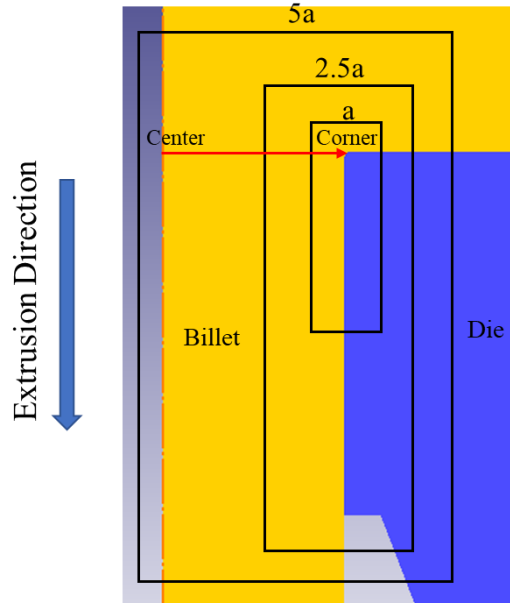


Figure 4-13 Mesh windows at die corner.

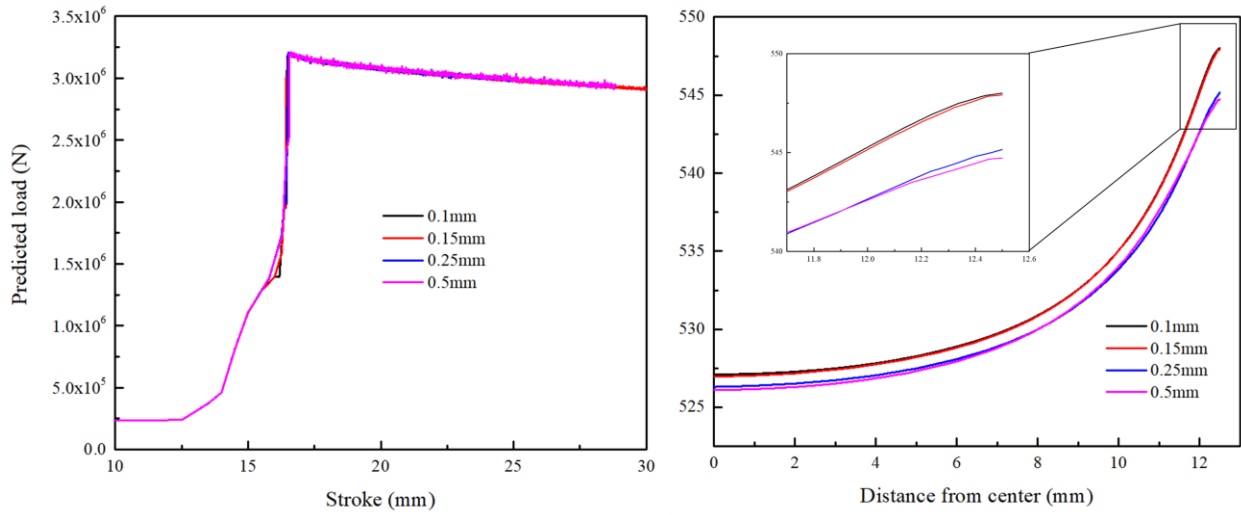


Figure 4-14 Model-predicted temperature from the center to the surface of the bar at the die corner (left) and model-predicted breakthrough load (right) showing the influence of minimum element size.

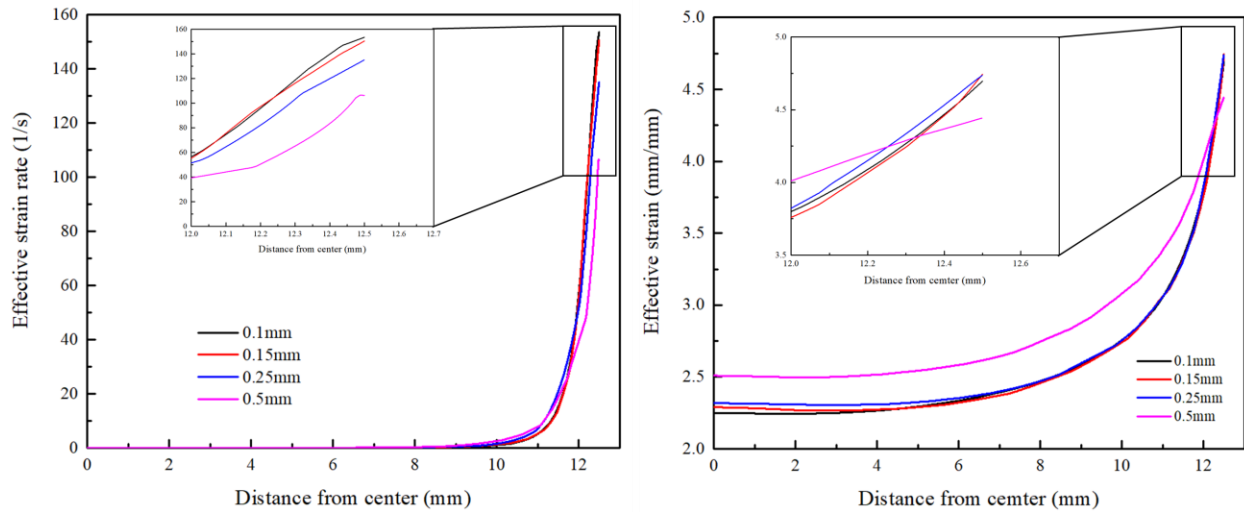


Figure 4-15 Effect of minimum element sizes on the predicted effective strain rate (left) and effective strain (right).

#### 4.4.1.5 Friction coefficient justification

Frictional force is described as the force that hinders the relative motion of two objects in contact. During the extrusion process, frictional forces come into play between various components: the billet and the dummy block, the billet and the container, and the billet and the die bearing. The frictional force between the billet and the dummy block is often less scrutinized due to its limited impact on the extrusion process. Typically, the contact condition between the billet and the container is assumed to be sticking [41,95]. The friction condition at the die bearing is complex and depends on the specific die geometries. The die geometries have been categorized into three groups by Sanabria Rosas [96], as illustrated in Figure 4-15, with each group corresponding to different frictional conditions. In the case of a choked die bearing, depicted in Figure 4-15 (a), a portion of the bearing adheres to the billet, and the extent of this adherence is dependent on the overall length of the die bearing. For the flat die, as seen in Figure 4-15 (b), slip

conditions are typically encountered. Figure 4-15 (c) illustrates that in the relief die bearing configuration, there is no contact between the components.

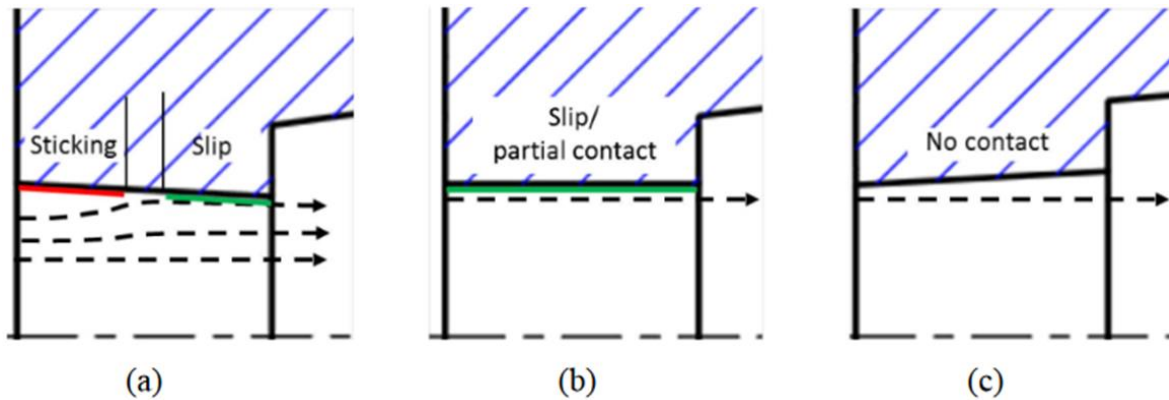


Figure 4-16 Three types of die geometries and their contact condition with the billet: (a) choked die bearing, (b) flat die bearing, (c) relief bearing [96].

#### 4.4.1.5.1 Friction coefficient of the flat die

Referring to the literature [96], to determine the proper friction coefficient at the die bearing region for the flat die, it started from the 25 mm flat die, and two friction coefficients were chosen that are 0.7 and 0.3. Subsequently, two separate simulations were conducted, maintaining all other conditions, such as extrusion speed, billet temperature and tool temperature, consistent with the original extrusion trial. The predicted loads and temperatures, extracted from DEFORM<sup>TM</sup>, were then compared to the measured data, as shown in Figure 4-16.

When the friction coefficient was set to 0.7, both the predicted load and temperature exceeded the measured values, with percentage differences of approximately 10% and 4%, respectively, at a stroke of 150 mm. Conversely, when the friction coefficient was reduced to 0.3, the percentage differences between the predicted load and temperature and the measured data were

both less than 2% at the same stroke. Consequently, a friction coefficient of 0.3 was selected for all flat dies.

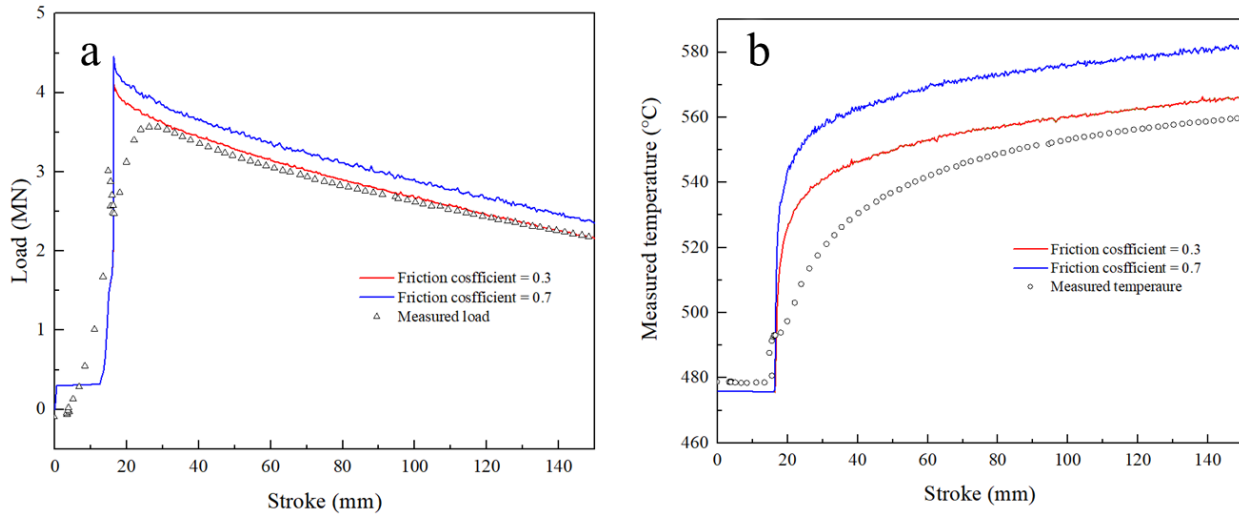


Figure 4-17 Comparisons of the measured loads (a) and temperatures (b) to the measured load and temperature at an extrusion speed of 26 mm/s for the 25 mm flat die respectively (Extrusion ratio = 17:1 and A612 material).

#### 4.4.1.5.2 Friction coefficient of the choked die

For the choked die, the contact condition at the die bearing is more complex compared to that for the flat die bearing. In the literature the researchers either observed it was a combination condition of sticking-slipping or simply slipping with a certain friction coefficient at the die bearing [87,96,97]. In this research, as it is not feasible to physically cut the die in order to observe the die bearing surface, our approach to address this challenge is to determine an average friction coefficient that best replicates the real-world conditions. This will be achieved by comparing the predicted loads and temperatures to their corresponding measured values. Three distinct scenarios were taken into account: a) A uniform friction coefficient of 0.3 along the entire die bearing; b)

The choked section of the die bearing featuring a friction coefficient of 0.5, while the flat section retains a friction coefficient of 0.3; c) The choked portion exhibiting adhesion, while the flat portion maintains a friction coefficient of 0.3, as illustrated in Figure 4-18.

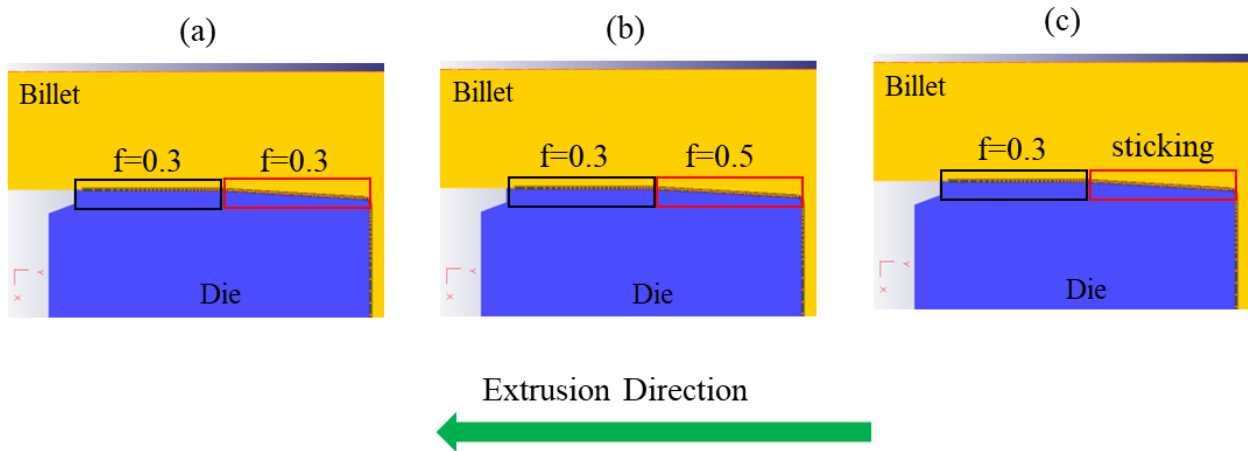


Figure 4-18 Three friction conditions along the die bearing of the 35 mm choked die (Extrusion ratio = 17:1).

Figure 4-19 and Figure 4-20 present a comparison between the measured load history and predicted load histories, as well as the measured temperature history and predicted temperature histories, under varying friction conditions. These experiments were conducted at an extrusion speed of 26 mm/s using a 35 mm choked die.

When the entire bearing employs a friction coefficient of 0.3, both the predicted load and temperature are lower than the measured values. However, when a sticking condition is applied to the choked part of the die, the predicted load and temperature significantly exceed the measured ones. Notably, the predicted data for friction condition (b) closely aligns with the measured data. Consequently, friction condition (b) has been selected for the die bearing region of both the 35 mm choked die and the 12 mm choked die in our simulations.



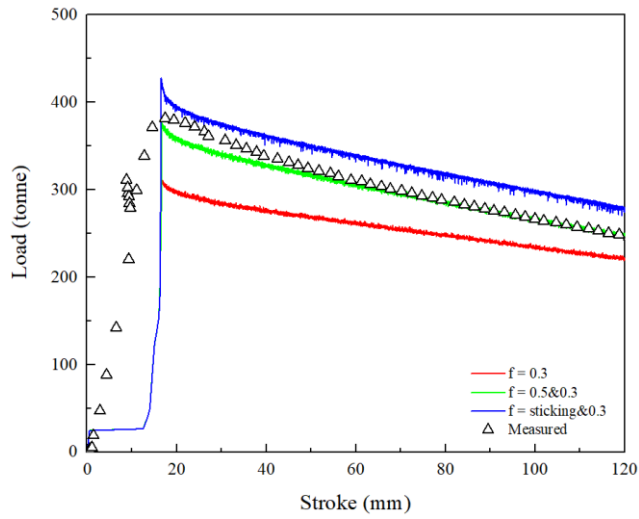


Figure 4-19 Comparison of the measured load history to the model predicted load history using different friction conditions at the extrusion speed of 26 mm/s for the 35 mm choked die.

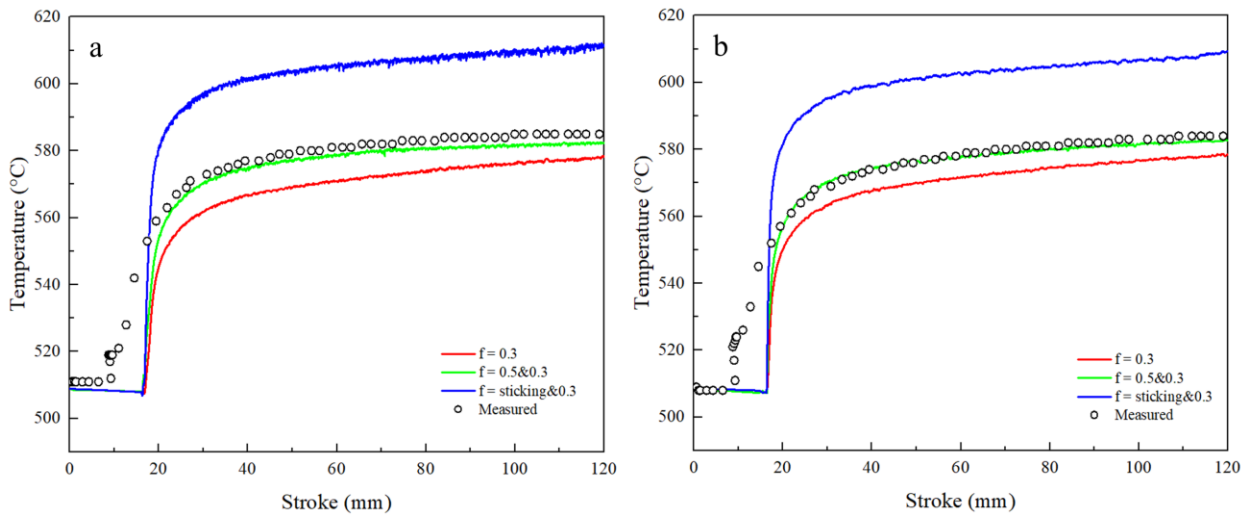


Figure 4-20 Comparison of the measured temperature histories at the (a) TC1 and (b) TC2 to the model predicted temperature histories using different friction conditions at the extrusion speed of 26 mm/s for the 35 mm choked die with material A612 respectively.

#### 4.4.2 Experimental verification of the model

Figure 4-21 presents a detailed comparison between the predicted load and temperature values obtained through numerical simulations with the corresponding measured values obtained at a given extrusion speed when the stroke reaches 150 mm for different die geometries. Figure 4-21 (a) and (b) illustrates the contrast between a representative predicted temperature history and the actual measured temperature history, as well as a representative predicted load history and the actual measured load history for the 25 mm flat die with an extrusion speed of 26 mm/s, respectively. The results show strong agreement between the measured and the predicted curves. Figure 4-21 (c) shows the calculated error between predicted temperatures and loads compared to the corresponding measured values for all dies at the stroke of 100 mm. The figure showcases two to three extrusion speeds for each die, with the error for both the temperatures and loads being measured within 8%. The results clearly show that the model's predicted data exhibits excellent agreement with the measured data, providing a reliable basis for further analysis and interpretation of the extrusion process under different conditions and die geometries.

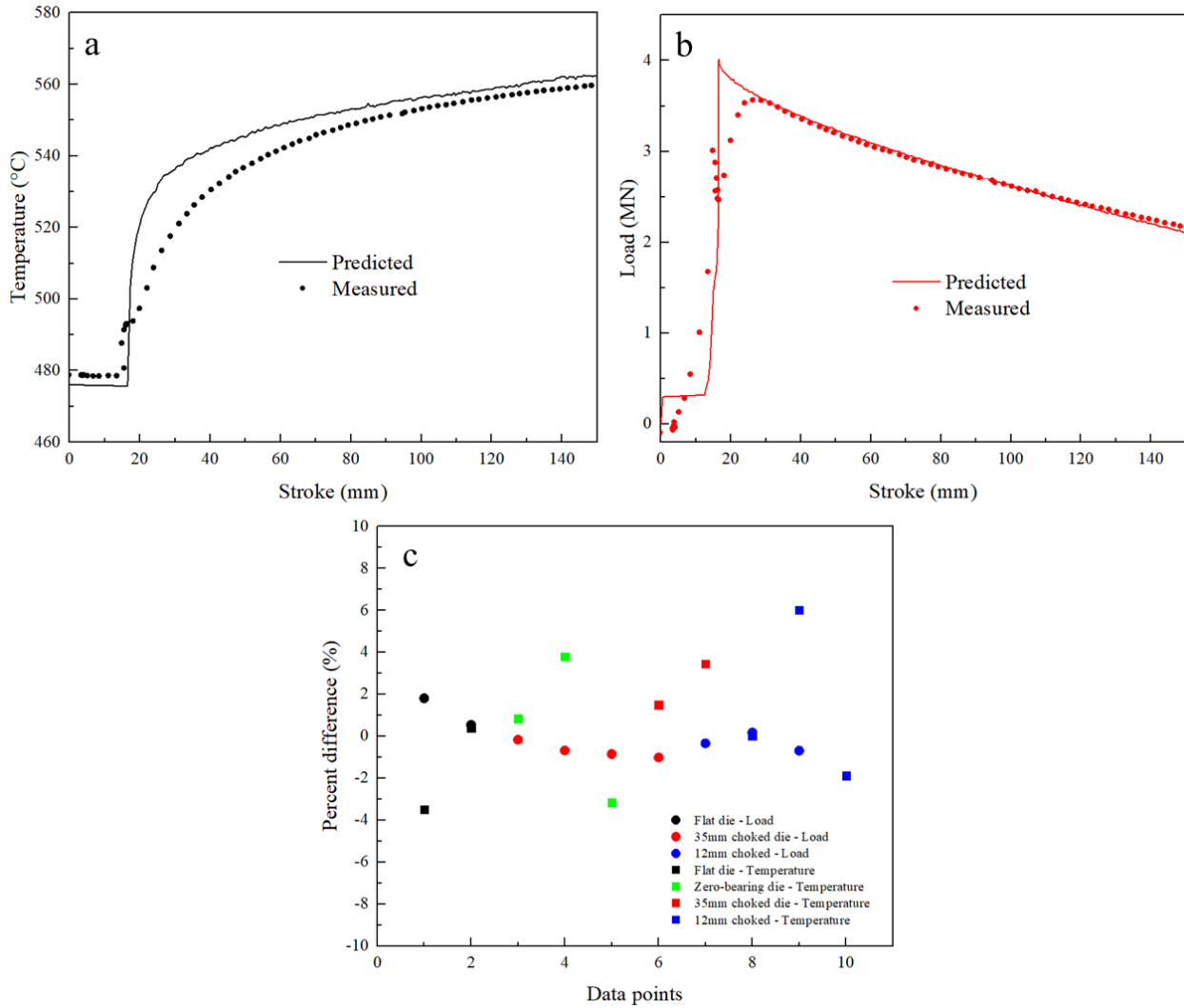


Figure 4-21 Model verification for different die geometries at varying extrusion speeds by comparing the measured load and temperature to the predicted load: (a) and (b) show the comparisons of a typical predicted and measured temperature history and a typical predicted and measured load history, respectively, for the 25 mm flat die with an extrusion speed of 26 mm/s, and (c) presents the calculated error between the predicted temperatures and loads and the corresponding measured values for all dies at a stroke of 150 mm. The data incorporated 2-3 different extrusion speeds.

## **Chapter 5 Results and Discussion**

This chapter presents the findings from the experimental trials and model predictions conducted using various die geometries, Cu levels, and different extrusion speeds. The work focuses on evaluating their impact on surface cracking, surface temperature, and loads. Initially, this chapter begins by presenting the experimental results, specifically highlighting the influence of Cu levels on both solidus behavior and hot compression characteristics.

### **5.1 Material properties**

#### **5.1.1 DSC**

##### **5.1.1.1 DSC results**

Figure 5-1 to Figure 5-4 displays the DSC traces of A576, A611, A612 and A613 under the conditions of as cast and homogenization respectively. The positions of the samples do not affect the overall trend of the measurement much, which implies there is no significant macro segregation along the radius of the billet. The curves of the as-cast and homogenized samples show similar trends with a large melting peak appearing at approximately 650°C, at which the bulk material melts.

After homogenization some additional peaks emerge on the DSC trace between 200°C and 300°C, prompting further investigation using C80 calorimetry for precise analysis. Here only A612 is further analyzed. To achieve this, the samples were cut, ground, and cleaned so that the sample could fit in and contact with the bottom of the crucible properly during testing. Pure aluminum was used as the reference, having the same weight as the sample. The sample was heated up at the rate of 1°C/min from room temperature to 300°C. The DSC curve obtained from this analysis is

shown in Figure 5-5. From the curve, three main exothermic reactions are identified and labeled as I, II and III. Reaction I occurs at around 125°C and is attributed to the formation of the early stage of Si/Mg clusters and nucleation of Guinier-Preston (G.P.) zones. Reaction II and III occur at about 210°C and 250°C respectively, indicating the precipitation of  $\beta''$  and/or  $\beta'$ , Q' or some other metastable phases. The result is in good agreement with the measurement by Bryant for AA6111 [98].

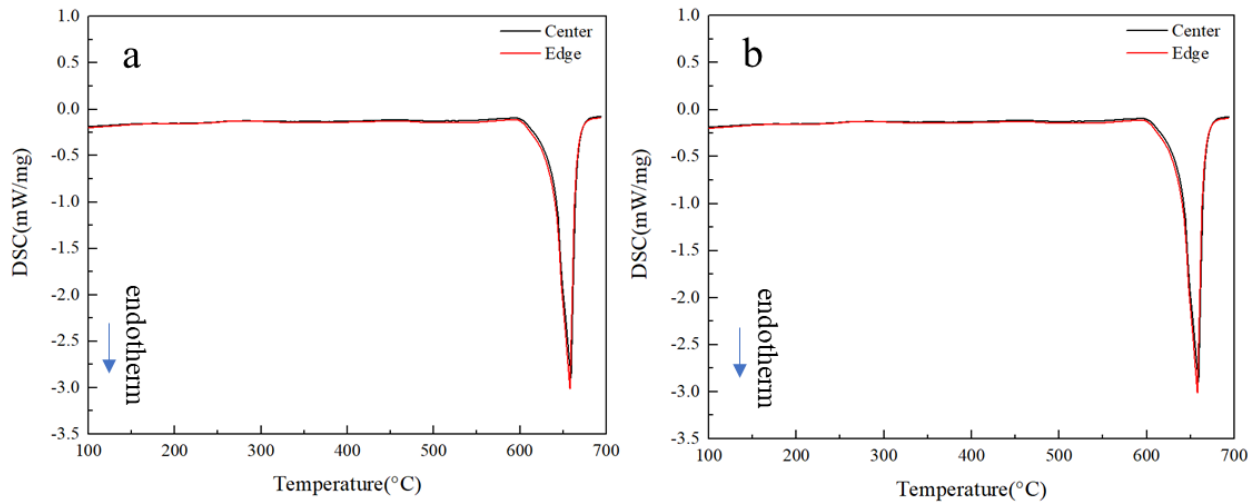


Figure 5-1 DSC traces of the as-cast A576 material and the homogenized A576 material.

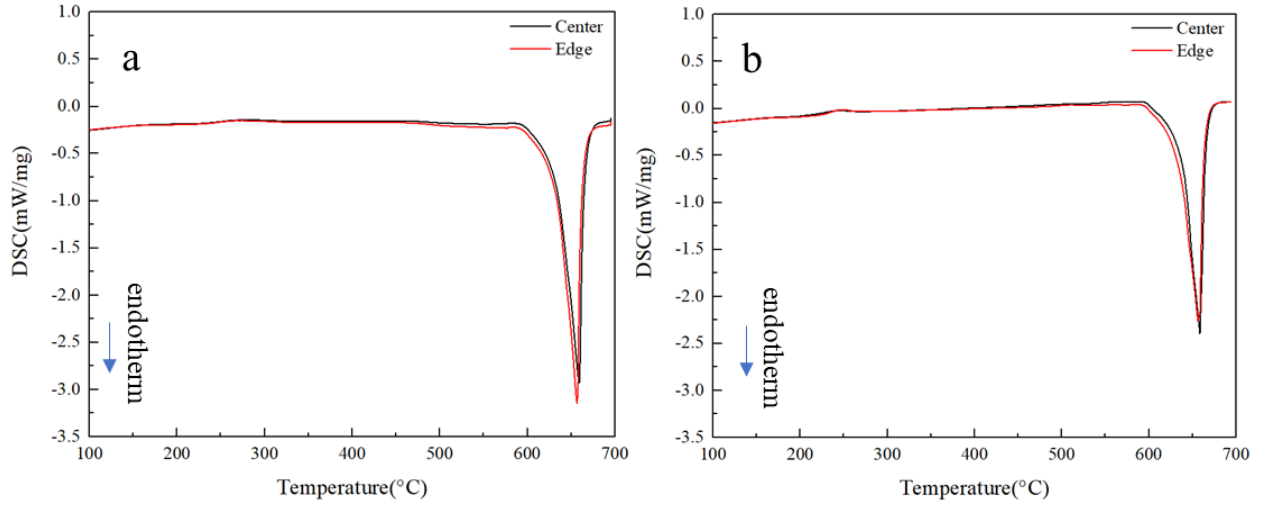


Figure 5-2 DSC traces of the as-cast A611 material and the homogenized A611 material.

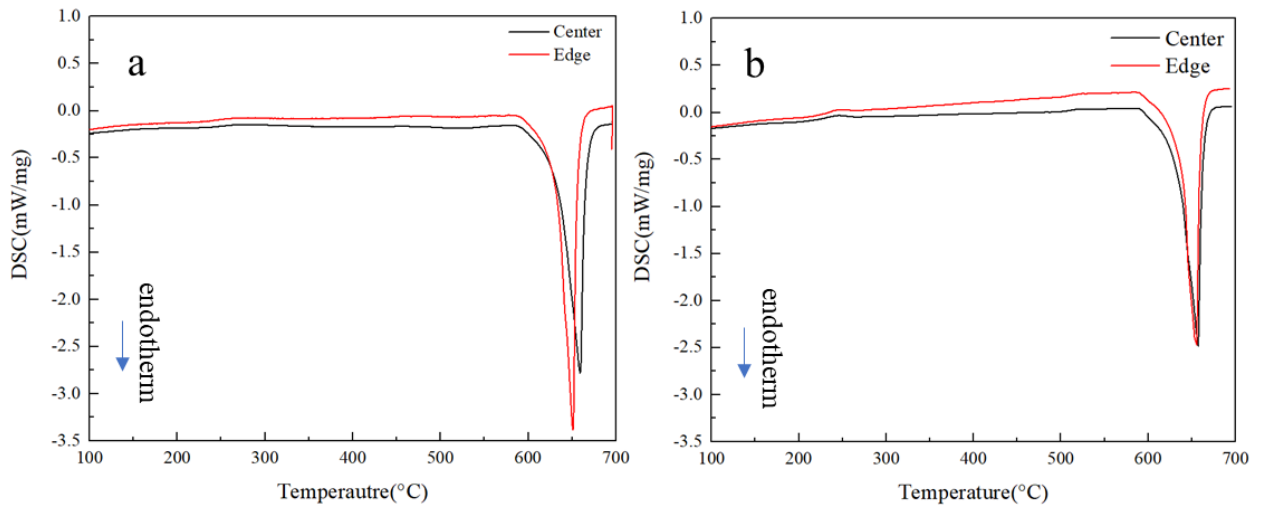


Figure 5-3 DSC traces of (a) as-cast A612 material and (b) the homogenized A612 material.

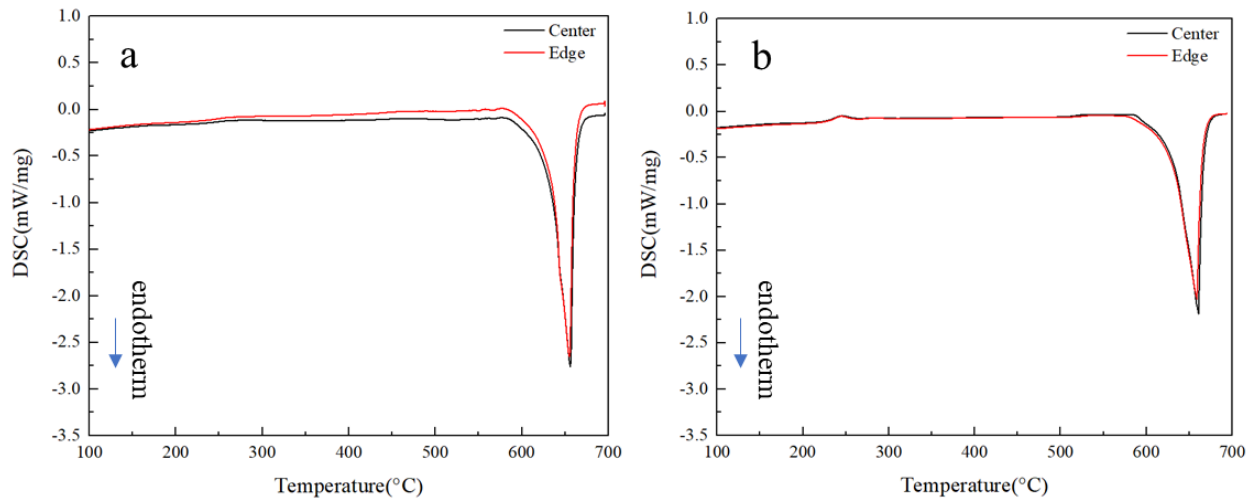


Figure 5-4 DSC traces of (a) as-cast A613 material and (b) the homogenized A613 material.

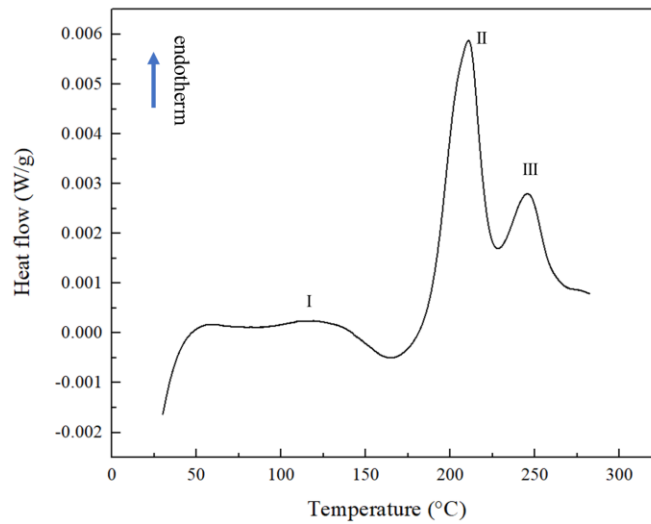


Figure 5-5 Measured DSC curve of homogenized A612 obtained from the C80 calorimeter.

### 5.1.1.2 Determination of the solidus temperature

Usually, the classical onset temperature of the melting peak on the DSC curve is regarded as the melting temperature of the pure material because it is less dependent on the heating rate and the sample mass, as shown in Figure 5-6 (b). The classical onset temperature is the temperature at

which the base line and the tangent of the peak front intersect. However, for alloys with a broad melting interval, there might be some incipient melting at the onset temperature, which is adverse to extrusion defects [30]. To account for this, the user-defined method to determine the solidus temperature of the alloys was applied in this work [99]. The temperature at which the peak front on the DSC curve deviates from the base line is taken as the solidus temperature for the extrusion material. The baseline is part of the DSC curve and shows no phase transformation. Using this method, the solidus temperatures of the alloys depend on the view scale. For all the curves a temperature range of 550-700°C and a DSC range of -0.5 to 0.5W/g are defined for this research. Taking A612 as an example, the solidus temperature of the material was found to be approximately 590°C, as shown in Figure 5-6 (b).

Using this technique, the solidus temperatures of the as cast and homogenized material are summarized in Table 5-1 and the effect of Cu contents on this is shown in Figure 5-7. As the Cu content increases from 0 to 0.9, the average solidus temperatures of the as cast materials decrease from 597.9°C to 581.3°C, and the average solidus temperatures of the homogenized materials decrease from 601.7°C to 583.3°C. Generally, the solidus temperatures of the homogenized materials are higher compared with that of the as-cast material. This is because during the homogenization process dissolution happens to most of the second phases, which makes the start of the melting peak begins at a higher temperature [100]. The solidus temperature is also compared with the thermo-calc simulation results of the homogenized material calculated by co-workers at University of British Columbia and the simulation results show the same trends and are lower than both the as cast and homogenized experimental results.



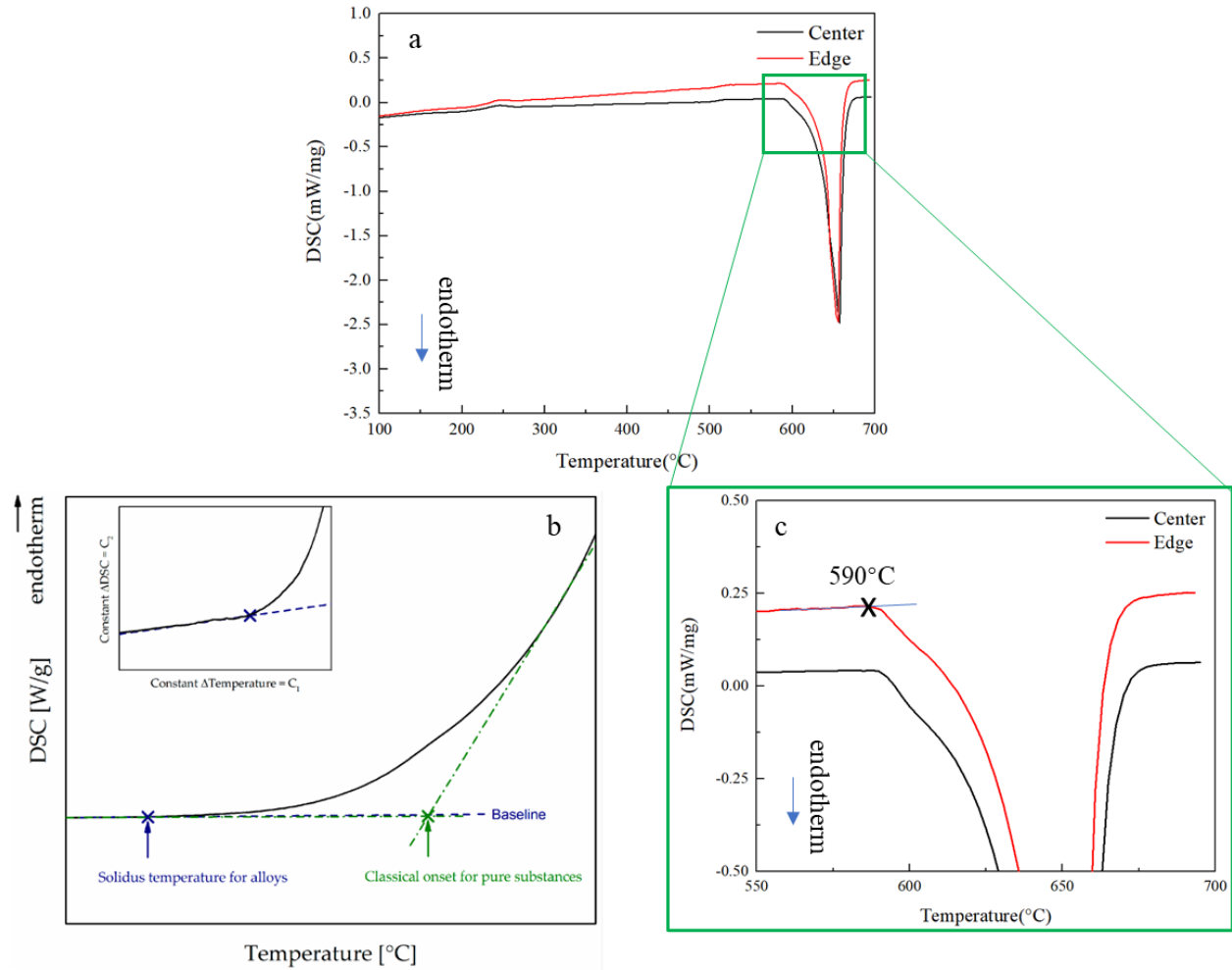


Figure 5-6 DSC results and determination of the solidus temperature of the homogenized material: (a) shows the DSC traces of both samples from the edge and center of the billet going from room temperature to melting; (b-c) shows how the solidus temperature is determined for the material [99].

Table 5-1 Estimated solidus temperature of each material based on DSC tests (°C).

As-cast	Edge	Center	Avg.	Homo.	Edge	Center	Avg.
A576	597.9	597.9	597.9	A576	600.9	602.4	601.7
A611	591.2	592.3	591.8	A611	592.6	594.2	593.4
A612	589.0	588.9	589.0	A612	590.5	589.4	590.0
A613	581.2	581.4	581.3	A613	583.3	583.3	583.3

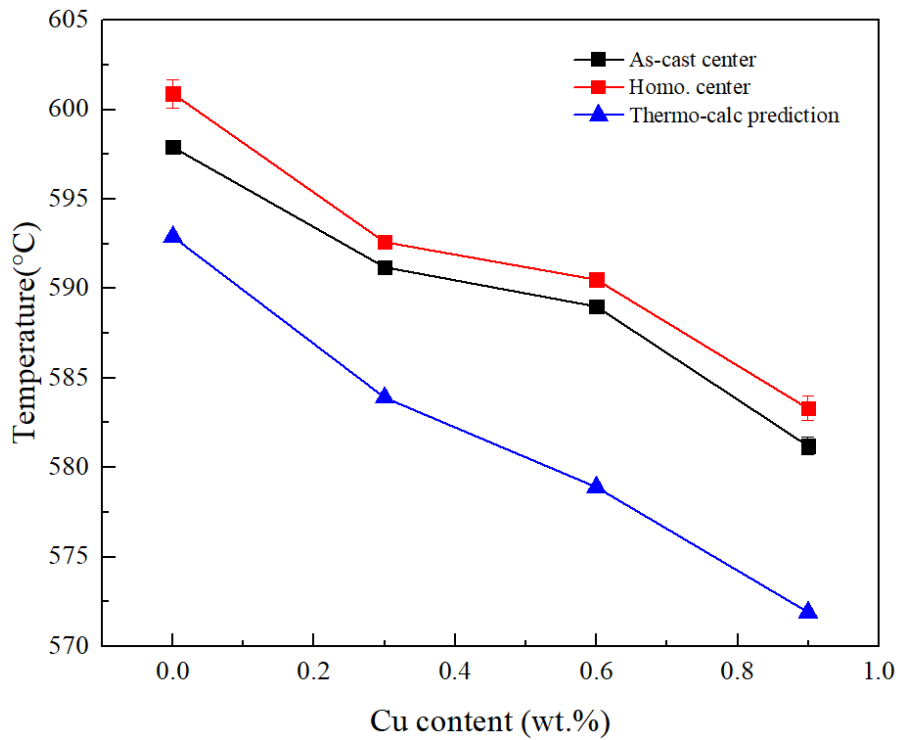


Figure 5-7 Comparison of the estimated solidus temperature as a function of Cu content for as-cast and homogenized A576, A611, A612 and A613 from center of the billet and model-predictions using thermo-calc.

## 5.1.2 Hot deformation behavior

### 5.1.2.1 Hot compression test

Compression tests were done on Gleeble<sup>TM</sup> 3500 and cam plastometer. For the tests on Gleeble<sup>TM</sup> 3500 the test temperatures are 450°C, 500°C and 550°C and the test strain rates are 0.1/s, 1/s, and 10/s. Three tests were repeated for each condition. Some high strain rate tests were done on Cam plastometer considering that the material in the extrusion process goes through high deformation, and the accuracy of the constitutive model could be improved by including some high strain rate flow stress data. The test temperature is 550°C and the test strain rates are 50/s and 100/s on the cam plastometer. Three tests were also repeated for each condition for the tests on the cam plastometer.

Figure 5-8, Figure 5-9 and Figure 5-10 shows the true stress-true strain curves of the three materials at the deformation temperature of 450°C, 500°C, and 550°C and at the strain rates of 0.1/s (black), 1/s (red), and 10/s (blue). Figure 5-11 presents the true stress-true strain curves of the three materials on Cam plastometer at the deformation temperature of 550°C and the strain rates of 50/s (black) and 100/s (red). The solid curve, dash curve, and dot curve curves represent the A611, A612, and A613, respectively in all the true stress-true strain curves.

Notably the flow stress for all the material exhibits a rapid increase to a peak stress level due to work hardening. Subsequently stress decreases at a relatively slow rate or stays steady due to dynamic softening. It is noteworthy that aluminum alloys, characterized by their high stacking-fault energy, tend to experience substantial dynamic softening during hot deformation [101].

For specific material, as the temperature decreases and the strain rate increases, the flow stress tends to rise. Furthermore, dynamic softening, which occurs after reaching the peak stress,

tends to manifest at lower strain rates. This is because lower strain rates provide an extended period for dynamic softening to take place. Conversely, at higher strain rates, the flow stress tends to stabilize as the rate of work hardening due to deformation is balanced against the rate of recovery.

When comparing the flow stress of the three materials under similar deformation conditions, their differences appear relatively minor. Table 5-2 summarized the average flow stress data from the true strain of 0.1 to 0.4 for A611, A612, and A613 at varying deformation temperatures and strain rates. Taking the flow stress data at 500°C as an example, at strain rates of 0.1/s, 1/s, and 10/s, the variations in average flow stress between true strains of 0.1 to 0.4 between A611 and A612, as well as A612 and A613, are less than 6%. So in this study, a constitutive model specifically for A612 was developed and utilized to represent all three materials.

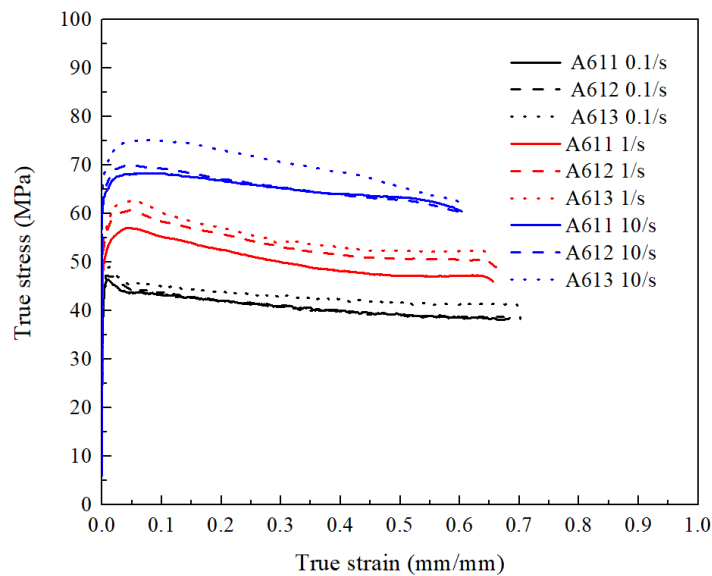


Figure 5-8 Measured flow stress at the deformation temperature of 450°C for three materials with varying Cu contents (solid line: A611, dash line: A612, dot line: A613) at different strain rates (0.1/s-black, 1/s-red, and 10/s-blue) on Gleeble™ 3500.

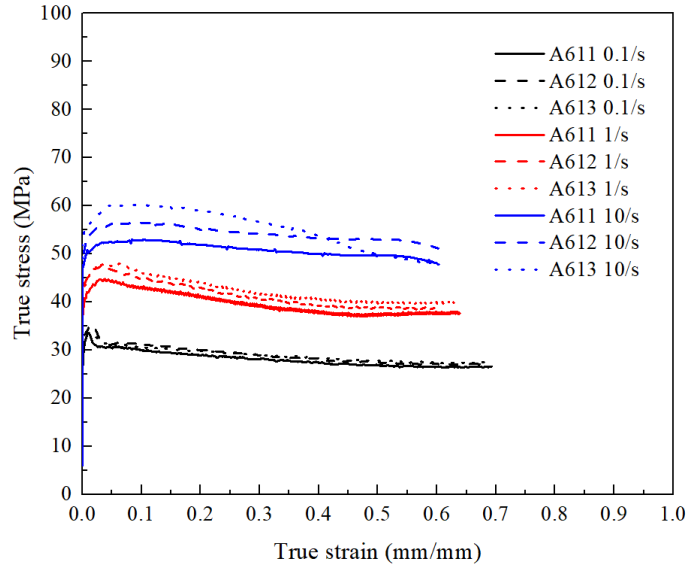


Figure 5-9 Measured flow stress at the deformation temperature of 500°C for three materials with varying Cu contents (solid line: A611, dash line: A612, dot line: A613) at different strain rates (0.1/s-black, 1/s-red, and 10/s-blue) on Gleeble™ 3500.

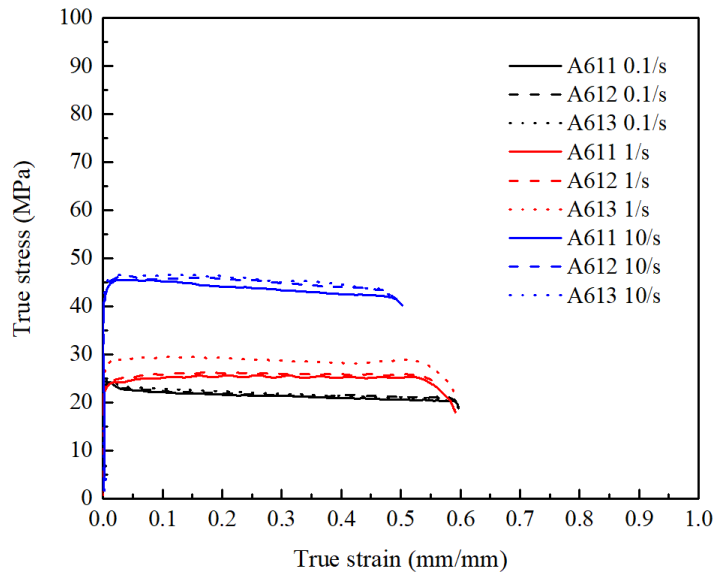


Figure 5-10 Measured flow stress at the deformation temperature of 550°C for three materials with varying Cu contents (solid line: A611, dash line: A612, dot line: A613) at different strain rates (0.1/s-black, 1/s-red, and 10/s-blue) on Gleeble™ 3500.

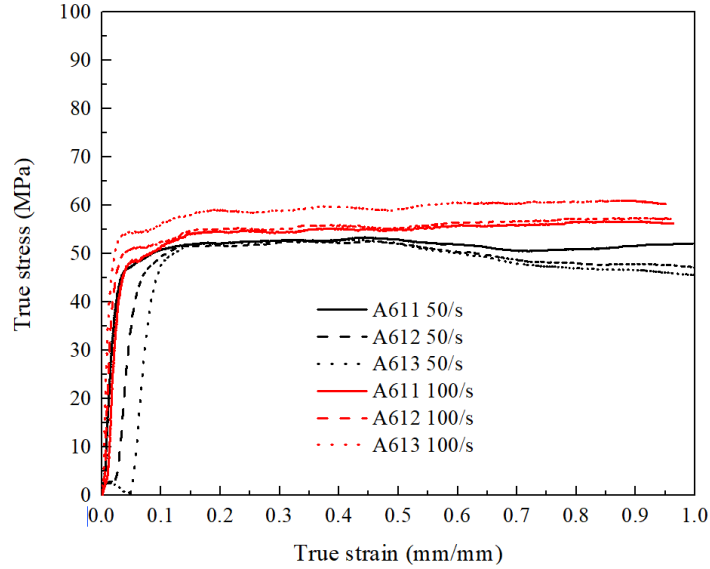


Figure 5-11 Measured flow stress at the deformation temperature of 550°C for three materials with varying Cu contents (solid line: A611, dash line: A612, dot line: A613) at different strain rates of 50/s (black) and 100/s (red,) on cam plastometer.

Table 5-2 Average flow stress data calculated between the true strain of 0.1 to 0.4 for A611, A612, and A613 at different deformation temperatures and different strain rates (MPa).

	450°C			500°C			550°C				
	0.1/s	1/s	10/s	0.1/s	1/s	10/s	0.1/s	1/s	10/s	50/s	100/s
A611	41.4	50.9	66.1	28.5	39.9	51.4	21.5	25.4	43.8	52.3	54.3
A612	41.6	54.2	66.4	39.5	41.6	54.8	21.7	26.0	45.2	51.8	54.9
A613	43.5	55.7	71.8	29.4	42.6	57.4	22.1	29.0	45.8	52.0	58.6

### 5.1.2.2 Constitutive model

The Sellars-Tegart constitutive model is commonly used to describe the relationship among the flow stress ( $\sigma$ ), strain rate ( $\dot{\epsilon}$ ) and temperature (T). The equation is described as

$$\sigma = \frac{1}{\alpha} \ln \left[ \left( \frac{Z}{A} \right)^{\frac{1}{n}} + \left( \left( \frac{Z}{A} \right)^{\frac{2}{n}} + 1 \right)^{\frac{1}{2}} \right] \quad 5-1$$

$$Z = \dot{\epsilon} \exp \left( \frac{Q}{RT} \right) \quad 5-2$$

Where  $\dot{\epsilon}$  is the strain rate of deformation, A, n and  $\alpha$  are material constants, Q is the deformation activation energy (kJ/mol), R is the gas constant (8.318 J/mol/K), T is the absolute deformation temperature (K). The parameters needed for the Sellars-Tegart constitutive model were fitted using the average flow stress listed in Table 5-2.

To determine  $\alpha$ , another set of equations are needed as

$$\dot{\epsilon} = Af(\sigma) \exp \left( \frac{-Q}{RT} \right) \quad 5-3$$

$$f(\sigma) = \begin{cases} \sigma^{n1} (\alpha\sigma < 0.8) \\ \exp(\beta\sigma) (\alpha\sigma > 1.2) \\ [\sinh(\alpha\sigma)]^n (\text{for all } \alpha\sigma) \end{cases} \quad 5-4$$

$$\alpha = \beta/n1 \quad 5-5$$

Where  $\beta$  and n1 are all material constants. Substituting Equation 5-4 to Equation 5-3, and then take natural logarithm on both sides of the equations, the following equations can be obtained.

$$\ln \dot{\epsilon} = \ln A + n1 \ln \sigma - \frac{Q}{RT} \quad 5-6$$

$$\ln \dot{\epsilon} = \ln A + \beta\sigma - \frac{Q}{RT} \quad 5-7$$

$$\ln \dot{\epsilon} = n \ln [\sinh(\alpha\sigma)] - \frac{Q}{RT} \quad 5-8$$

Then n1,  $\beta$ , n can be obtained by the following equations.

$$n1 = \left( \frac{\partial \ln \dot{\epsilon}}{\partial \ln \sigma} \right)_T \quad 5-9$$

$$\beta = \left(\frac{\partial \ln \dot{\epsilon}}{\partial \sigma}\right)_T \quad 5-10$$

$$n = \left(\frac{\partial \ln \dot{\epsilon}}{\partial \ln[\sinh(\alpha\sigma)]}\right)_T \quad 5-11$$

Through Eq. 5-9, Eq. 5-10, and Eq.5-11, whose figures are shown in Figure 5-12 (a), (b), and (c), respectively, the values of  $n$ ,  $\beta$  and  $n$  can be obtained by taking the average slope values in the corresponding figure. To calculate  $Q$ , first transforming Equation 5-8 into

$$Q = nR \left(\frac{\partial \ln[\sinh(\alpha\sigma)]}{\partial (1/T)}\right)_{\dot{\epsilon}} \quad 5-12$$

Then  $Q$  can be obtained by taking the average slope values in Figure 5-12 (d). Then take natural logarithm on both sides of 5-3

$$\ln[\sinh(\alpha\sigma)] = \frac{\ln \dot{\epsilon}}{n} + \frac{Q}{RTn} - \frac{\ln A}{n} \quad 5-13$$

By plotting  $\ln[\sinh(\alpha\sigma)]$  vs.  $\ln \dot{\epsilon}$  and fitting linearly, the interception of the lines (I) can be calculated. Then  $A$  is calculated by the following equation

$$A = \exp\left(\frac{Q}{RT} - nI\right) \quad 5-14$$

The calculated values of the constitutive model parameters are listed in Table 5-3.



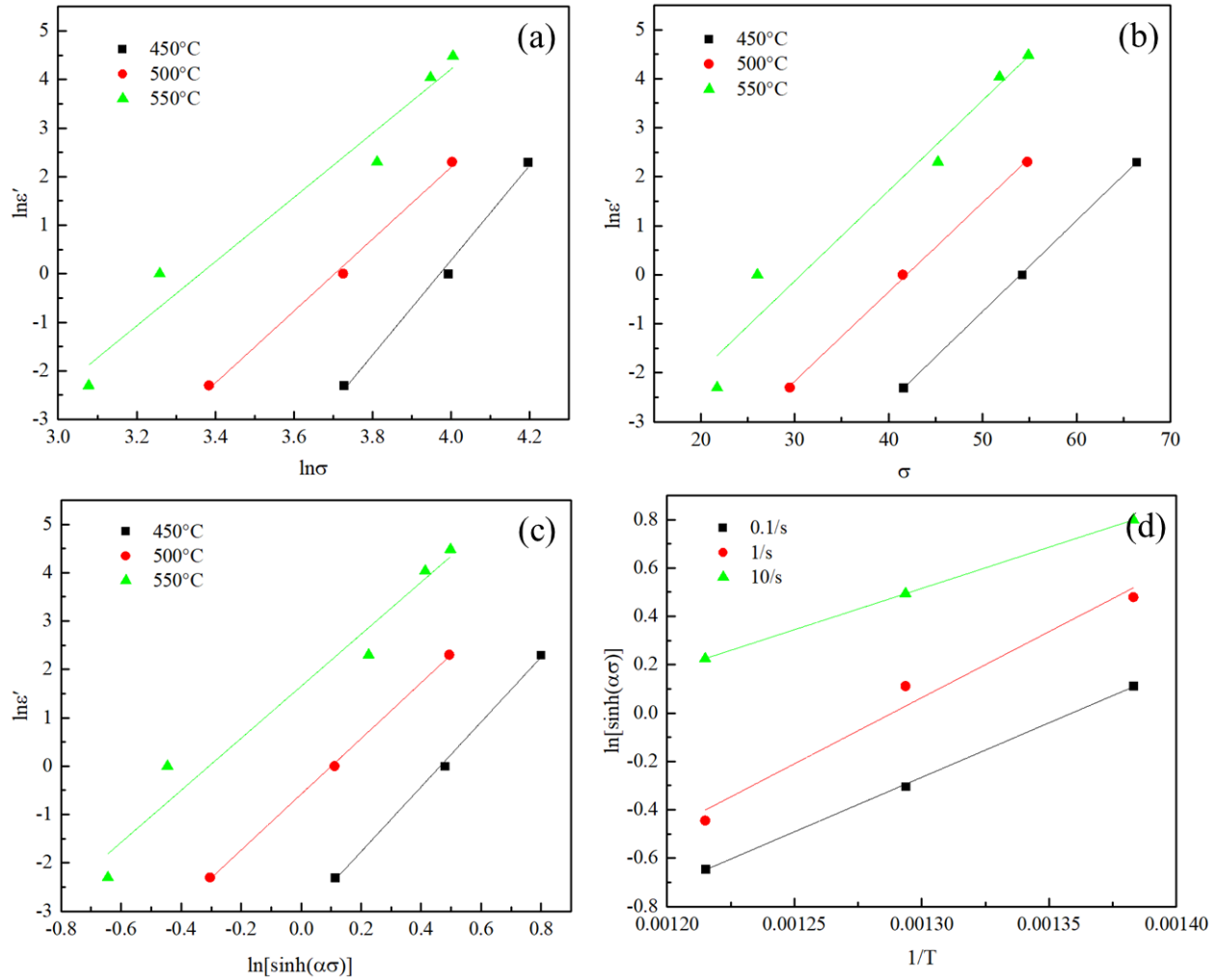


Figure 5-12 Relationship of (a)  $\ln \epsilon'$  vs.  $\ln \sigma$ ; (b)  $\ln \epsilon'$  vs.  $\sigma$ ;  $\ln \epsilon'$  vs.  $\ln[\sinh(\alpha\sigma)]$ ; (d)  $\ln[\sinh(\alpha\sigma)]$  vs.  $1/T$ .

The model predicted values of the flow stress are compared with the measured data of all three alloys, which is shown in Figure 5-13. The differences between the model predicted flow stress and the measured flow stress for all three materials all fall into the  $\pm 10\%$  range. So, this model was used to represent three materials with different Cu additions in the modeling work.

Table 5-3 Constitutive model parameters of A612.

Material model parameter	Value
A	$1.23 \times 10^{15}/s$
$\alpha$	0.023/MPa
n	5.99
Q	225kJ/mol/K
R	8.314J/mol/K

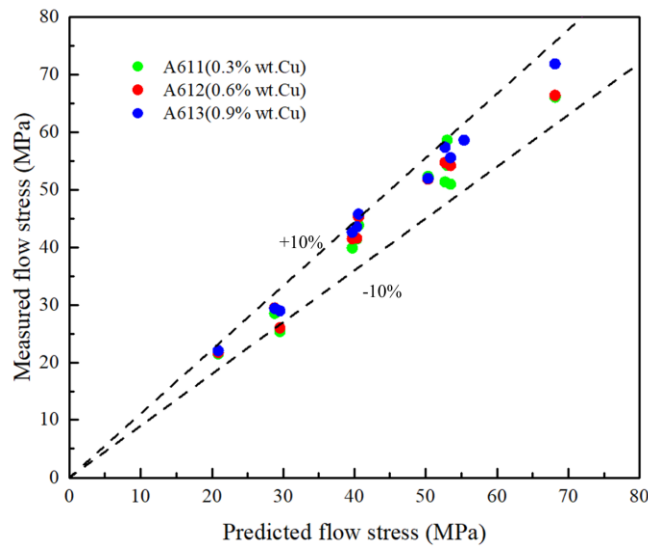


Figure 5-13 Comparison of model predicted flow stress and measured flow stress for A611, A612, and A613. The dotted lines represent +/- 10% of the measured data.

## 5.2 Extrusion trials

### 5.2.1 Measured load and temperature

The load histories of the extrusion trials were obtained from the extrusion press and the temperature histories of the extrusion trials were measured by the thermocouples located in the die bearing. The locations of the thermocouples can be found in Section 4.3.

Figure 5-14 shows the typical temperature and load histories of the extrusion trials at different extrusion speeds for the 12 mm flat die using the A612 material with an extrusion ratio of 70:1 in extrusion trial #1. The left figure shows the measured temperature histories at the extrusion speeds of 4 mm/s, 5 mm/s, and 6 mm/s. Referring to Figure 5-14 (a), the temperature rises rapidly to 570°C at a stroke of ~25 mm. As the stroke continues to increase the temperature rise is relatively small and approached a steady state value of ~570°C for all speeds. The measured temperatures increase as the extrusion speed increases because more heat is generated due to the faster deformation of the material at a higher extrusion speed. The corresponding measured loads are shown in the right figure. Referring to Figure 5-14 (b), the load increases fast to the peak load at the stroke of around 20 mm, during which the billet is filling the container, and then the load reaches the maximum value when the material breaks out of the die. After reaching the peak value, the load decreases smoothly until the end of the extrusion due to the contacting area reduction between the billet and the container and reduced friction force. As speed increases there is an expected increase in both the breakthrough load and subsequent loads because the material goes through a higher strain rate as the extrusion speed increases.

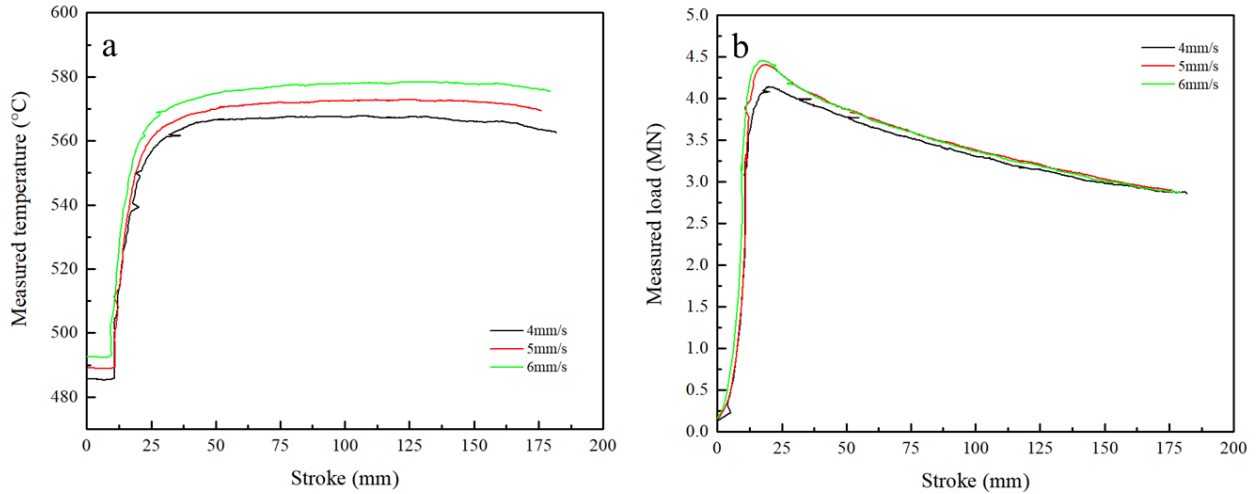


Figure 5-14 Typical measured temperature (a) and load (b) histories of the extrusion trials at different extrusion speeds for A612 material and with an extrusion ratio of 70:1 in extrusion trial #1.

## 5.2.2 Extrudate characterization

All the as-extruded surfaces were characterized by both visual observation and micro-observation. Micro observation was performed by scanning electron microscopy (SEM) for high magnification images of the as-extruded surfaces. This was done at the Zeiss UltraPlus FESEM. The peripheral coarse grain (PCG) layers in the cross-section area along the extrusion direction were observed by using the microscope with polarized light. In addition, the Keyence VK-X250K laser scanning microscope was used for 2D and 3D surface profilometry to measure the surface roughness of the extrudates produced by different die geometries with the extrusion ratio of 17:1 and by different materials A612 and A613 with the 25 mm flat and 35 mm choked dies. The samples were prepared from either the front, middle, or back sections of the extrusion profile, as shown in Figure 5-15.

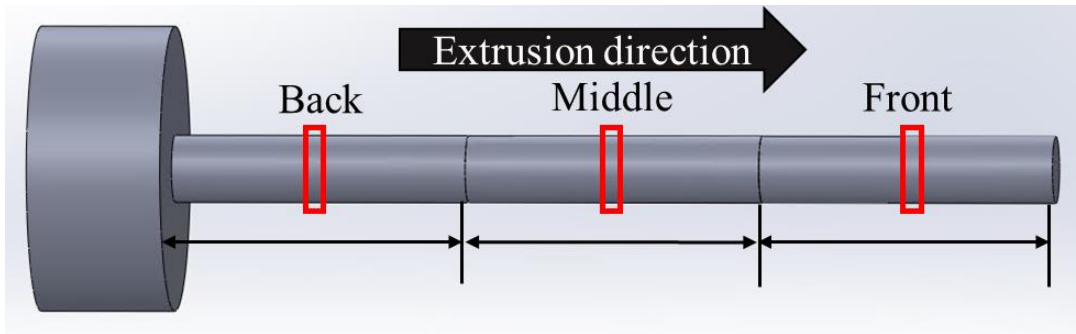


Figure 5-15 Schematic sample locations from the extrudate for analysis.

Figure 5-16 presents the visual observations of the extrudate surfaces for A612 using a 12 mm flat die with an extrusion ratio of 70:1. In Figure 5-16 (a), we examined the surface images of the extrudates with samples from the back of the extrusion at varying extrusion speeds, ranging from 4 mm/s to 10 mm/s. Notably, the extrusion speed has a significant influence on the surface morphology, particularly regarding the formation of cracks. Evidently, when the extrusion speed is set at 4 mm/s, 6 mm/s, and 8 mm/s, no surface cracks are observable. However, at extrusion speeds of 9 mm/s and 10 mm/s, surface cracks begin to manifest. Comparing these two speeds, it becomes apparent that at 10 mm/s, the cracks are more pronounced and larger in size.

In Figure 5-16 (b) and (c), we observe the evolution of the extrudate surface throughout the extrusion process, specifically at extrusion speeds of 9 mm/s and 10 mm/s, respectively. At the extrusion speed of 9 mm/s, there are no apparent cracks on the surface at the beginning of the extrusion, but as the process progresses, surface cracks become evident, particularly on the back of the extrudate. Conversely, at the extrusion speed of 10 mm/s, visible surface cracks are observable nearly throughout the entire extrusion. The final five bars of the image exhibit substantial and densely distributed cracks on the extrudate surface. This surface crack formation

at higher extrusion speeds can be attributed to the accelerated temperature increase within the die bearing and the elevated strain rate when using a higher extrusion speed.

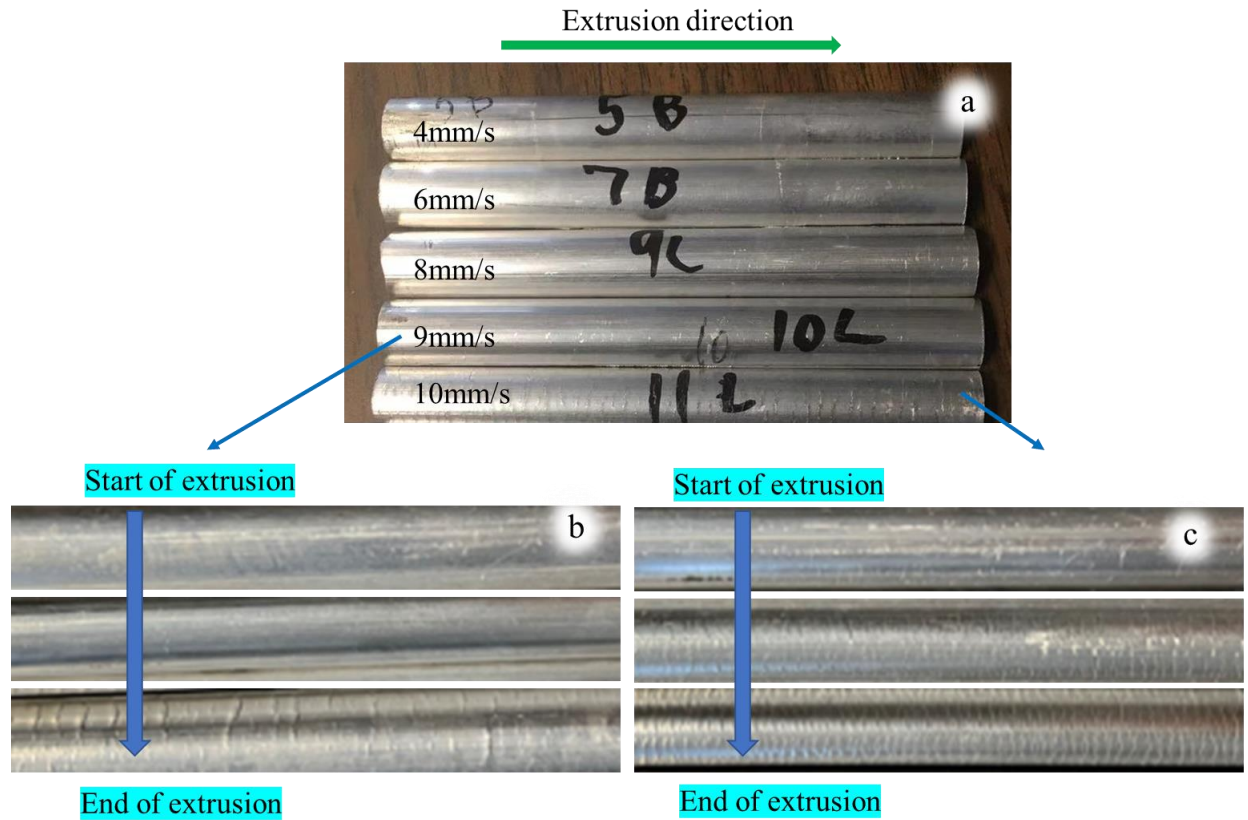


Figure 5-16 Visual observation of the extrudate surfaces extruded by the 12 mm flat die with an extrusion ratio of 70:1, the material is A612: (a) the as-extruded surface images of the extrudates from the back of the extrusion with the extrusion speed change from 4-10 mm/s; (b) and (c) show how the extrudate surface changes from the beginning to the end of the extrusion process at the extrusion speed of 9 mm/s and 10 mm/s respectively.

Figure 5-17 presents the surface morphology by SEM of the samples from the back of the extrudates produced by a 12 mm flat die using A612 with an extrusion ratio of 70:1 at varying extrusion speeds, with figures (a) to (f) representing the extrusion speeds of 4 mm/s, 6 mm/s, 7 mm/s, 8 mm/s, 9 mm/s, and 10 mm/s respectively. For figure (a) to (c), the extrusion direction is

from the top to the bottom of the figures, and for figure (d) to (f), the extrusion direction is from the left to the right of the figures. The lines along the extrusion direction are die lines. As the extrusion speed increases, certain changes in the extrudate surface become evident. At lower speeds (figure a and b), the extrudate appears smooth and exhibits no surface cracks under SEM. However, as the speed increases (c to f), the surface exhibits progressively larger surface cracks, indicating clear damage to the extrudate surface during the extrusion process. This can be attributed to the faster temperature rise caused by greater work input at higher extrusion speeds. Additionally, higher extrusion speeds subject the material to a higher strain rate, resulting in increased tensile stress experienced by the material [48].

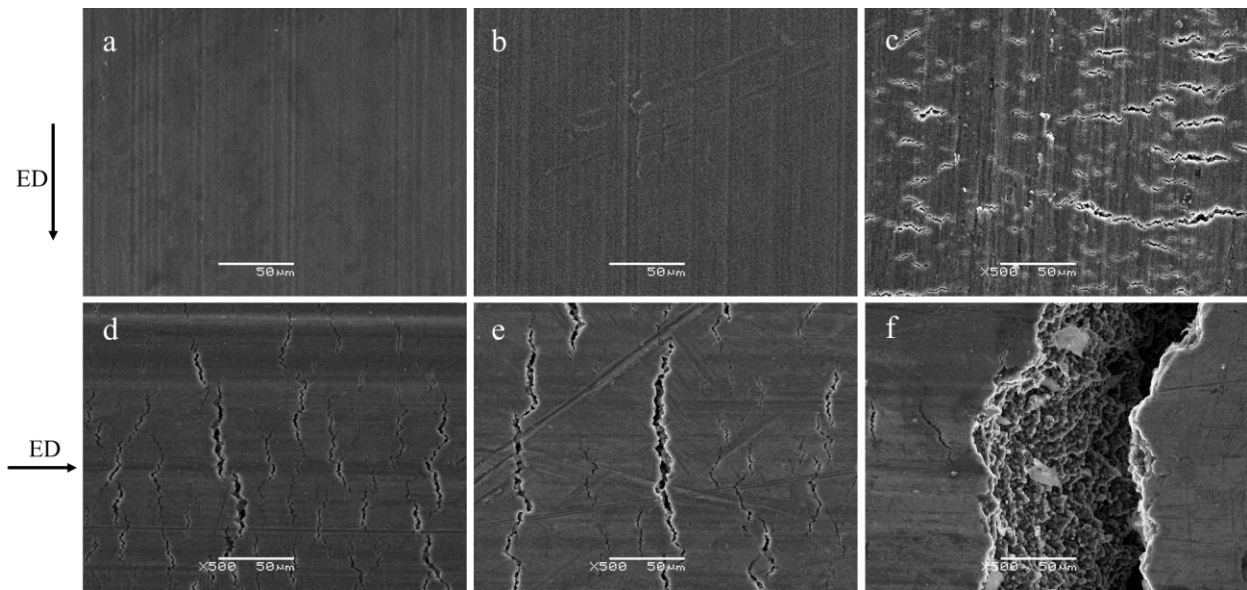


Figure 5-17 Surface morphology of the back of the extrudates produced by a 12 mm flat die with an extrusion ratio of 70:1 using A612 at varying extrusion speed: (a) 4 mm/s, (b) 6 mm/s, (c) 7 mm/s, (d) 8 mm/s, (e) 9 mm/s, and (f) 10 mm/s by SEM. (ED = Extrusion Direction).

The appearance of the Peripheral Coarse Grain (PCG) growth structure poses a significant challenge by introducing microstructure imperfections that notably impact the machinability,

mechanical properties. This phenomenon is predominantly observed in high-strength aluminum alloys and is intricately linked to the nature of the extrusion process, which involves elevated temperatures and significant levels of strain and strain rates. Consequently, this process greatly increases the likelihood of forming a coarse grain structure on the surface of the extruded material [102].

Figure 5-18 illustrates the presence of the Peripheral Coarse Grain (PCG) layer within the cross-sectional area perpendicular to the extrusion direction of the extrudates. These extrudates were produced using a 12 mm flat die with A612 alloy, with extrusion speeds ranging from 4 mm/s to 10 mm/s. This observation was conducted using a microscope equipped with polarized light and performed by a colleague at Rio Tinto.

The thickness of the PCG layer demonstrates an increasing trend as the extrusion speed rises. This phenomenon can be attributed to the concurrent rise in strain rate, accumulated strain, and temperature rise associated with higher extrusion speeds. This outcome is advantageous for promoting grain growth, as discussed in reference [103,104]. However, it is worth noting that the PCG layer thickness at an extrusion speed of 6 mm/s deviates from this pattern. This exception primarily results from elevated temperatures within the die bearing specifically at this speed, as demonstrated in Figure 5-19, even when the extrusion speed remains steady throughout the entire extrusion process.



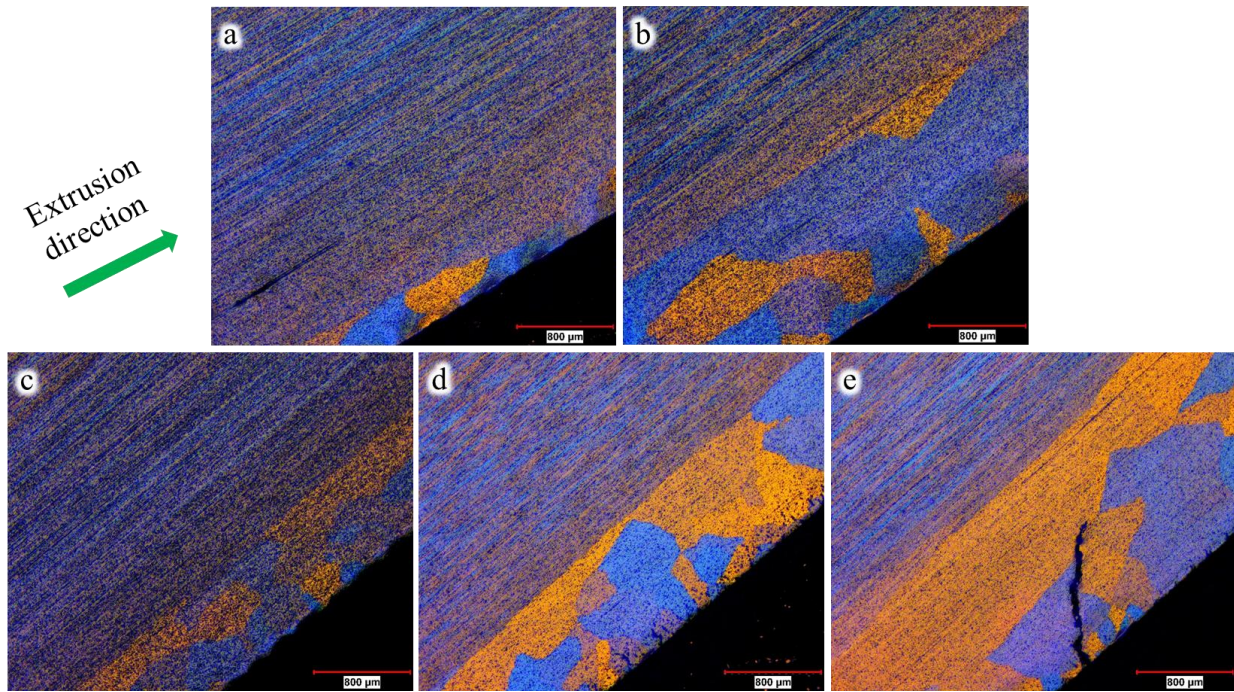


Figure 5-18 PCG layer in the cross-section area along the extrusion direction of the extrudates produced by the 12 mm flat die with A612 at varying extrusion speed: (a) 4 mm/s, (b) 6 mm/s, (c) 8 mm/s, (d) 9 mm/s, (e) 10 mm/s by microscope with polarized light.

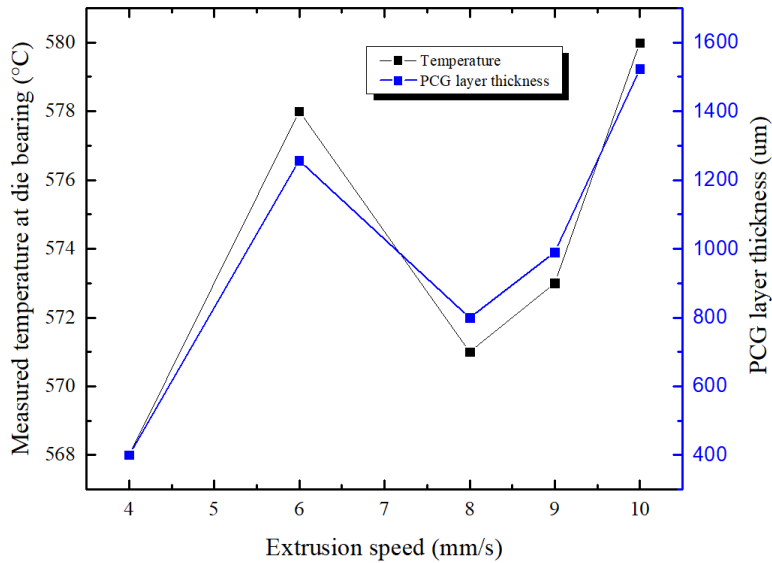


Figure 5-19 Correlation of the measured temperature in the die bearing when the stroke is 150 mm and the PCG layer thickness of the extrudates produced by the 12 mm flat die using A612 at various extrusion speeds using A612.

To examine how the extrusion speed affects the size of the surface cracks, extrudates produced by the 25 mm flat die with the material of A612 at various extrusion speeds were examined. Four of the longest cracks and four of the widest cracks were picked for measurement for each extrusion speed as shown in Figure 5-20. The crack sizes were plotted against the extrusion speeds in Figure 5-21. The length and the width of the surface cracks increase fast as the extrusion speed increases.

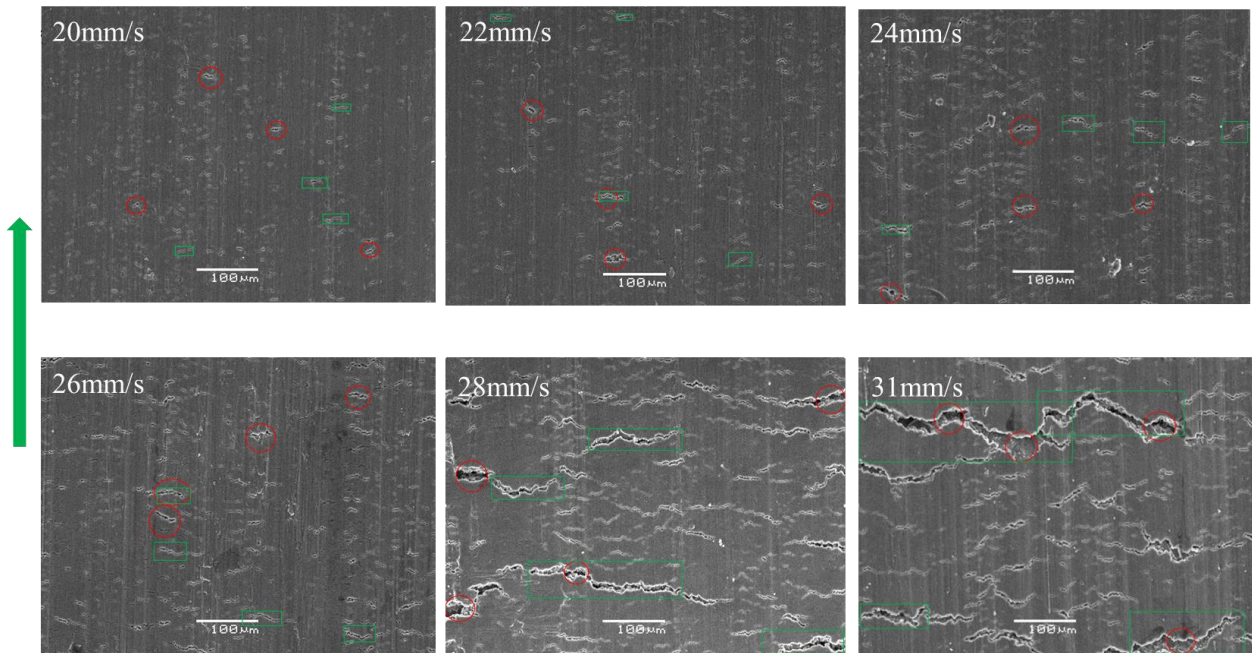


Figure 5-20 Surface cracks picked from the extrudates generated by the 25 mm flat die with the material of A612 and the extrusion speed ranging from 20 mm/s to 31 mm/s for measurement of the crack size.

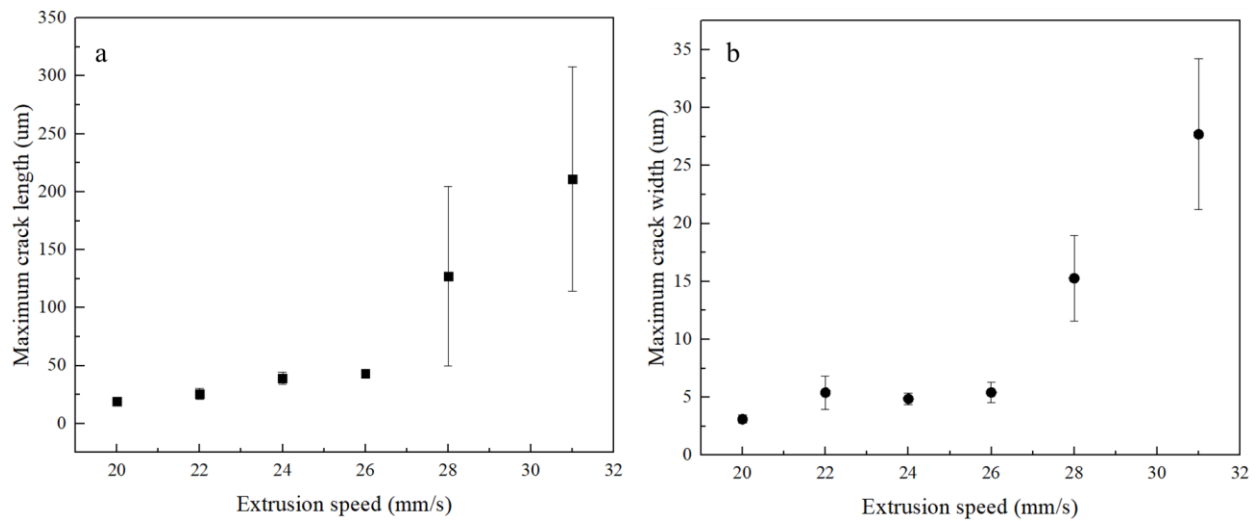


Figure 5-21 Surface maximum cracks change with extrusion speed in length (a) and width (b).

Figure 5-22 took the natural logarithm of the sizes of the longest and the widest surface cracks at different extrusion speeds and plotted them as the function of the extrusion speeds respectively. The figure shows that the natural logarithm of the sizes of the surface crack, either the width or the length, changes linearly with the extrusion speed. This can be attributed to both the temperature rise caused by greater work input at higher extrusion speeds and the higher strain rate the material is subject to at a higher extrusion speed, resulting in increased tensile stress experienced by the material.

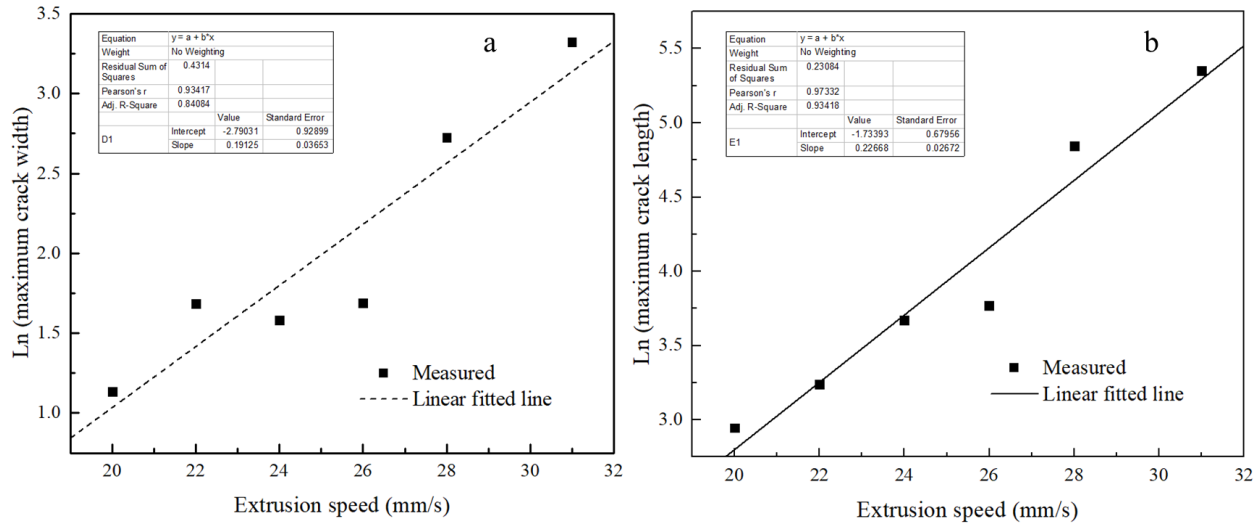


Figure 5-22 Relationship between the natural logarithm of (a) the maximum crack length width and the extrusion speeds, and (b) the maximum crack width and the extrusion speeds.

Figure 5-23 presents the Electron backscatter diffraction (EBSD) inverse pole figure (IPF) map in RD-ND plane of the extrudates produced by zero-bearing die at an extrusion speed of 28 mm/s using A612 material. This sample was chosen because the surface crack in this extrusion penetrates deep to the inside of the extrusion bar and can be observed clearly. It can be observed that the big surface crack propagates along the grain boundary and forms a 45° angle compared to

the extrusion direction. There are also some small cracks close to the extrudate surface and they also initiate from the grain boundary.

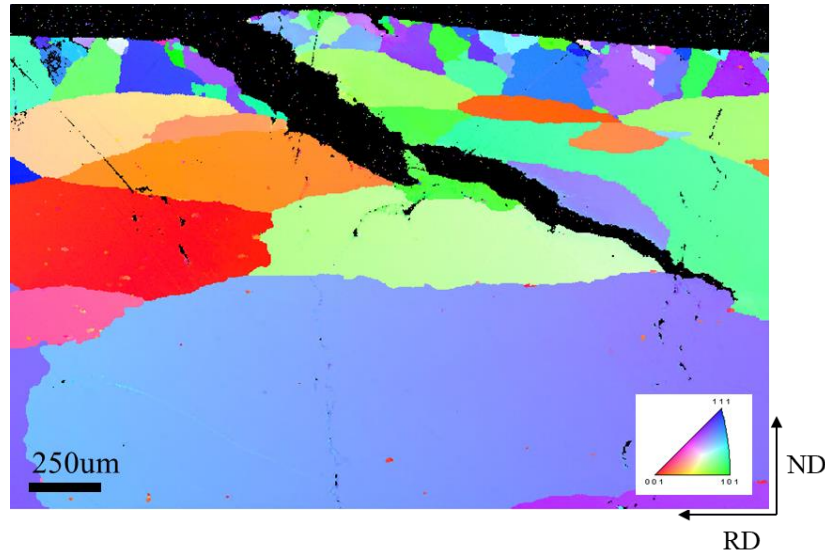


Figure 5-23 Electron backscatter diffraction (EBSD) inverse pole figure (IPF) map in RD-ND plane of the extrudates produced by a zero-bearing die at an extrusion speed of 28 mm/s using A612 material.

### 5.2.2.1 Surface visual observation

#### 5.2.2.1.1 Effect of extrusion ratio

Figure 5-24 provides a visual assessment of the extrudate produced using two distinct die configurations: (a) a 12 mm flat die with an extrusion ratio of 70:1 and (b) a 25 mm flat die with an extrusion ratio of 17:1 using A612 material. These samples were obtained from the back of the extrusion. In Figure 5-24 (a), featuring the extrusion ratio of 70:1, no visible cracks are evident on the bars within the extrusion speed range of 4 mm/s to 8 mm/s. Surface cracks become apparent at extrusion speeds of 9 mm/s and 10 mm/s. Conversely, in Figure 5-24 (b), where the extrusion ratio

is 17:1, no visible cracks are observable on the extrudate surface as the extrusion speed varies between 20 mm/s and 26 mm/s. However, small visible cracks do appear at extrusion speeds of 28 mm/s and 31 mm/s.

Notably, the extrusion ratio shows a significant influence on the extrusion speed at which surface cracks occur. Higher extrusion ratios lead to the occurrence of surface cracks at lower extrusion speeds. This phenomenon arises due to the higher extrusion ratio, which subjects the material to increased strain, strain rate and temperature [105]. All of these factors accelerate the occurrence of surface cracks at a lower extrusion speed at the higher extrusion ratio.

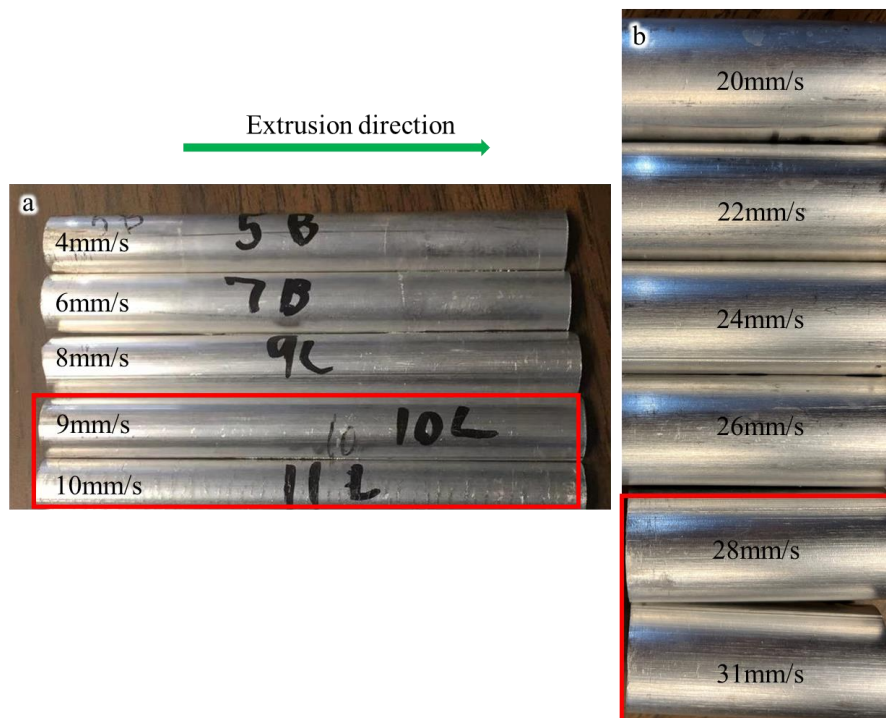


Figure 5-24 Surface visual observations of the samples from the back of the extrudates produced with A612 at various extrusion speed by dies with different extrusion ratios: (a) extrudates produced by 12 mm flat die with extrusion ratio of 70:1, (b) extrudates produced by 25 mm flat die with extrusion ratio of 17:1.

### 5.2.2.1.2 Effect of die geometry

Figure 5-25 illustrates the visual inspection of extrusion profile surfaces produced using four different die geometries, with (a) 25 mm flat die, (b) 35 mm choked die, (c) zero-bearing die, and (d) 12 mm choked die, all under the same conditions: a consistent extrusion ratio of 17:1 and utilizing A612 material. Across each die type, multiple extrusion speeds were tested, and all samples were prepared from the back of the extrusion. The initial billet temperatures of the trials from which the samples were prepared are all between 485°C and 495°C, falling slightly below the predetermined billet temperature of 500°C.

Regarding the 25 mm flat die in Figure 5-25 (a), extrusion speeds ranging from 20 mm/s to 31 mm/s were investigated. Notably, no visible surface cracks were observed within the speed range of 20 mm/s to 26 mm/s. However, small visible surface cracks began to show at an extrusion speed of 28 mm/s and 31 mm/s. For the zero-bearing die in Figure 5-25 (c), the extrusion profile surfaces were examined at extrusion speeds of 26 mm/s, 28 mm/s, and 29 mm/s. Among these, no surface cracks were observed at the extrusion speed of 26 mm/s, while small visible surface cracks significant visible cracks were exclusively observed at an extrusion speed of 28 mm/s and 29 mm/s respectively.

As for the 35 mm choked die in Figure 5-25 (b), no visible surface cracks were evident until reaching the maximum extrusion speed of the extrusion press, which is 40 mm/s. For the 12 mm choked die, the extrusion profiles at speeds of 28 mm/s, 32 mm/s, and 34 mm/s were inspected, and no cracks were observed at all speeds.

From the above analysis it is clear that the die geometry plays a significant role in the extrusion surface crack occurrence. For both the 25 mm flat die and the zero-bearing die without

choked angle at the die corner, visible surface cracks were observed at the same extrusion speed. While for both choked dies no surface cracks were observed at the examined extrusion speeds.

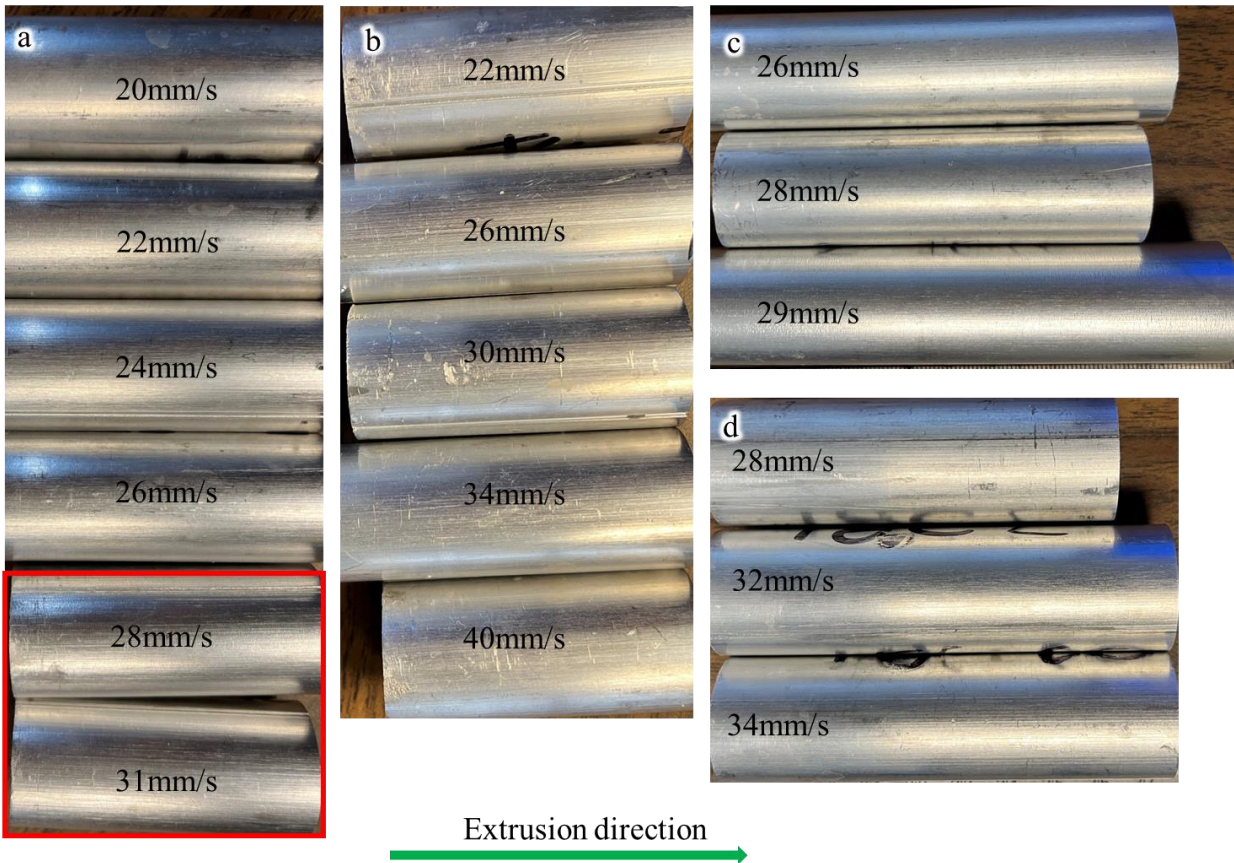


Figure 5-25 Surface visual observation of the samples from the back of the extrusion profiles extruded by four different die geometries at varying extrusion speed with the same extrusion ratio of 17:1 using A612: (a) 25 mm flat die, (b) 35 mm choked die, (c) zero-bearing die, and (d) 12 mm choked die.

### 5.2.2.1.3 Effect of Cu

Figure 5-26 illustrates the surface characteristics observed in samples extruded using a 25 mm flat die with varying Cu contents in the material. All samples were extracted from the back of the extrusion process. The extrusion direction is from the left to the right of the figure. Subfigure



(a) of Figure 5-26 displays the extrusion surface produced with material A612, where the extrusion speeds ranged from 20-31 mm/s. In contrast, Subfigure (b) of Figure 5-26 exhibits the extrusion surface generated with material A613, involving extrusion speeds varying from 5-20 mm/s.

Evidently, the material composition exerts a discernible influence on the quality of the extruded surface. In Figure 5-26 (a), extrudates remain free of visible surface cracks at speeds up to 26 mm/s. However, when the extrusion speed reaches 28 mm/s and 31 mm/s, small visible cracks become apparent. Conversely, Subfigure (b) of Figure 5-26 shows no visible cracks at extrusion speeds of 5 mm/s and 10 mm/s. As the extrusion speed escalates to 15 mm/s, small visible cracks begin to emerge, and further increasing the speed to 20 mm/s results in prominent, visible cracks.

Notably, both minor and major visible cracks occur at lower extrusion speeds in the case of A613 when compared to the extrusion speed at which A612 displays only minor visible surface cracks. This suggests that addition of Cu content makes the material more susceptible to surface cracks, which manifest at lower extrusion speeds while all other conditions keep almost constant.

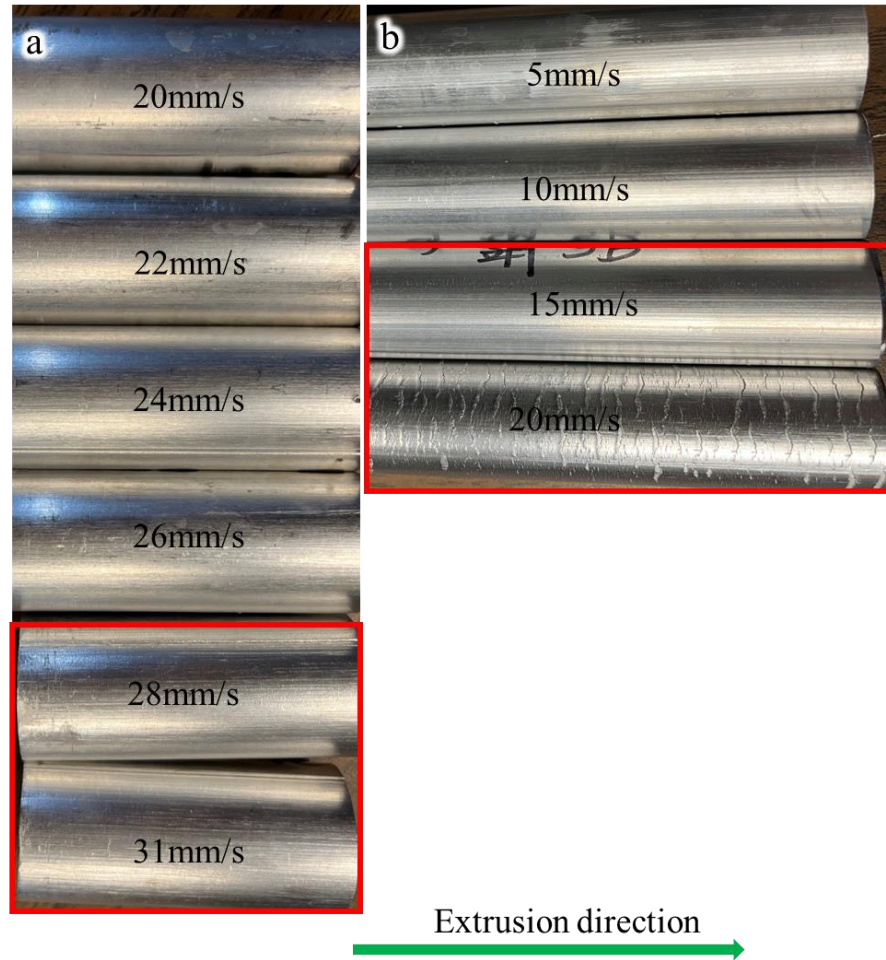


Figure 5-26 Surface visual observation of the samples from the back of the extrusion profiles extruded by 25 mm flat die using materials with different Cu contents: (a) A612 with extrusion speed varying from 20-31 mm/s, and (b) A613 with extrusion speed varying from 5-20 mm/s.

### 5.2.2.2 Surface observation by SEM

In this section, we exclusively focus on the impact of die geometry and Cu content on the SEM images of the extrudate surface. As for trials involving various extrusion ratios, their SEM images are not compared here due to the considerable variation in extrusion speeds, making a direct comparison less meaningful.

#### 5.2.2.2.1 Effect of die geometry

Figure 5-27 displays the surface morphology of the samples from the back of the extruded length produced by the 25 mm flat bearing using A612, with figures (a) to (f) representing extrusion speeds of 20 mm/s, 22 mm/s, 24 mm/s, 26 mm/s, 28 mm/s, and 31 mm/s, respectively. The extrusion direction is from the bottom to the top of the images. The longitudinal lines along the extrusion direction are die lines. As the extrusion speed increases, certain changes in the extrudate surface become evident. At lower speeds (a and b), the extrudate appears smooth and exhibits minimal irregularities, with the surface morphology being characterized by small micro-cracks that are not visible to the naked eye. However, as the speed increases (c to f), the surface exhibits progressively larger surface cracks, indicating clear damage to the extrudate surface during the extrusion process.

To gain a more comprehensive understanding of the extrudate produced at the highest speed (31 mm/s), Figure 5-27 (g-i) show the surface morphology from different positions on the sample: front, middle, and back, respectively. These figures reveal variations in the extrudate's surface texture and defect evolution along its length. The front portion has a smooth and relatively defect-free surface morphology compared to the more pronounced irregularities at the middle and back sections. This observation suggests that the surface quality deteriorates towards the middle and back regions. While the strain rate remains constant at a particular extrusion speed, the temperature is the primary factor that changes. Initially, the temperature rises rapidly, eventually reaching a nearly steady state [41]. This observation suggests that the extrusion process, at an initially lower temperature, does not lead to any apparent surface defects but as the surface temperature of the extrudate increases as it approaches the middle and back sections, with the stresses near the die outlet acting on the surface, distinct surface features begin to appear, as clearly seen in Figure 5-27.

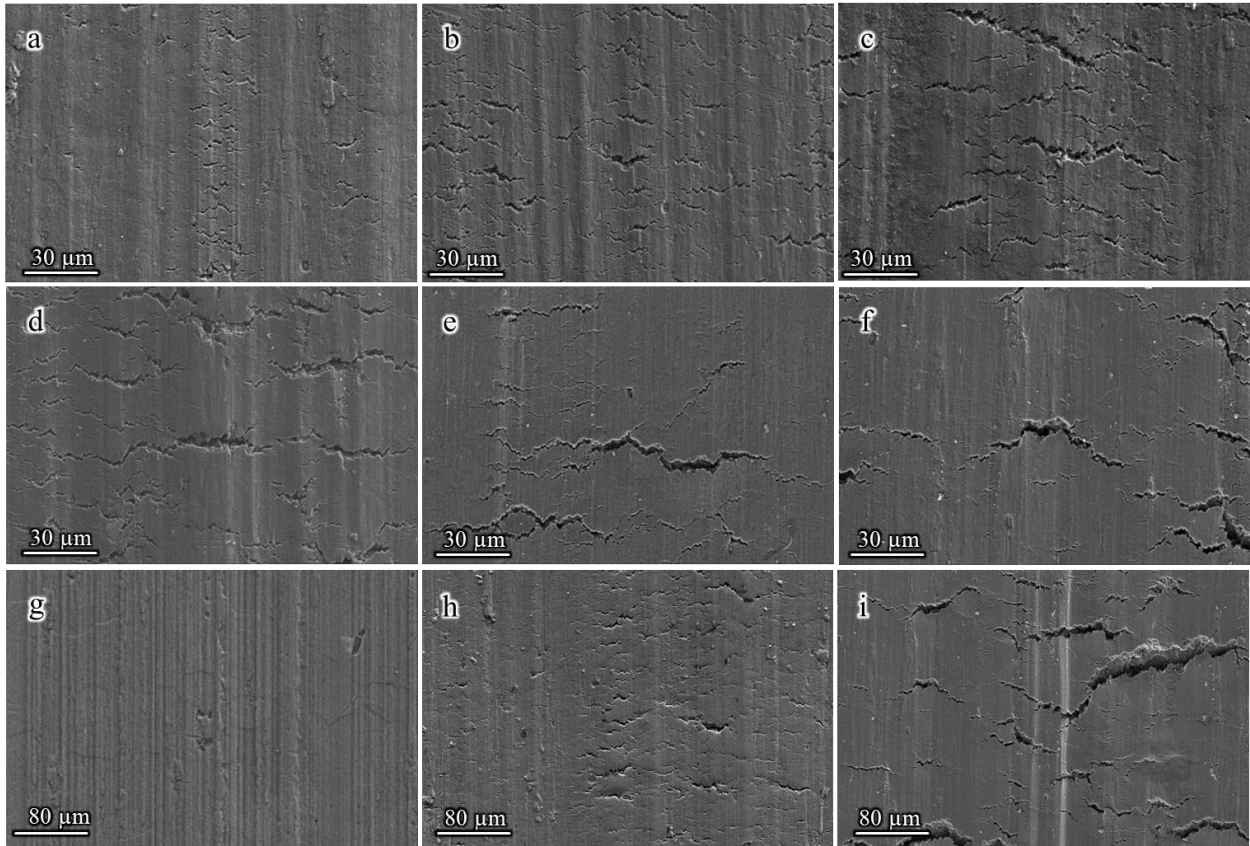


Figure 5-27 Surface morphology of extrudates produced by a 25 mm flat die using A612 with an extrusion speed of (a) 20 mm/s, (b) 22 mm/s, (c) 24 mm/s, (d) 26 mm/s, (e) 28 mm/s, and (f) 31 mm/s. Figures (g-i) show the surface morphology of the extrudate from the front, middle, and back of the sample produced with an extrusion speed of 31 mm/s, respectively. Extrusion direction from bottom to top.

Figure 5-28 shows higher magnification images of the surface at the back of extrusions produced by a 25 mm flat die at two different extrusion speeds using A612: (a) 20 mm/s and (b) 26 mm/s. The observations suggest that surface cracking predominantly occurs along the exposed grain boundaries of the extrudates.

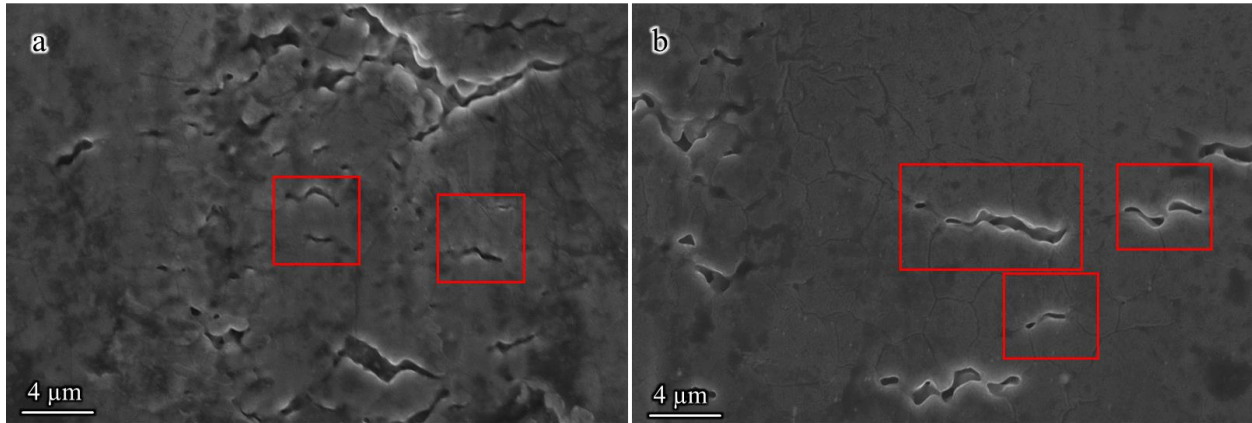


Figure 5-28 Surface crack locations of the extrudate produced by a 25 mm flat die using A612 at an extrusion speed of (a) 20 mm/s and (b) 26 mm/s, suggests that surface cracking occurs at exposed grain boundaries.

Figure 5-29 shows the surface morphology of extrudates produced by a 35 mm choked bearing at various extrusion speeds (ranging from 22 mm/s to 40 mm/s) using A612. No surface cracking was observed for any of the extrudates, regardless of the extrusion speed. This is in contrast to the previous findings with the 25 mm flat bearing, where significant surface cracking was evident.

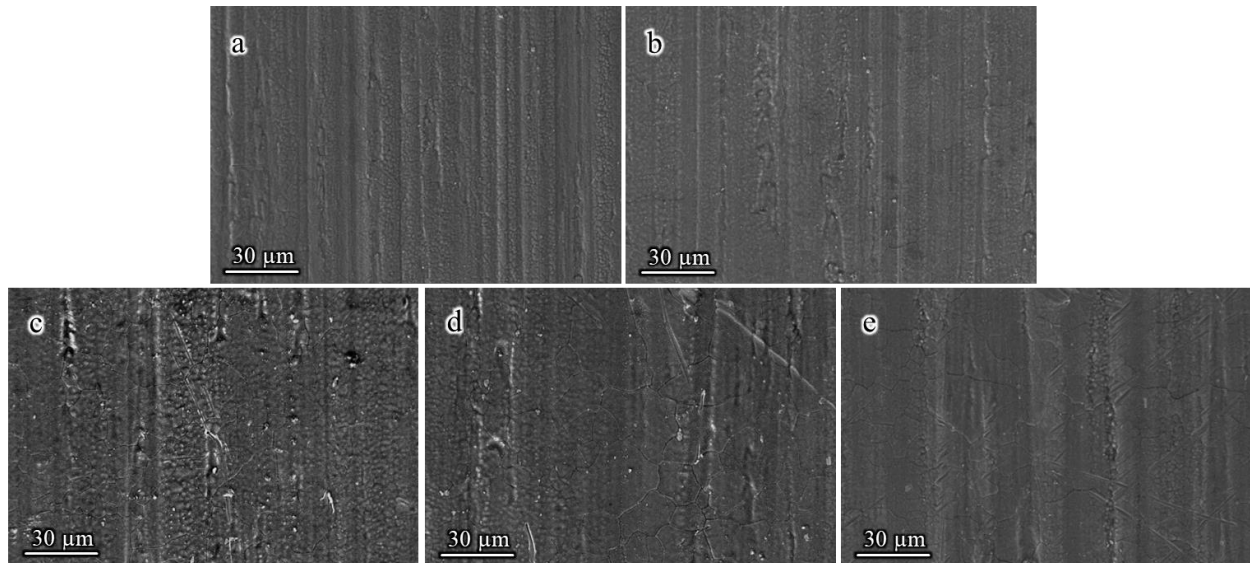


Figure 5-29 Surface morphology of extrudates produced by a 35 mm choked die using A612 material with an extrusion speed of (a) 22 mm/s, (b) 26 mm/s, (c) 30 mm/s, (d) 34 mm/s, and (e) 40 mm/s.

Figure 5-30 and Figure 5-31 present a comparative analysis of the surface morphology of extrudates produced by the 12 mm choked and zero-bearing dies, respectively using A612. Notably, similar to the 35 mm choked die, the 12 mm choked die exhibits resistance to surface cracking, regardless of the extrusion speed. In Figure 5-30 (a-c), where extrusion speeds range from 28 mm/s to 34 mm/s, there is a consistent absence of surface cracks in all extrudates.

In contrast, the extrudates produced with the zero-bearing die (Figure 5-31) reveal a different behavior. At slower extrusion speeds (26 mm/s), the surface morphology in Figure 5-31 (a) appears relatively smooth, showing relatively minimal defects. However, as the extrusion speed increases, Figure 5-31 (b-c) display a pronounced presence of cracks on the surface. At high speeds, the cracks become more significant and extensive, compromising the overall quality of the extrudate. These observations imply that the zero-bearing die design is less effective in mitigating

stress concentrations, especially at higher extrusion speeds, leading to the development of surface cracks.

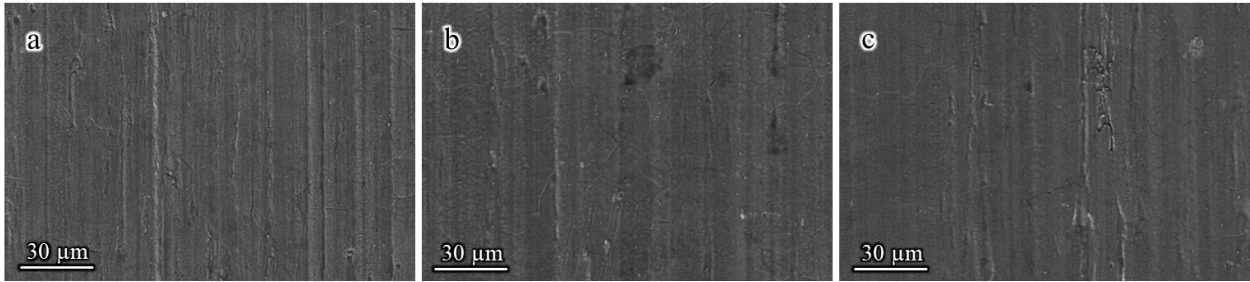


Figure 5-30 Surface morphology of extrudates produced by a 12 mm choked die using A612 with an extrusion speed of (a) 28 mm/s, (b) 32 mm/s, and (c) 34 mm/s.

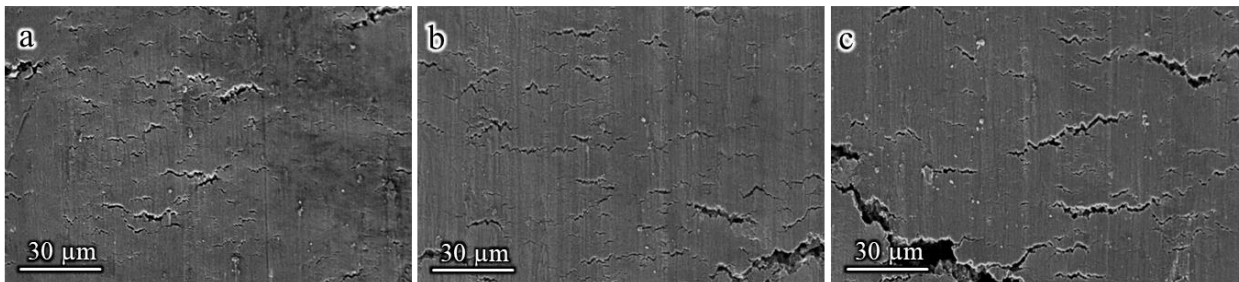


Figure 5-31 Surface morphology of extrudates produced by a zero-bearing die using A612 with an extrusion speed of (a) 26 mm/s, (b) 28 mm/s, and (c) 29 mm/s.

The comparison between the various die designs clearly demonstrates the superior performance of the choked dies in preventing surface cracking of AA6xxx alloys during extrusion, even under varying extrusion speeds. The choked die's ability to maintain a controlled extrusion process and distribute stress more evenly ensures a defect-free surface in the extrudates. In contrast, the flat die and the zero-bearing die show a vulnerability to surface cracking, particularly at higher extrusion speeds, indicating the importance of selecting appropriate die designs to achieve high-quality extruded products with AA6xxx alloys.

Figure 5-32 provides a comprehensive comparison of the as-extruded surface morphology of samples from the back of the extrudates produced using the four different die geometries discussed earlier, at a constant extrusion speed of 26 mm/s (28 mm/s for the 12 mm choked die) using A612 material. To capture the maximum damage in the extrusion profile's surface morphology, the samples were taken from the back of the extrudate. The observations in the figure shed light on the performance of each die design in terms of surface morphology and integrity. At the specified extrusion speed, both the 25 mm flat die and the zero-bearing die exhibit surface cracks on the as-extruded profiles (Figure 5-32 a & c). These cracks are clear indicators of stress concentration and potential material defects, which could compromise the overall quality and structural integrity of the extrudates. In contrast, the extrusion profiles produced using the two choked dies show a markedly different behavior. While there are no visible cracks on the surfaces of these extrudates, grain boundaries are also clearly discernible at this magnification (Figure 5-32 b & d). This suggests that the choked dies successfully prevent surface cracking, highlighting their superior ability to maintain a stress distribution that prevents surface defects from forming during the extrusion process.



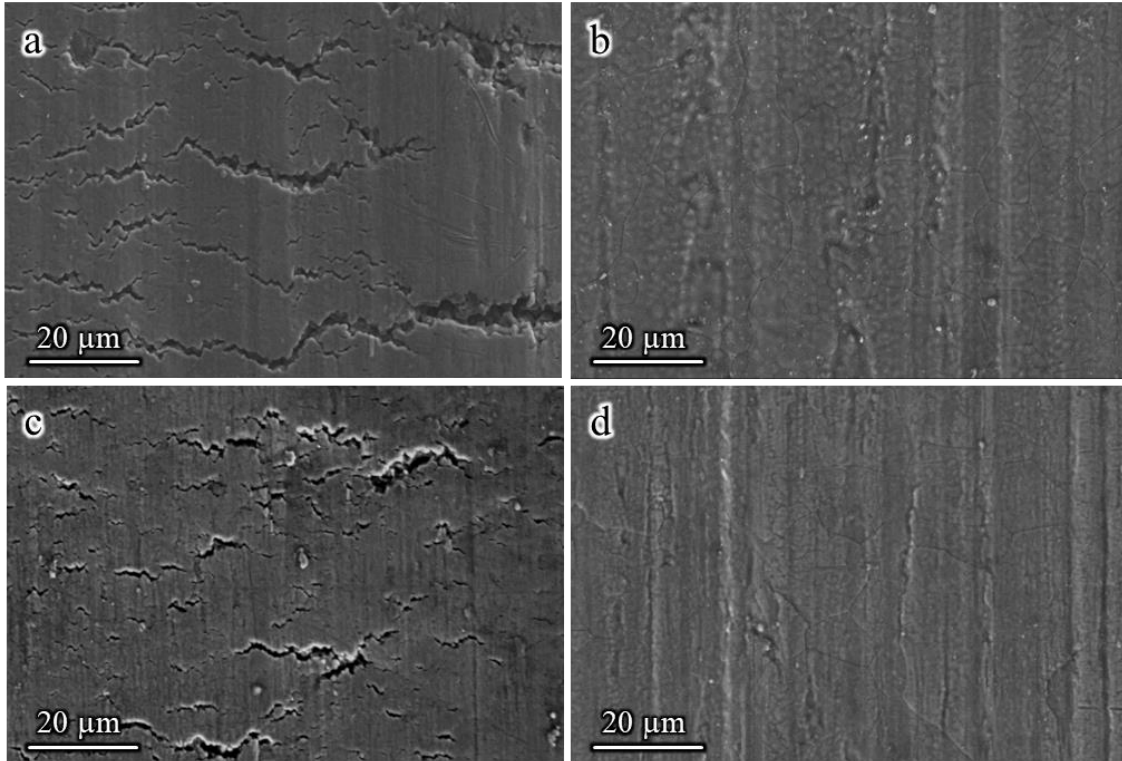


Figure 5-32 Surface morphology comparison of extrusion profiles produced by four die geometries from the back of the extrudates and at a similar extrusion speed using A612 material: (a) 25 mm flat die at 26 mm/s; (b) 35 mm choked die at 26 mm/s; (c) zero-bearing die at 26 mm/s; and (d) 12 mm choked die at 28 mm/s. Extrusion direction from bottom to top.

#### 5.2.2.2 Effect of Cu

Figure 5-33 shows the surface morphology of extrudates produced using materials with different Cu contents. In Figure 5-33 (a) and (b), the extrudates were produced using the 25 mm flat die and at an extrusion speed of 20 mm/s, utilizing the A612 and A613 respectively. Small micro-sized cracks scattered across the surface were observed in Figure 5-33 (a), with the cracks appearing along the boundaries of individual grains, as shown by Figure 5-33 (a1). In contrast, the extrudates generated with a higher Cu content material A613 using the same flat die and extrusion speed in Figure 5-33 (b) exhibited notably larger surface cracks when compared to the A612

extrudates. The cracks were again predominantly concentrated along the grain boundaries as evidenced by Figure 5-33 (b1). The addition of Cu lowers the solidus temperature of the material, which is mentioned in literature [106,107] and also observed in the DSC tests conducted in this work, where the A612 material had a solidus temperature of around 590°C while the A613 sample showed a lower solidus temperature of about 583°C. When the extrusion speed is the same, both materials reach the same or similar maximum temperature during the extrusion process. However, for A613 a larger portion of the grain boundaries melted, which makes the extrusion with A613 can induce surface cracks easier when the stress of the material went through is the same.

The extrudates produced using the 35 mm choked die showed that both the A612 samples Figure 5-33 (c) and the A613 samples Figure 5-33 (d) had no visible surface cracks, indicating that even with higher Cu content, the 35 mm choked die cannot induce surface cracks. Clear grain boundaries can be observed in both the figures, with the one extruded from A613 showing a bigger grain size.

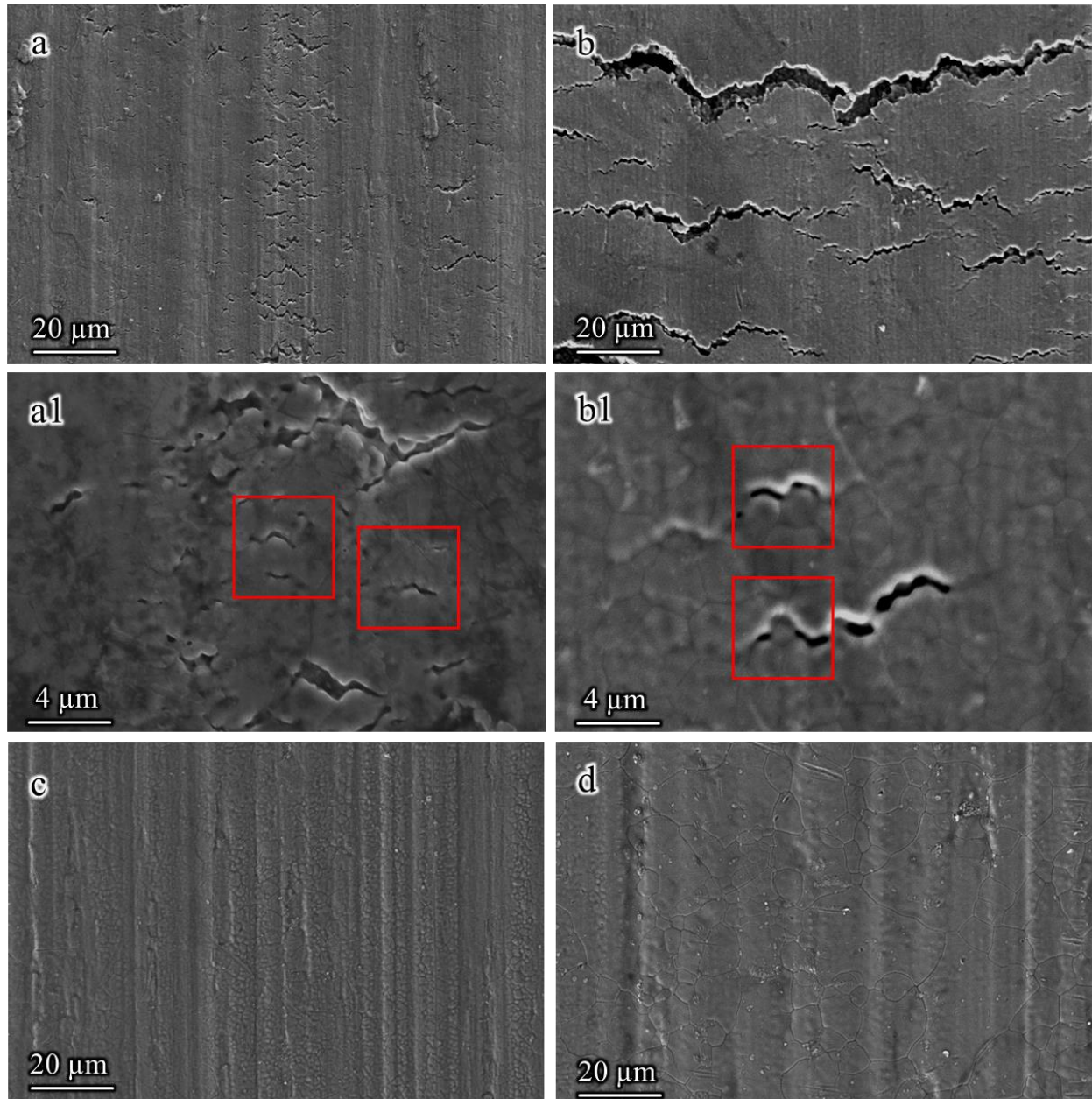


Figure 5-33 Surface morphology of extrudates produced using materials with different Cu contents. (a) and (b) are surface morphology images of A612 and A613, respectively, extruded by a flat die at an extrusion speed of 20 mm/s, (a1) and (b1) are the high magnification images of (a) and (b) showing the crack location respectively; (c) and (d) are surface morphology images of A612 and A613 extruded by 35 mm choked die at an extrusion speed of 22 mm/s and 20 mm/s respectively.

### **5.2.2.3 PCG layer**

This section discussed the effect of die geometry and Cu content on the extrudates. The effect of the extrusion ratio is not discussed because in the extrusion trials using dies with different extrusion ratios the extrusion speed is totally different, which makes it is meaningless to compare the microstructure.

#### **5.2.2.3.1 Effect of die geometry**

Figure 5-34 presents microstructure images of cross sections perpendicular to the extrusion direction of the extrudates from the back of the extrusion. These were obtained from various die configurations using A612 material: (a) a 25 mm flat die, (b) a zero-bearing die, (c) a 12 mm choked die, and (d) a 35 mm choked die . The extrusion speed was set at 26 mm/s for all dies, except for the zero-bearing die, which used an extrusion speed of 28 mm/s, which is in order to make the starting billet temperature keep similar for all dies.

The microstructural observations reveal that both the 25 mm flat die and the zero-bearing die produce a PCG layer with similar thickness. Comparatively, the PCG layer from the 12 mm choked die is slightly thinner than those produced by the 25 mm flat and zero-bearing dies. The 35 mm choked die yields the thinnest PCG layer.

In a related study by Mahmoodkhani et al. [87], extrusion trials were conducted using both the zero-bearing and 35 mm choked die under the same extrusion conditions. The results indicated a close connection between the PCG layer thickness and the stored energy within the extrudates. The equation they used to calculate the stored energy is proportional to the flow stress of the material. By using FEM they calculated that the zero-bearing die exhibited a higher stored energy (approximately 5%) across the extrudate radius compared to that of extrudates produced by the 35 mm choked die.

Our results align with the result of this research. The extrudates produced by the 35 mm choked die experience a lower stress at the die corner compared to the 25 mm flat and zero-bearing dies, which results in a thinner PCG layer. This is discussed in detail in Section 5.3. It can also be concluded that as the choked angle increases, the PCG layer thickness decreases when comparing the PCG layers from both the choked dies.

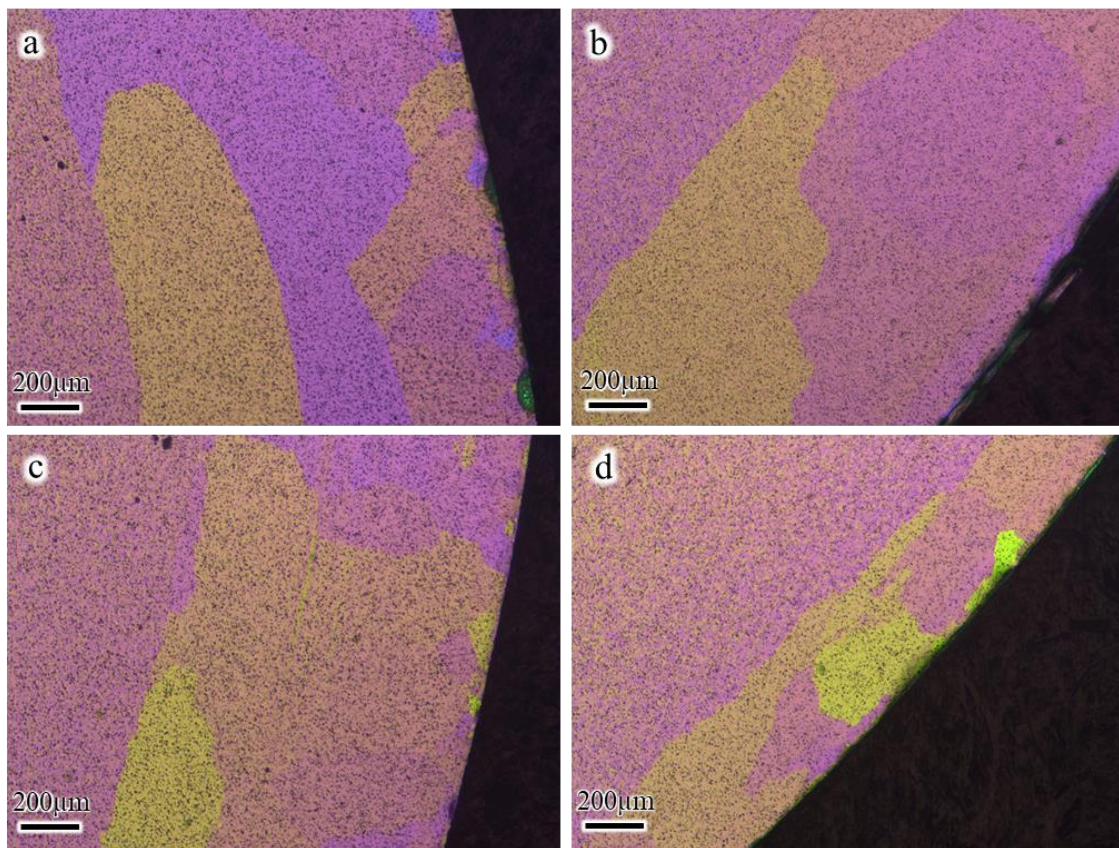


Figure 5-34 Microstructure images of the cross section perpendicular to the extrusion direction of the back extrudates produced by: (a) 25 mm flat die (b) zero-bearing die, (c) 12 mm choked die, and (d) 35 mm choked die at an extrusion speed of 26 mm/s for all die except the zero-bearing die (28 mm/s) using A612.

### 5.2.2.3.2 Effect of Cu

Figure 5-35 depicts the PCG layer microstructure of the cross section perpendicular to the extrusion direction of the samples from back of the extrusion extruded by two dies, with each die two materials A612 and A613 being extruded at the same and/or similar extrusion speed. In Figure 5-35 (a) and (b), it shows the microstructure images of A612 and A613, respectively, which were extruded using the 25 mm flat die at an extrusion speed of 20 mm/s. It is noteworthy that the samples from A613 exhibit a slightly thicker PCG layer compared to A612. When the extrusion condition is the same, the strain, strain rate and the temperature that the material goes through are the same. Because A612 exhibits a higher solidus temperature than A613, the temperature increase percentage of A613 is higher than that of A612 compared to the solidus temperature at the same stage of the extrusion. Higher temperature during the extrusion process is beneficial to recrystallization, which is probably the reason for a thicker PCG layer in A613.

In Figure 5-35 (c) and (d), it presents microstructure images of samples prepared from A612 and A613 extrudates, extruded by the 35 mm choked die at extrusion speeds of 22 mm/s and 20 mm/s, respectively. The microstructure of A612 shows an obvious thinner PCG layer compared to that of A613. This can be attributed to the slightly higher starting billet temperature ( $\sim 10^{\circ}\text{C}$ ) for A613 on one side; on the other side A613 has lower solidus temperature and can be reached at a relatively stage of the extrusion. Both the reasons result in a much thicker PCG layer in Figure 5-35 (d). No matter which die is used, the increase in Cu content promotes the formation of PCG layer and a thicker PCG layer is observed in the extrudates with a higher Cu content.

However in some literature, it is mentioned that Cu content increases the retarding force of recrystallization by increasing the number of intermetallic particles and dispersoids [108,109]. So Cu has a negative effect on the formation of PCG layer. The effect of Cu on the intermetallic

particles and dispersoids in the microstructure has not been studied yet in this research, but it is believed that the solidus temperature plays a more important role in the formation of the PCG layer.

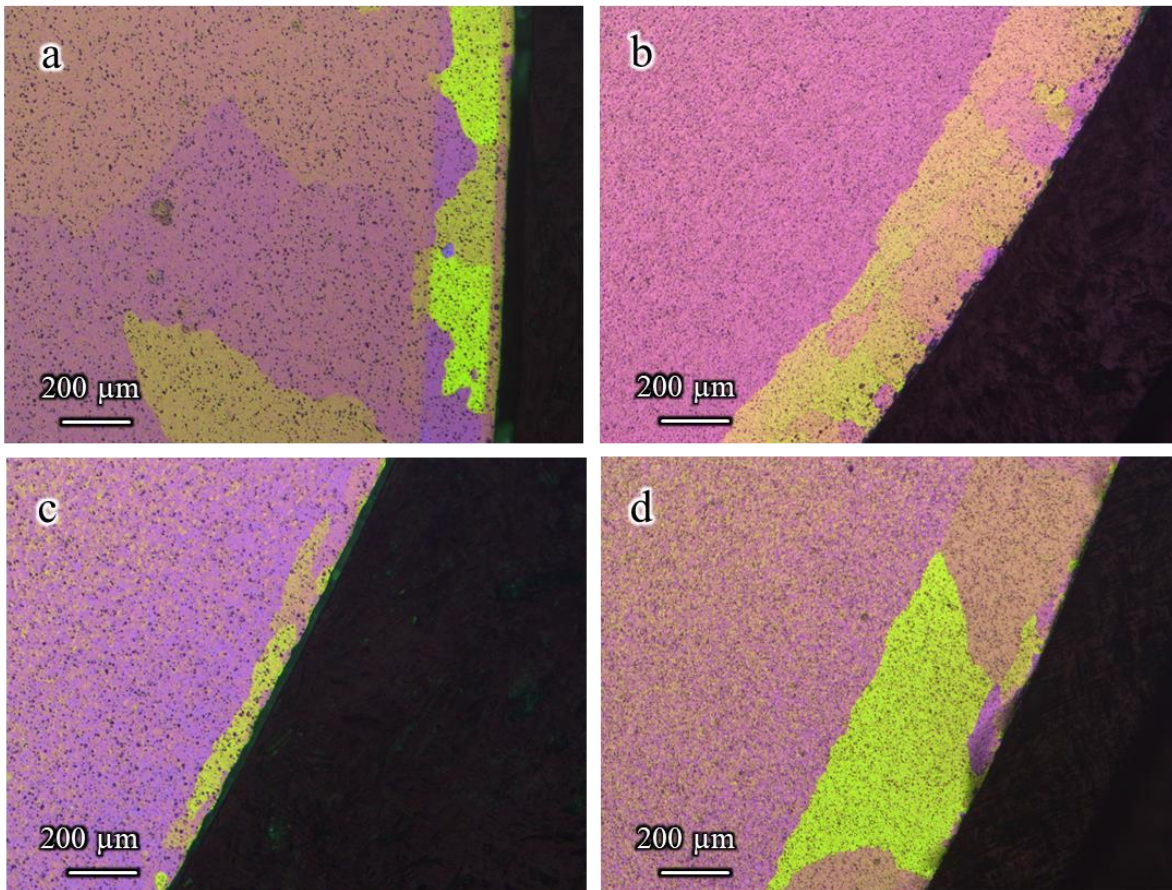


Figure 5-35 Microstructure images of the cross section perpendicular to the extrusion direction using materials with different Cu contents: (a) and (b) are microstructure images of A612 and A613, respectively, extruded by a flat die at an extrusion speed of 20 mm/s; (c) and (d) are microstructure images of A612 and A613 extruded by choked die at an extrusion speed of 22 mm/s and 20 mm/s respectively.

#### 5.2.2.4 Surface roughness

##### 5.2.2.4.1 Effect of die geometry

Figure 5-36 presents a comparison of surface roughness for extrudates produced by the four different die geometries using A612, at a similar extrusion speed. The roughness values for each die configuration are as follows:  $0.77\mu\text{m}$  for the 25 mm flat die,  $0.43\mu\text{m}$  for the 35 mm choked die,  $0.61\mu\text{m}$  for the zero-bearing die, and  $0.40\mu\text{m}$  for the 12 mm choked die. A lower roughness value indicates a smoother surface. Accordingly, the two choked dies exhibit relatively lower roughness values compared to the 25 mm flat die and the zero-bearing die.

The variation in surface roughness can be attributed to the observed cracking behavior in the extrudates. As Figure 5-36 reveals, surface cracks are evident in the extrusion profiles produced by the 25 mm flat die and the zero-bearing die. These cracks contribute to increased surface roughness due to the disruption of the smooth surface, introducing irregularities and imperfections. In contrast, the extrusion profiles generated by the two choked dies show significantly smoother surfaces with minimal or no surface cracks, resulting in lower roughness values. This observation further emphasizes the importance of die geometry in influencing not only surface cracking but also the overall surface quality of the extrudates.

The data from Figure 5-36 reinforces the correlation between die design, surface cracking behavior, and surface roughness of AA6xxx alloy extrudates. The choked dies exhibit superior performance in achieving smoother surfaces, which is advantageous for applications requiring high-quality extruded products. The reduced surface roughness achieved by the choked dies is a result of their ability to mitigate stress concentrations and prevent surface cracking, underscoring the importance of proper die design to optimize product quality. These results provide valuable insights into the selection and optimization of die geometries for extrusion processes involving AA6xxx alloys, ultimately enhancing the quality and performance of the final extrudates.



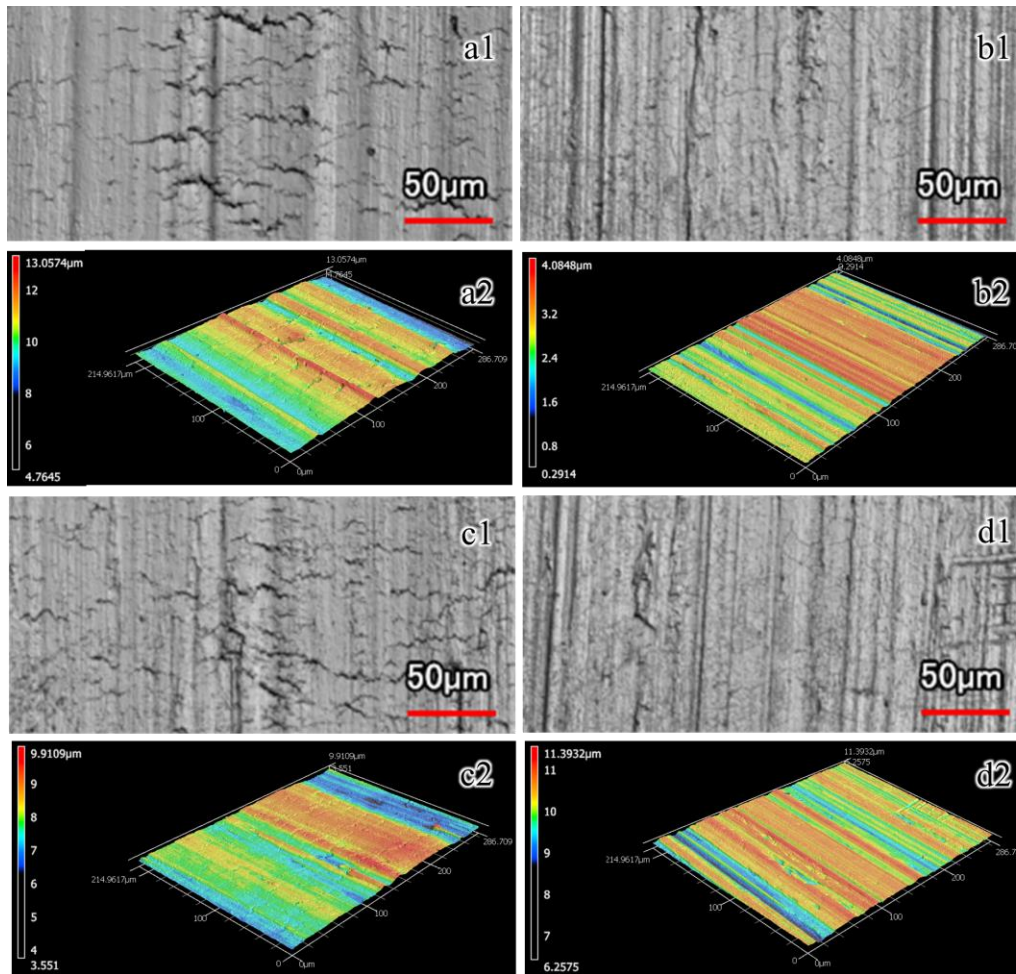


Figure 5-36 3D surface roughness and laser confocal micrography images showing the comparison of extrusion profiles produced by four die geometries using A612 at a similar extrusion speed: (a) 25 mm flat die at 26 mm/s; (a) 35 mm choked die at 26 mm/s; (a) zero-bearing die at 26 mm/s; and (a) 12 mm choked die at 28 mm/s. Extrusion direction is from the bottom to the top of the figure.

#### 5.2.2.4.2 Effect of Cu

Figure 5-37 presents the measured surface roughness images of the extrudates produced with materials with different Cu contents. The samples were all taken from the back of the extrudates. In Figure 5-37 (a) and (b), the extrudates were produced using the 25 mm flat die and at an extrusion speed of 20 mm/s, utilizing the A612 and A613 respectively. The surface roughness

images of the 3D profilometry images show roughness values of  $0.41\mu\text{m}$  and  $1.73\mu\text{m}$  for A612 and A613, respectively. The big difference in surface roughness values is mainly caused by the big difference in surface crack size.

Figure 5-37 (c) and (d) show the surface roughness images of the extrudates produced with A612 and A613 using a 35 mm choked die at extrusion speed of 22 mm/s and 20 mm/s respectively. These two images have a roughness value of  $0.47\mu\text{m}$  and  $0.86\mu\text{m}$ , respectively, clearly showing that the extruded surfaces get rougher with the addition of Cu. This is because the temperature is closer to the solidus temperature of the material with a higher Cu addition.

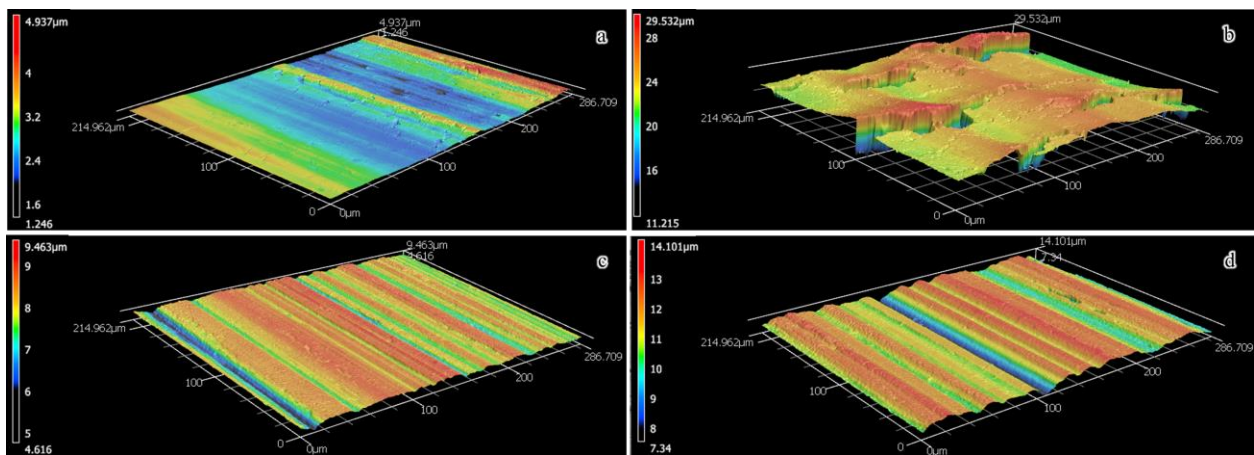


Figure 5-37 Surface roughness images of the samples taken from the back of the extrudates with different Cu contents: (a) and (b) are surface roughness of A612 and A613, respectively, extruded by a flat die at an extrusion speed of 20 mm/s; (c) and (d) are surface roughness of A612 and A613 extruded by choked die at an extrusion speed of 22 mm/s and 20 mm/s respectively.

## 5.3 Model predictions

In the Finite Element Method (FEM) modeling, the constitutive model based on A612 was applied to all three materials with varying Cu content. This decision was made due to the minimal effect Cu appeared to have on the high temperature flow stress behavior. Consequently, the model-predictions for stress, temperature and load are the same for all three materials when subjected to similar extrusion conditions, including die geometry, extrusion speed and billet temperature. As a result, this section is primarily dedicated to the analysis of stress and temperature variations arising from different extrusion ratios and die geometries.

Considering that the material goes through the most severe plastic deformation at the die corner, and the extrudate surface then continues to interact with the die bearing, the numerical modelling analysis was therefore focused on the stress and temperature distribution at the die corner and along the die bearing.

### 5.3.1 Effect of extrusion ratio

Figure 5-38 shows the distribution of all the calculated stress components at the die corner from the center to the surface of the billet for the dies using A612 with an extrusion ratio of 17:1 in Figure 5-38 (a) and extrusion ratio of 70:1 in Figure 5-38 (b) at the same extrusion speed of 6 mm/s, while Figure 5-39 shows the corresponding temperature distribution. The stress curves change from negative value (indicating a compressive load) to positive value (indicating a tensile load) from the center to the surface of the billet with the maximum value being reached at the surface, implying that the surface of the sample is prone to cracking. The following stresses have been calculated and shown in the figure:  $\sigma_R$  is the radial stress,  $\sigma_{RZ}$  is the shear stress,  $\sigma_\theta$  is the hoop stress, and  $\sigma_Z$  is the longitudinal stress.

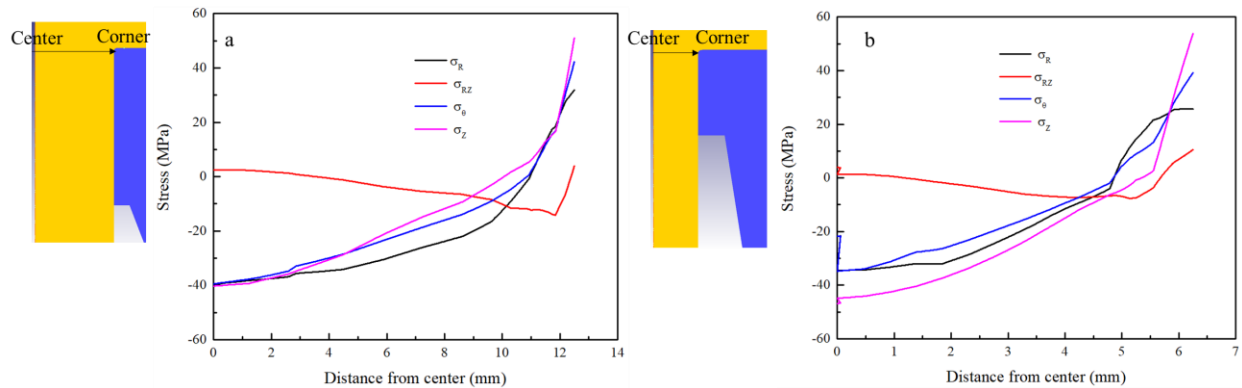


Figure 5-38 Model-predicted stress components from the center to the surface at the die corner at an extrusion speed of 6 mm/s for dies with an extrusion ratio of: (a) 17:1, (b) 70:1 at a stroke of 150 mm using A612.

Figure 5-38 (a) shows the stress component distribution of the die with an extrusion ratio of 17:1.  $\sigma_\theta$ ,  $\sigma_R$  and  $\sigma_z$  change in a similar trend from the center to the surface of the billet, among which  $\sigma_z$  is the highest and is approximately 50 MPa.  $\sigma_{RZ}$  is almost entirely below zero, which implies that this is a compressive stress and therefore does not contribute to the formation of surface cracks. Figure 5-38 (b) shows the stress component distribution of the die with an extrusion ratio of 70:1.  $\sigma_{RZ}$  in this figure is similar as than in Figure 5-38 (a) and almost fully below zero.  $\sigma_\theta$ ,  $\sigma_R$  and  $\sigma_z$  show the same trend as the same stress in Figure 5-38 (a), and the magnitude of them are also close. A higher extrusion ratio means a smaller opening at the die exit. When the billet diameter is the same, the billet that goes through a smaller opening gets to be extruded to a longer profile, which implies that the material experiences a higher stress along the extrusion direction. At the same time the temperature is also higher due to more work input, which is shown in Figure 5-39.

Figure 5-39 shows the corresponding temperature distribution across the billet from the center to the surface at die corner for dies with different extrusion ratios at an extrusion speed of 6 mm/s and a stroke of 150 mm using A612. The temperature consistently rises from the billet's center to its surface due to material deformation and interaction with the die bearing. Obviously, the temperature for the die with the extrusion ratio of 70:1 is much higher than the temperature for the die with the extrusion ratio of 17:1 due to more severe deformation the material experienced when the material passed through a smaller die exit.

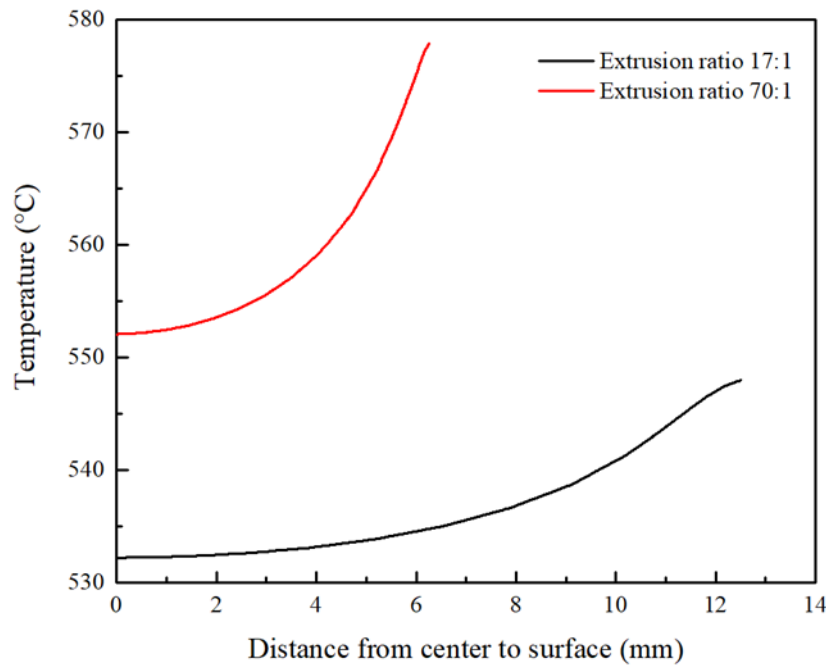


Figure 5-39 Model-predicted temperature distribution from the center to the surface of the billet at die corner at an extrusion speed of 6 mm/s by dies with an extrusion ratio of 17:1 and 70:1 at a stroke of 150 mm. The starting billet temperature is 480°C and material is A612.

Figure 5-40 (a) and (b) depict contour maps of  $\sigma_z$  (stress), while Figure 5-40 (a1) and (b1) provide corresponding contour maps of temperature. These maps related to dies with extrusion

ratios of 17:1 and 70:1, respectively. The material used is A612. The results indicate a common trend for both dies: stress and temperature exhibit pronounced concentration primarily at the die corner. Notably, in the die with an extrusion ratio of 17:1, the stress is similar to that of the die with an extrusion ratio of 70:1, but the temperature level at the die bearing region is lower compared to the die featuring an extrusion ratio of 70:1.

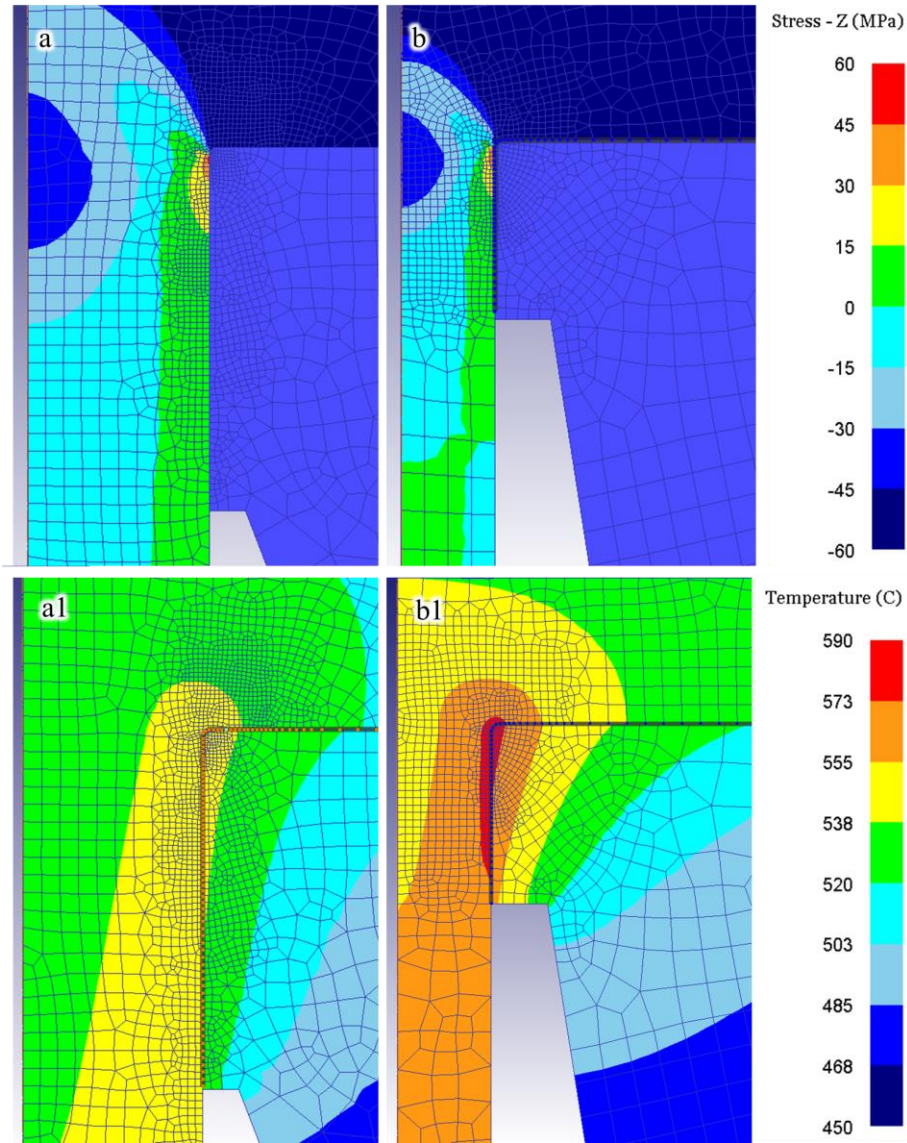


Figure 5-40 Model-predicted  $\sigma_z$  and temperature contour map at the die bearing region for die with extrusion ratio of 17:1 (a and a1) and 70:1 (b and b1) at the extrusion speed of 6 mm/s at a stroke of 150 mm with A612.

Figure 5-41 provides insight into the distribution of  $\sigma_z$  and temperature along the die bearing for dies with different extrusion ratios using A612. As identified in the contour maps, Figure 5-41 confirms that in both dies, the highest stress and temperature point were at the die

corner. Both the stress and the temperature are higher for the die with a smaller extrusion ratio. This outcome aligns with the stress contour map showcased in Figure 5-40 Figure 5-44.

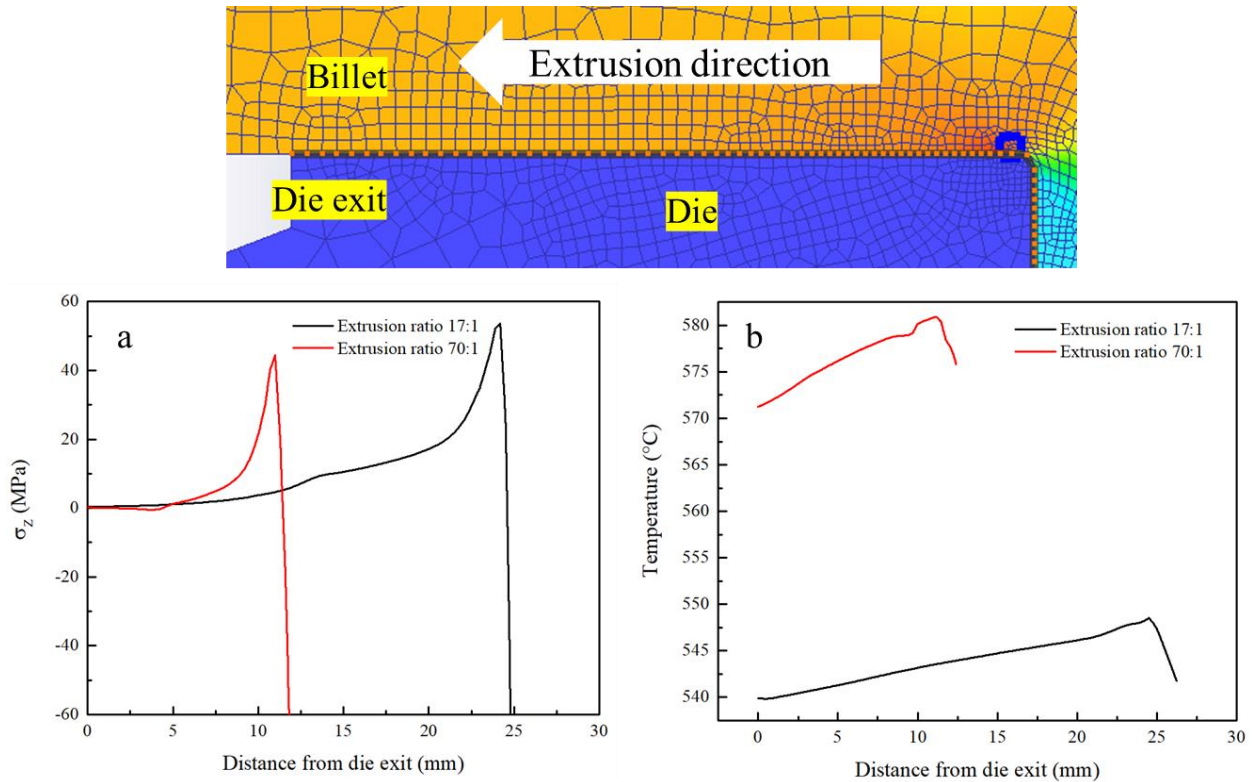


Figure 5-41 Model-predicted (a)  $\sigma_z$  and (b) temperature distribution along the die bearing for dies with extrusion ratio of 17:1 and 70:1 at a stroke of 150 mm at the extrusion speed of 6 mm/s with material A612.

### 5.3.2 Effect of die geometry

Figure 5-42 shows the distribution of all the calculated stress components for different dies using A612 at the die corner from the center to the surface of the billet at the same extrusion speed of 26 mm/s, with Figure 5-43 showing the corresponding temperature distribution. All the stress curves have a negative value (indicating a compressive load) or change from a negative to positive



value (indicating a tensile load) from the center to the surface of the billet with the maximum value being reached at the surface, implying that the surface of the sample is prone to cracking. The following stresses have been calculated and shown in the figure:  $\sigma_R$  is the radial stress,  $\sigma_{RZ}$  is the shear stress,  $\sigma_\theta$  is the hoop stress, and  $\sigma_Z$  is the longitudinal stress.

Figure 5-42 (a) shows the stress component distribution of the 25 mm flat die.  $\sigma_Z$  is the highest among them and it is approximately 50 MPa.  $\sigma_{RZ}$  is almost entirely below zero, which implies that this is a compressive stress and therefore does not contribute to the formation of surface cracks. Figure 5-42 (c) shows the stress component distribution of the zero-bearing die. When comparing Figure 5-42 (a) to (c), the results show that each stress component is very similar to its counterpart.  $\sigma_Z$  in Figure 5-42 (c) is also the highest close to the surface. Both the extrudates of the 25 mm flat die and zero-bearing die showed surface cracks at this speed and the size of the cracks were observed to be very similar. It is reasonable to conclude from the results that  $\sigma_Z$  is the main stress factor that causes the surface cracks. This observation is in agreement with the literature [50]. Figure 5-42 (b) and (d) show the stress component distribution of the 35 mm choked die and 12 mm choked die, respectively. The stress close to the surface for the 35 mm choked die was much smaller compared to the 25 mm flat die and the zero-bearing die. In fact, the stress components were either all negative at the surface or they had a relatively smaller value, which is the reason why no cracks were observed for the 35 mm choked die.  $\sigma_Z$  in Figure 5-42 (d) was also smaller when compared to that of the 25 mm flat die and the zero-bearing die, calculated to about 40 MPa at the surface, explaining why no surface cracks were observed for the 12 mm choked die at the same extrusion speed. However, at a higher extrusion speed of 36 mm/s, surface cracks were observed for the 12 mm choked die.

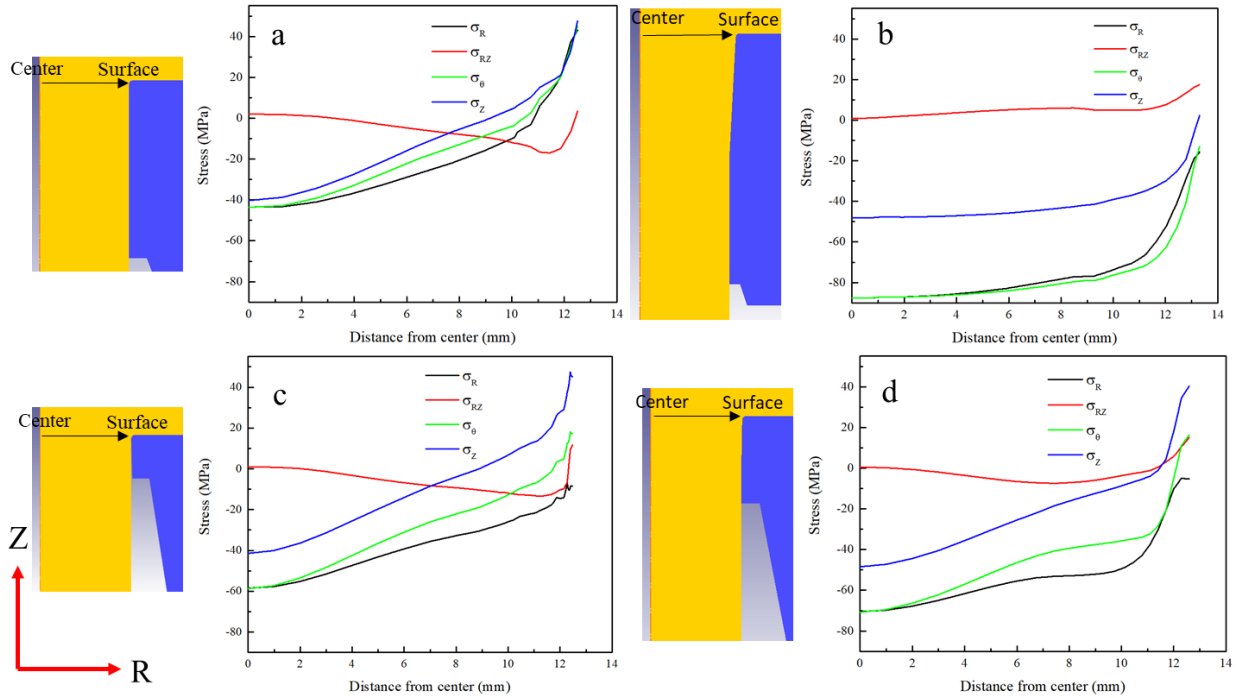


Figure 5-42 Model-predicted stress components from the center to the surface at the die corner at an extrusion speed of 26 mm/s for: (a) 25 mm flat die, (b) 35 mm choked die, (c) zero-bearing die, and (d) 12 mm choked die using the material A612 and a starting billet temperature of 500°C.

Figure 5-43 shows the corresponding temperature distribution across the billet from the center to the surface at die corner for different dies using A612 during extrusion at a speed of 26 mm/s. The temperature consistently rises from the billet's core to its surface due to material interaction with the die and intense deformation. Notably, the results show that the surface temperature of the 25 mm flat die and the zero-bearing die were nearly identical. These temperatures remain well below the solidus temperature, which is predicted to be around 570°C. Comparatively, the surface temperature of the 35 mm choked die and the 12 mm choked die were slightly higher, about 10°C, than that of the non-choked dies. However, even with the elevated temperature, the relatively lower  $\sigma_z$  stress at the die corner for the 12 mm choked die was

insufficient to induce surface cracks. The extrusion trials verify the numerical results, as surface cracks were only observed for the 12 mm choked die when the extrusion speed exceeded 36 mm/s, which induced a high enough stress at the surface to cause cracking.

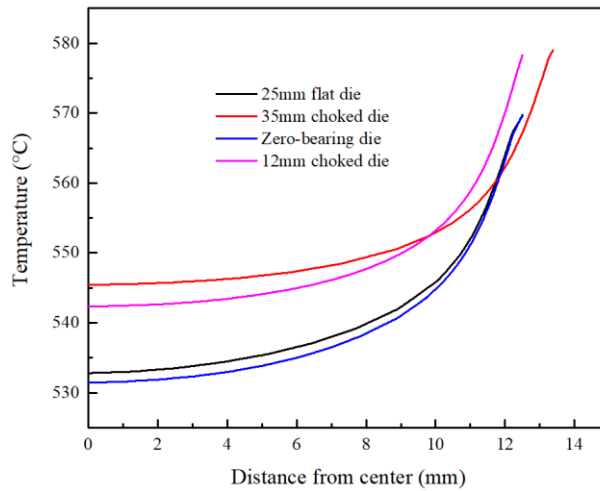


Figure 5-43 Model-predicted temperature distribution from the center to the surface of the billet at die corner for all die geometries using A612 at an extrusion speed of 26 mm/s.

Figure 5-44 (a-d) illustrates contour maps of  $\sigma_z$ , for the 25 mm flat, 35 mm choked, zero-bearing, and 12 mm choked dies using A612, respectively. Additionally, the temperature distribution is shown in a1-d1 for the corresponding dies. The results show that for the 25 mm flat and the zero-bearing dies, the stress is concentrated predominantly at the die corner. However, the zero-bearing die exhibits a larger region with the stress exceeding 15 MPa compared to the 25 mm flat die. The material right at the die front near the die corner has a sticking condition with the die. When the material just exits the die corner, the friction within the die bearing in the 25 mm flat die hinders material flow, which results in reduced displacement of the material compared to the material that has a sticking condition with the die. This contrasts with the zero-bearing die, where

material flow encounters no restriction when the material has moved past the die corner. In contrast, the results show that the stress contour patterns for the 35 mm choked die and the 12 mm choked die are completely different. In the case of the 35 mm choked die, the upper part of the die mainly exhibits compressive stress with a very small area showing lower tensile stress close to the die corner, while the lower part is under tension. Notably, only a minimal area exhibited stress values exceeding 15 MPa compared to the other three dies. For the 12 mm choked die, two stress concentration regions were observed along the bearing, i.e., one at the die corner and the other at the middle of the die bearing. In both regions the area where the stress was above 15 MPa was relatively small compared to the 25 mm flat and zero-bearing dies, again explaining why the choked die bearings are more resistant to cracking.

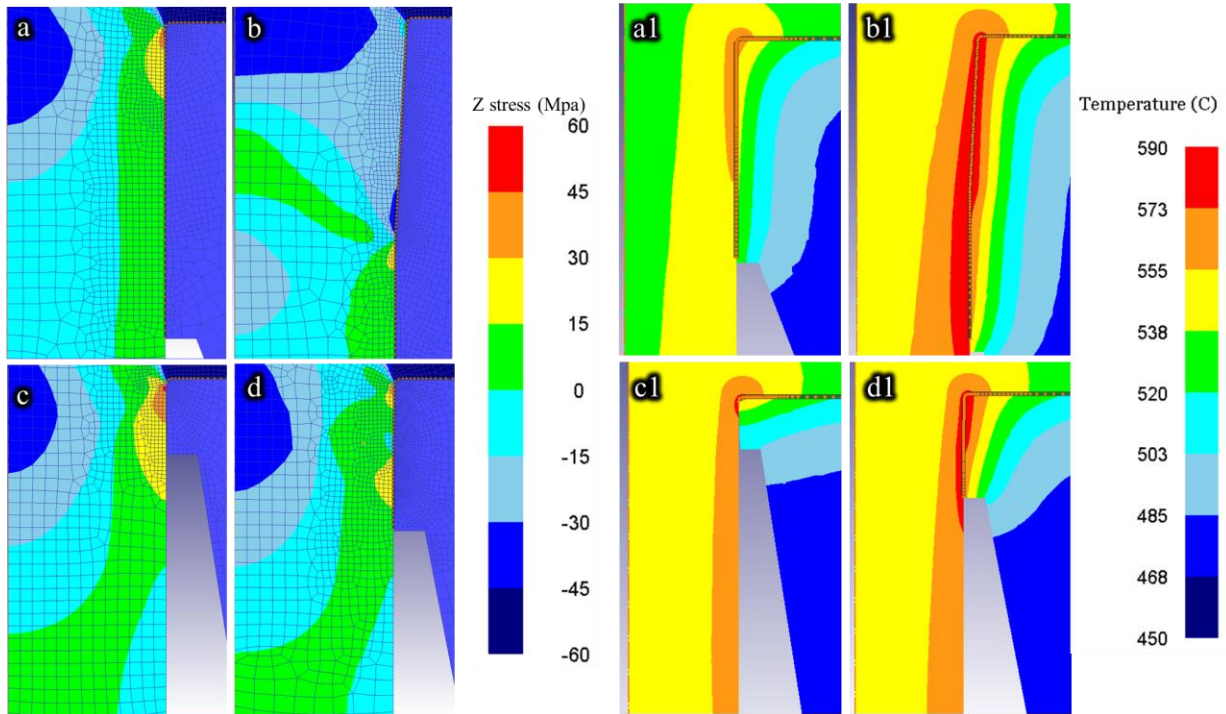


Figure 5-44 Model-predicted  $\sigma_z$  and temperature contour map at the die bearing region for the different die types using A612: the 25 mm flat die (a, a1), the 35 mm choked die (b, b1), the zero-bearing die (c, c1), and the 12 mm choked die (d, d1) at a stroke of 150 mm.

Figure 5-45 (a) provides insight into the distribution of  $\sigma_z$  along the die bearing for all four dies using A612. As identified in the contour maps, Figure 5-45 confirms that in the case of the 25 mm flat and zero-bearing dies, the highest stress point was at the die corner. In contrast, for the 12 mm choked die, which features a  $1^\circ$  choke angle, the stress concentration was still present at the die corner, but with a significantly reduced magnitude. A different trend was observed for the 35 mm choked die, which was characterized by a  $3^\circ$  choked angle. The maximum stress was moved away from the die corner to the middle of the die bearing, and its magnitude was lower than that observed in the other three dies. This outcome aligns with the stress contour map showcased in Figure 5-44.

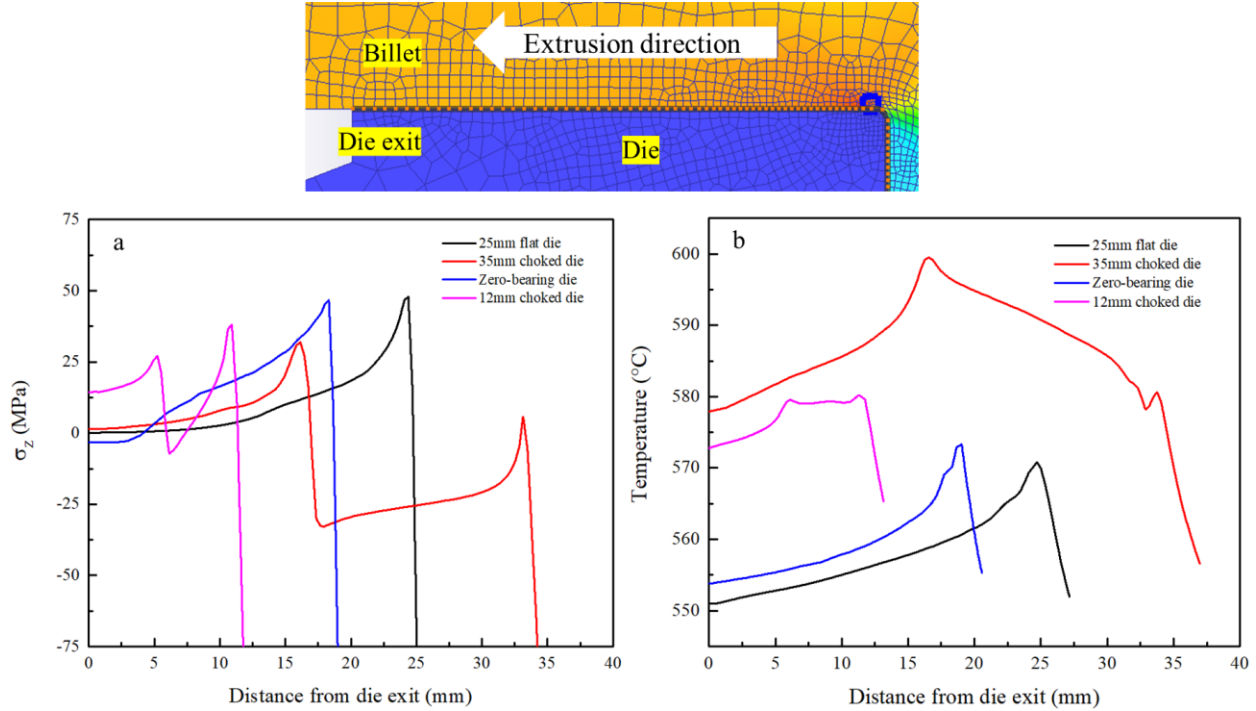


Figure 5-45 Model-predicted (a)  $\sigma_z$  and (b) temperature distribution along the die bearing for all four dies using A612 at the stroke of 150 mm at an extrusion speed of 26 mm/s.

Upon examining the temperature contour map shown in Figure 5-44 (a1-d1), it is evident that both the 25 mm flat and zero-bearing dies exhibited comparatively lower temperatures in the die bearing region, which contrasted with the choked dies. Clearly, the highest temperature was observed at the die corner for the 25 mm flat die and the zero-bearing die, while the temperature along the die bearing area was slightly elevated for the zero-bearing die when compared to the flat die. This distinction was also captured in Figure 5-45 (b). The explanation for this phenomenon is that even though friction at the die bearing generates heat concurrently, the die bearing of the 25 mm flat die absorbs a portion of the heat produced on the surface of the extrudates. In contrast, for the choked dies, the temperatures along the bearing were much higher and the temperature was observed to reach the solidus of the material. For the 12 mm choked die, the maximum temperature

occurred at the die corner, while the maximum temperature of the 35 mm choked die was observed at the middle of the die bearing. The results show that when the choke angle increases, the location of the maximum  $\sigma_Z$  and the maximum temperature shifts from the die corner to the middle of the die bearing. Additionally, an increase in the choke angle corresponds to a reduction in the maximum  $\sigma_Z$  while at the same time leading to an elevation in the peak temperature.

### 5.3.3 Stress and temperature conditions that lead to cracking

Figure 5-46 displays the model prediction for temperature and the corresponding  $\sigma_Z$  at the die corner at varying extrusion speeds all four dies with four dies (25 mm flat die, zero-bearing die, 12 mm choked die and 35 mm choked die) with an extrusion ratio of 17:1 and one die (12 mm flat die) with an extrusion ratio of 70:1 using A612. The colors used in the figure represent the surface morphology observed in the extrusion trials: **Green** signifies an absence of surface cracks, **Orange** indicates the presence of micro cracks, and **Red** denotes the visibility of surface cracks. The dash line is an approximate line that separates the areas where there are surface cracks and there are no surface cracks.

In each extrusion speed for die with an extrusion ratio of 17:1, data regarding the temperature and  $\sigma_Z$  values at the front, middle, and back of the extrusion are extracted through post-processing of the simulation results. In the case of the 35 mm choked die, the figure displays both temperature and  $\sigma_Z$  values at both the die corner and the middle of the die bearing. This is due to the behavior observed in this die, where both the maximum temperature and maximum  $\sigma_Z$  have shifted towards the middle of the die bearing. Notably, among all four dies, the highest stress is observed in both the 25 mm flat and zero-bearing dies. Micro cracks start to appear at approximately 563°C for the 25 mm flat die and around 570°C for the zero-bearing die. The temperature difference is because for the 25 mm flat die, the simulation data from the extrusion

speeds of 22 mm/s, 24 mm/s, 26 mm/s and 28 mm/s is plotted, while for the zero-bearing die, the simulation data from the extrusion speeds of 24 mm/s, 26 mm/s and 28 mm/s is plotted. In contrast, the 12 mm choked die exhibits relatively lower stress levels, and surface cracks only become visible at the back of the extrusion when the temperature reaches the solidus temperature. However, in the case of the 35 mm choked die, stress levels are significantly lower compared to the other three dies, especially the data at the bottom of the figure extracted from the die corner.

The surface cracks tend to occur at the up-right corner of the  $\sigma_z$ -temperature figure, where both the stress and temperature are relatively high compared to the lower left corner of the figure for all the dies except the 35 mm choked die. For the 35 mm choked die, although the temperatures reach the solidus temperature for some conditions, cracking is not initiated due to the lower stress. Therefore, both the temperature and the stress state play important roles in surface crack formation. The dash line separates the areas where there were observed and micro cracks (above the line) and the region where no surface cracks were observed (below the line). The relationship between the stress and temperature is provided in Equation 5-15:

$$\sigma_z = -0.65T + 422.6 \quad 5-15$$

For each extrusion speed for die with an extrusion ratio of 70:1, only the data regarding the temperature and  $\sigma_z$  values at the back of the extrusion are extracted through post-processing of the simulation as this is where observations were made. For the extrusion trial without surface cracks, the predicted stress and temperature falls below the dash line, while for the extrusion trial with surface cracks, the corresponding predicted stress and temperature are above the dash line.

However, for certain die except the 35 mm choked die, it is evident that stress levels alone do not reliably distinguish between scenarios with and without cracks. Instead, temperature



emerges as the more critical factor contributing to the occurrence of surface cracks. Therefore, the temperature is used as a criterion to help construct the extrusion limit diagram.

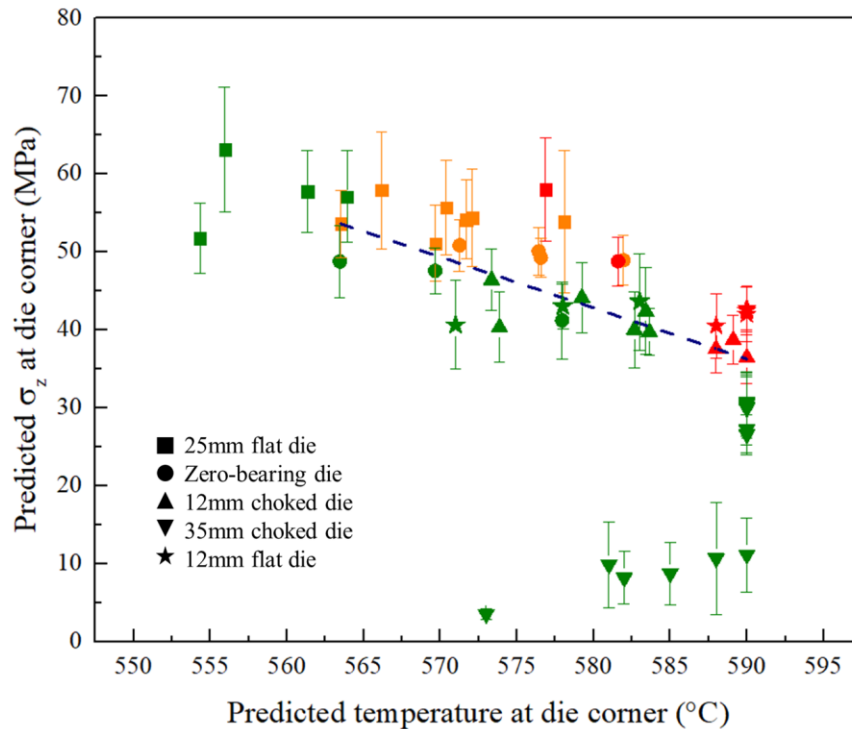


Figure 5-46 Model predicted temperature and corresponding  $\sigma_z$  at the die corner at varying extrusion speeds for all die geometries for A612. For die with ER=17:1 the data at the front, middle and back of the extrusion is extracted. For die with ER=17:1 the data at the front, middle and back of the extrusion is extracted. Different colors refer to the corresponding surface morphology observed in the extrusion trial with **Green** indicating no surface cracks, **Orange** indicating micro cracks, and **Red** indicating visible surface cracks. For the 35 mm choked die, both the data at the die corner and middle of the die bearing is plotted.

Figure 5-47 presents the model prediction for surface temperature using a homologous temperature so that alloys with different Cu levels and different solidus values could be compared on a similar graph. The corresponding  $\sigma_z$  at the die corner for varying extrusion speeds and all for

A612 and A613 using the 25 mm flat die with “■” representing A612 and “□” representing A613. As expected for both the materials the predicted stress is essentially the same but does decrease very slightly as the temperature increases. Referring to Figure 5-47, we can see that as we increase the temperature and get beyond  $\sim 0.95T_{\text{homologous}}$ , which is  $560.5^{\circ}\text{C}$  for A612 and  $553.9^{\circ}\text{C}$  for A613, surface cracks start to appear and become more pronounced as the surface temperature continues to increase. The extrusion speeds do not show an obvious effect on the predicted stress because when the extrusion speed increases, the stress decreases due to the rise in temperature.

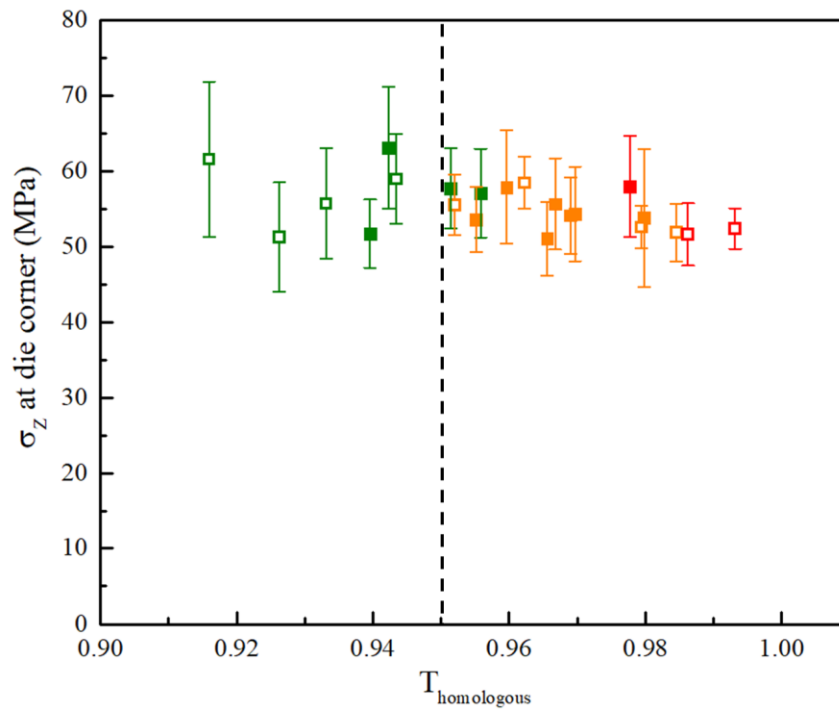


Figure 5-47 Model predicted  $\sigma_z$  at the die corner and temperature (corresponding homologous temperature) at the die corner at varying extrusion speeds for materials A612 and A613 using the 25 mm flat die.

## 5.4 Construction of extrusion limit diagram (ELD)

The extrusion limit diagram (ELD) graphically defines a workable area (i.e., the process window) for an extrusion process. It can be used to provide guidelines for the choice of extrusion parameters that can be used for a given alloy. To illustrate how they are developed, we can use the A612 material and the 25 mm flat die as an example to explain this method.

Utilizing the verified mathematical model of the extrusion process as a foundation, a series of numerical simulations for different extrusion speeds and starting billet temperatures were run first. For uniformity, the tooling temperature remained constant across all billet temperature variations. Specifically, the container, feeder, and die were maintained at a temperature of 480°C, while the dummy block was set to 450°C. We selected three distinct billet temperatures, namely, 475°C, 500°C, and 525°C. At each of these billet temperatures, we opted for three different extrusion speeds. A concise summary of the chosen billet temperatures and extrusion speeds for the simulations can be found in Table 5-4.

Table 5-4 Extrusion simulations run for 25 mm flat die (A612) to construct ELD.

Billet temperature (°C)	475	500	525
Extrusion speed (mm/s)	20, 25, 30	15, 20, 25	10, 15, 20

After completing the simulations, the maximum surface temperature achieved during each extrusion simulation was retrieved at a 150 mm stroke through post-processing in DEFORM™ 2D. These results were then plotted in Figure 5-48. Notably, it becomes apparent that, under specific starting billet temperatures, the anticipated maximum temperature at a 150 mm stroke

exhibits a linear correlation with the extrusion speed. Should a particular maximum temperature be desired at the same stroke and starting billet temperature, one can determine the required extrusion speed using this linear relationship.

For the purposes of this study, three maximum temperature thresholds were selected to represent conditions where surface cracking may occur, serving as upper processing limits: the solidus temperature, solidus temperature minus 10°C, and solidus temperature minus 20°C. In the context of A612, these three maximum temperature limits equate to 570°C, 580°C, and 590°C, respectively. For each of these temperature limits, the necessary extrusion speeds were calculated and summarized at various starting billet temperatures, as detailed in Table 5-5.

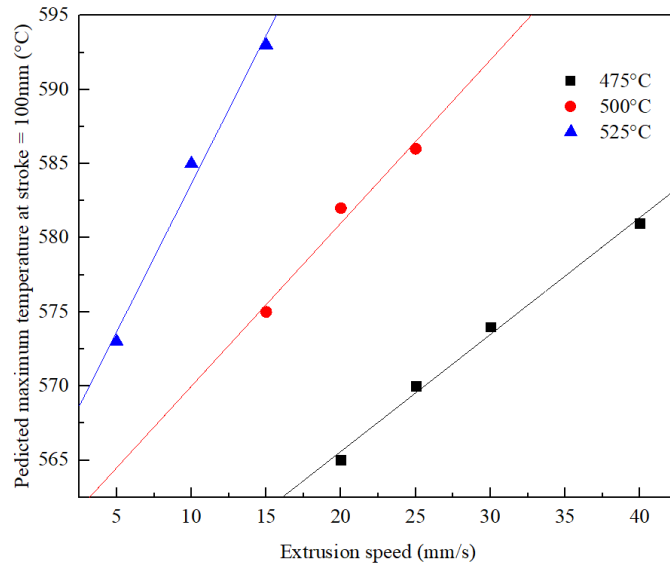


Figure 5-48 Model predicted relationship between the predicted maximum temperature and the extrusion speed at the stroke of 150 mm for different starting billet temperature by 25mm flat die using A612. The symbols represent the model predicted.

Table 5-5 Model predicted maximum extrusion speed (to reach the temperature limit) for different starting billet temperature by 25mm flat die using A612 material.

Temperature limit Billet temperature	570°C	580°C	590°C
475°C	21 mm/s	32 mm/s	43 mm/s
500°C	11 mm/s	19 mm/s	28 mm/s
525°C	7 mm/s	11 mm/s	15 mm/s

To determine the maximum achievable speed for a specific extrusion press under a given initial billet temperature, the breakthrough load was extracted for each combination of billet temperature and extrusion speed as outlined in Table 5-4 through post-processing in DEFORM™ 2D. Subsequently, the material's mean effective strain rate was calculated for each extrusion condition using the following Equation 5-16:

$$\dot{\epsilon} = \frac{6VD_C^2 \tan \alpha}{(D_C^3 - D_E^3)} 2 \ln \frac{D_C}{D_E} \quad 5-16$$

Where V is the extrusion speed,  $D_C$  is the container diameter,  $D_E$  is the extrusion profile diameter,  $\alpha$  is the dead-metal zone semi angle, which is taken as 45° in this case. With the mean effective strain rate and the billet temperature, the mean flow stress of the material at certain billet temperature and extrusion speed can be calculated by the material constitutive model in 5.1.2.2. Then the relationship of the breakthrough loads, and the corresponding calculated material mean flow stresses can be plotted as Figure 5-49. Their relationship exhibits a linear relationship. When the extrusion press maximum force is known, because the maximum breakthrough load is equal to the extrusion press maximum force, the corresponding mean flow stress can be obtained by using

the linear relationship from Figure 5-49, and then the mean effective strain rate for each billet temperature can be got by using the constitutive model again. Finally, the extrusion speed can be calculated by Equation 5-16.

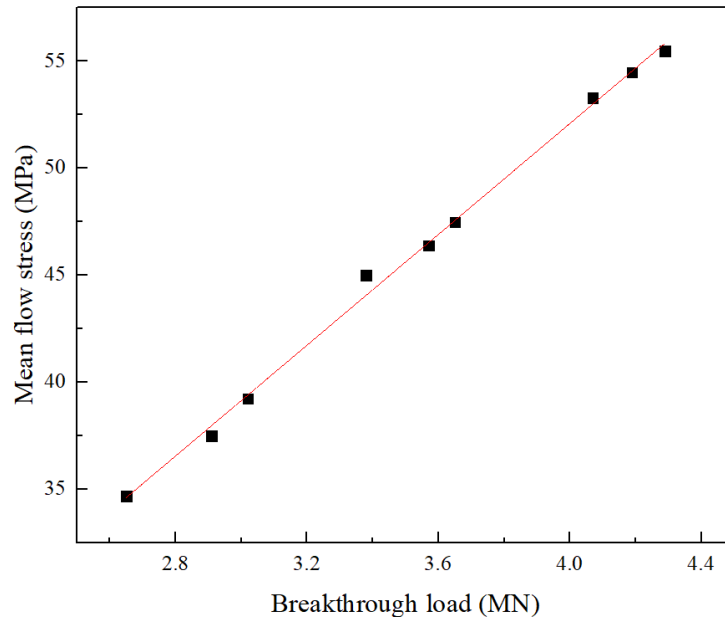


Figure 5-49 Model predicted linear relationship between the breakthrough load and the corresponding mean flow stress at the same starting billet temperatures and extrusion speeds by 25mm flat die using A612 material.

The obtained temperature limit and extrusion press limit can be graphically represented in Figure 5-50. In this figure, you can observe two distinctive black curves, one solid and the other dashed, which signify the theoretical extrusion press limitations. For instance, if the billet temperature is set at 440°C and the extrusion speed exceeds 30 mm/s, the extrusion press becomes incapable of extruding the material due to the force required surpassing the press limit of 600MPa. Meanwhile, three colored lines are utilized to depict the temperature constraints.

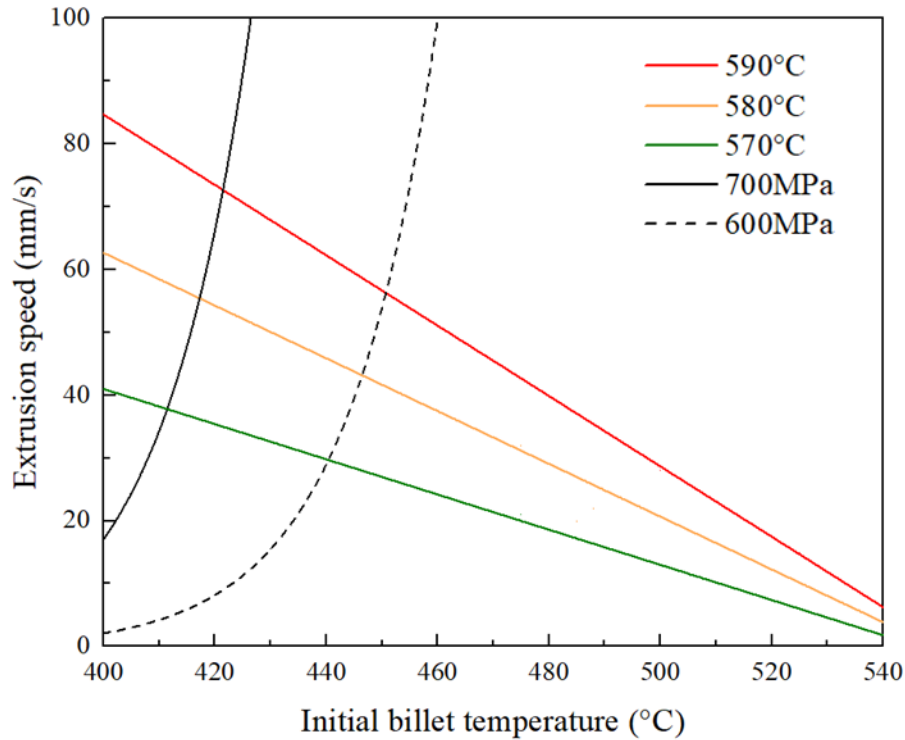


Figure 5-50 Model predicted ELD for an A612 alloy using the 25 mm flat die with the temperature limits: 590°C (Red line), 580°C (Orange line), and 570°C (Green line) and the extrusion press limits: 700MPa (Black solid curve) and 600MPa (Black dash curve)

Because the same constitutive model was used for all the three materials with Cu, the load limit curves on the ELD for the same die would be the same, and they can be adjusted according to the extrusion press capacity.

#### 5.4.1 Effect of die geometries on ELD

In order to identify the temperature thresholds associated with distinct surface conditions for each die, a visual and SEM examination of the extrusion profile surfaces was conducted with the samples from the back of the extrusion process for all four dies. Subsequently, the surface morphology conditions were summarized in Table 5-6. These surface conditions were categorized

into three types: good surface conditions, surfaces displaying microcracks, and surfaces exhibiting visible cracks, represented by the colors green, orange, and red in Table 5-6, respectively.

Table 5-6 Summary of the extrusion profile surface quality at different extrusion speeds for different die geometries with the same extrusion ratio 17:1 and the same material A612, **Green** means good surface, **Orange** means micro crack, **Red** means visible cracks.

25 mm flat die		Zero-bearing die		12 mm choked die		35 mm choked die	
Billet T(°C)	Speed (mm/s)	Billet T(°C)	Speed (mm/s)	Billet T (°C)	Speed (mm/s)	Billet T	Speed (mm/s)
485	20	511	24	513	26	491	22
488	22	491	26	480	28	511	24
483	24	488	28	484	34	493	26
479	26	516	28	527	30	503	28
495	28	502	30	511	27	489	30
495	31	488	29	515	28	500	32
		501	27	503	38	487	34
		492	29	485	36	503	36
				489	32	492	38
						499	40

The corresponding starting billet temperature and extrusion speed of these data were plotted in the ELD constructed using the method mentioned above, as shown in Figure 5-51. In



the figures the temperatures at which the same surface morphology conditions start showing are different for different die geometries.

For 25 mm flat die, micro cracks occur when the temperature is higher than 570°C. For zero-bearing die, micro cracks appear when the temperature reaches 580°C. The cracking phenomenon is a little different for the 12 mm choked die. There is no micro crack below the solidus temperature and, and visible cracks almost show at all the speed at which the maximum temperature reached the solidus temperature. For the 35 mm choked die, there is no surface crack at any extrusion speed within the limit of the extrusion press, which is 40 mm/s.

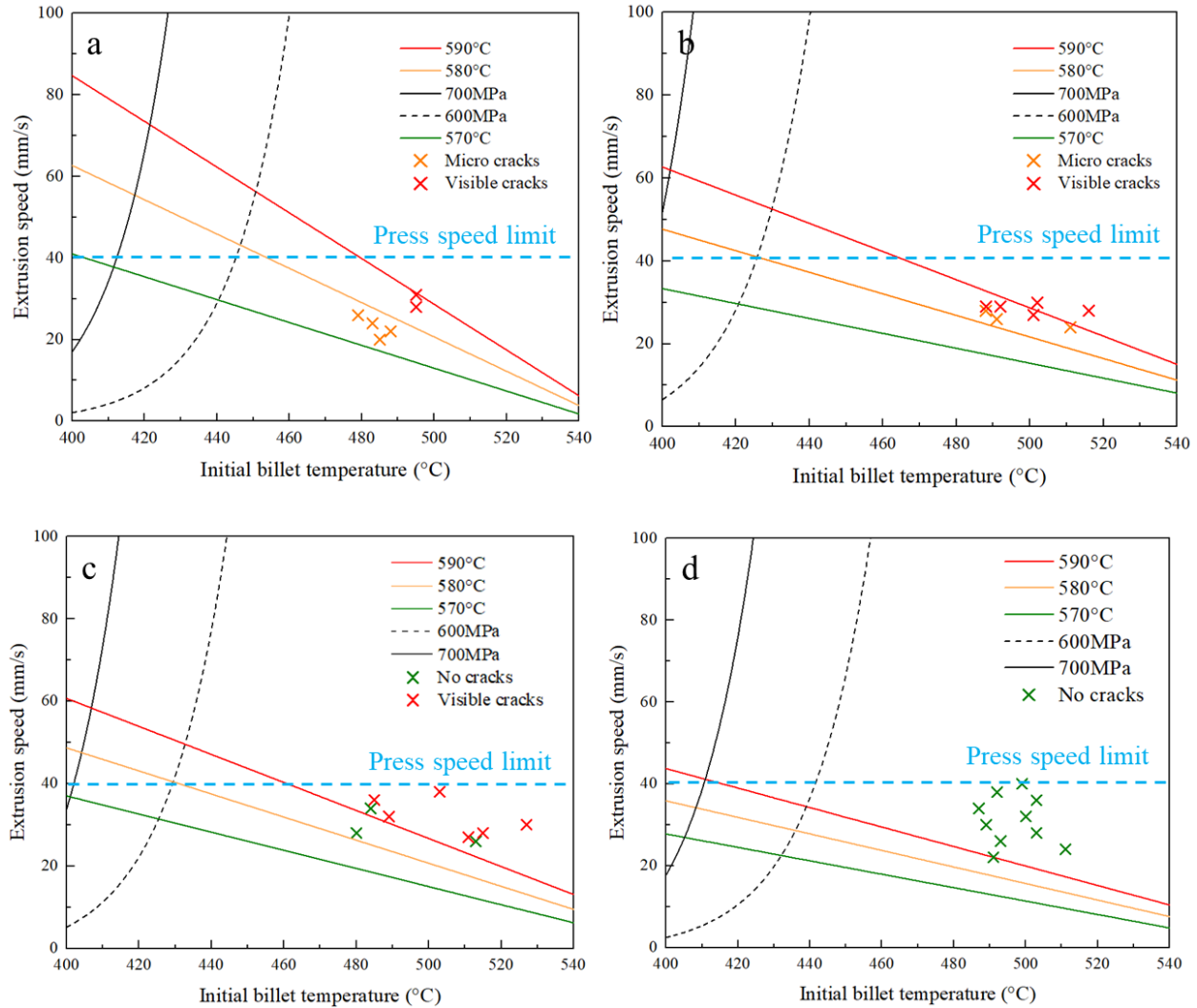


Figure 5-51 Model predicted ELDs (lines and curves) and experimental observations of surface morphology conditions (“x”) for A612 at the back of the extrudate with the same extrusion ratio of 17:1 for different die geometries: (a) 25m flat die, (b) zero-bearing die, (c) 12 mm choked die, and (d) 35 mm choked die.

Referring to Figure 5-52, it becomes evident that the die geometry has a significant impact on surface cracking behavior. Notably, the 35 mm choked die demonstrates the capacity to extrude the material at exceptionally high temperature, even exceeding the solidus temperature, yet it exhibits no observable surface cracks were evident. Likewise, the 12 mm choked die also exhibits

the ability to extrude the material at a higher temperature, reaching the solidus temperature before surface cracks emerge, in comparison to the 25 mm flat die and the zero-bearing die. This is because the choked angle in both the 35 mm choked die and the 12 mm choked die lowers the stress experienced by the material when the material passes through the die corner, which is analyzed in 5.3.2.

Conversely, the 25 mm flat die is constrained to run at the lowest extrusion speed because of the higher stress experienced as the material passes the die corner, and the 570°C temperature defined the effective working area and extruding the samples at a temperature greater than that would result in cracks. Considering that the zero-bearing die shows similar surface crack sizes as the 25 mm flat die at the same extrusion speed and the similar longitudinal stress at the die corner, it is reasonable to use the same temperature to define the working area. The results showed that the working area for the 25 mm flat die was slightly smaller than the zero-bearing die because of the friction force acting at the 25 mm flat die bearing, which results in more heat generated at the extrudate surface. The excess temperature causes the crack temperature to be reached faster for the 25 mm flat die compared to the zero-bearing die during the extrusion process. Nonetheless, the extrudates produced using the 25 mm flat die and the zero-bearing die show similar extrudability such that the material can only be extruded at a limited extrusion speed, while the choked dies greatly improved the extrudability of the samples at high extrusion speed without any apparent surface defects, which improves the extrusion efficiency.

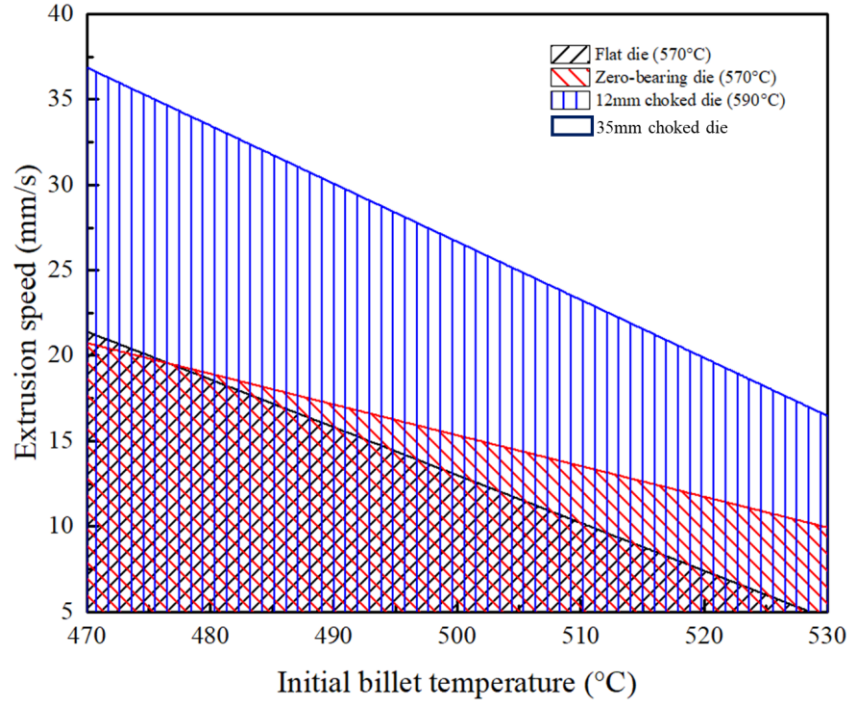


Figure 5-52 The effect of die geometries on the extrudability of A612 with black represents 25 mm flat die, red represents zero-bearing die, blue represents 12 mm choked die, and white represents the 35 mm choked die.

### 5.4.2 Effect of extrusion ratio on ELD

To investigate the impact of the extrusion ratios on the extrudability, the ELDs for two flat dies using A612 material featuring distinct extrusion ratios were constructed: 70:1 and 17:1. Initially, the surface characteristics of the extruded materials generated by these two dies were assessed. The surface morphology evaluations for both dies are presented in Table 5-7, where “green” designates a favorable surface condition, “orange” denotes surfaces with microcracks, and “red” signifies surfaces displaying visible cracks. Then the ELDs of the two flat dies with different extrusion ratios are constructed using the method described in the beginning of Section 5.4.

Referring to Figure 5-53, both figure (a) and (b) feature temperature limit lines, where red corresponds to 590°C, orange to 580°C, and green to 570°C. A notable observation when comparing the lines that represent the same temperature in Figure 5-53 (a) and (b) is the substantial difference in the area beneath these lines. Specifically, the die with an extrusion ratio of 17:1 exhibits a significantly larger area below the temperature limit lines compared to the die with an extrusion ratio of 70:1. This discrepancy indicates that, with a smaller extrusion ratio, the temperature escalates more rapidly during the extrusion process when both the initial billet temperature and tooling temperature remain constant.

In Figure 5-53 (a) and (b), the extrusion data derived from trials with both dies is graphically represented by “x” marks. These points are color-coded, with “red” indicating the presence of visible surface cracks, “orange” signifying the occurrence of microcracks, and “green” denoting a desirable, smooth surface finish. For both dies, the extrudates exhibit visible cracks before the temperature reaches the solidus point, while microcracks start to appear around the orange line, which corresponds to a temperature of 580°C. However, in the case of the die with an extrusion ratio of 70:1, when the temperature during the extrusion process remains below 580°C, the extrudates display a good surface finish. Conversely, for the die with an extrusion ratio of 17:1, none of the extrudates achieve a good surface quality.

Considering that the microcracks on the extrudates at an extrusion speed of 20 mm/s are already quite minimal, it can be believed that the temperature threshold at which no surface cracks are observed should be approximately aligned with the green line, which represents a temperature of 570°C.

Table 5-7 Summary of the extrusion profile surface quality at different extrusion speeds for the two flat dies with different extrusion ratio and the same material A612, “Green” means good surface, “Orange” means micro crack, “Red” means visible cracks.

25 mm flat die (Extrusion ratio = 17:1)		12 mm flat die (Extrusion ratio = 70:1)	
Actual billet T (°C)	Speed(mm/s)	Billet T (°C)	Speed(mm/s)
485	20	500	4
488	22	500	5
483	24	500	6
479	26	500	7
495	28	500	8
495	31	500	9
		500	10

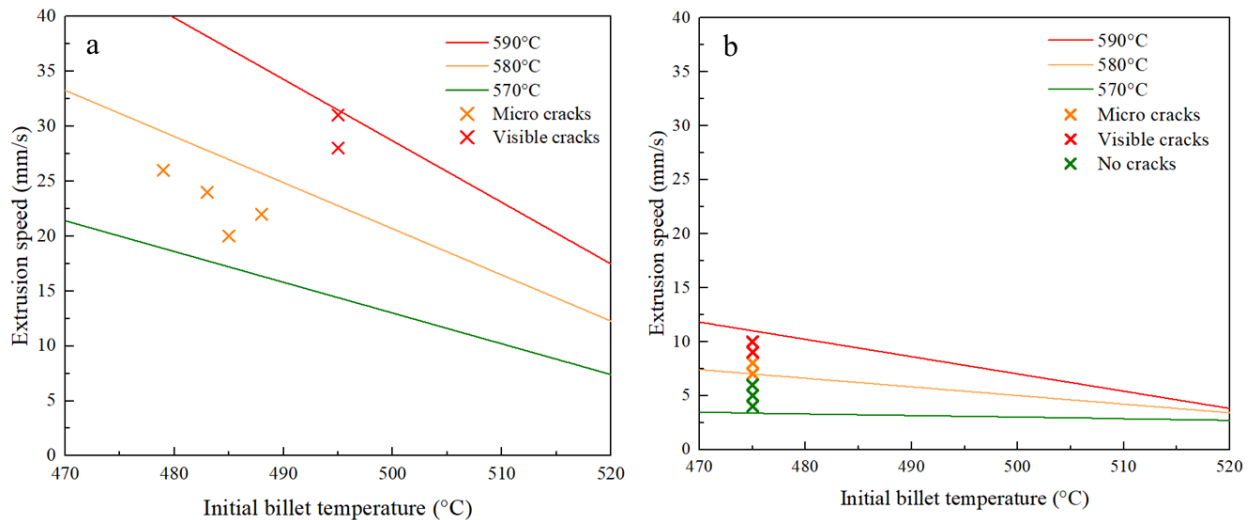


Figure 5-53 Model predicted ELDs (lines) and experimental observations of surface morphology conditions (“x”) extruded by flat dies using A612 with extrusion ratio of (a)17:1 and (b)70:1.

Figure 5-54 provides a comparison of temperature limit lines, specifically those situated below which surface cracks do not manifest. These lines are derived from the green line in Figure 5-53 (a) and the orange line in Figure 5-53 (b). The trend that emerges is quite evident: as the extrusion ratio increases, the limit line descends, resulting in a reduced workable area beneath the line. Consequently, the maximum achievable extrusion speed, without incurring surface cracks, diminishes at specific starting billet temperatures.

This phenomenon can be attributed to the fact that, under the same starting billet temperatures, higher extrusion ratios subject the material to greater stress and strain rates, generating more heat in the process. Consequently, the temperature escalates more rapidly, surpassing the critical crack temperature sooner than in the case of dies with lower extrusion ratios.

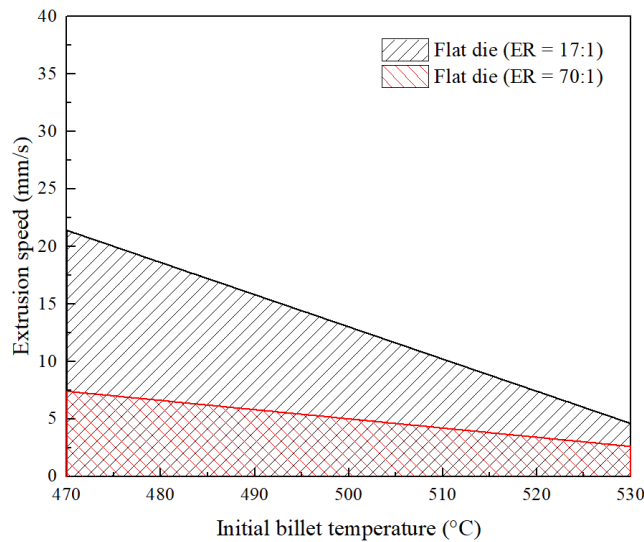


Figure 5-54 Model-predicted ELD for A612 extruded using the flat die showing the effect of extrusion ratio with the black-shaded area representing the workable area of the die with an extrusion ratio of 17:1 and the red-shaded area representing the workable area of the die with an extrusion ratio of 70:1.

### 5.4.3 Effect of Cu content on ELD

To explore the influence of Cu content on the material's extrudability, extrusion trials using both A612 and A613 materials through a 25 mm flat die were conducted. Subsequently, the surface morphology conditions of the extrudates were examined, as presented in Table 5-8. Here, "green" indicates a desirable no crack surface condition, "orange" signifies surfaces featuring microcracks, and "red" represents surfaces exhibiting visible cracks.

Figure 5-44 illustrates the ELDs, constructed as outlined in Section 5.4. These ELDs are distinguished by colored lines representing temperature limits ("red" denoting the solidus temperature, "orange" indicating a temperature 10°C lower than the solidus temperature, and "green" signifying a temperature 20°C lower than the solidus temperature). Additionally, two load limit curves are on the graph. Extrusion trial data is designated by the symbol "x" in the graph. It is important to note that the load limit remains consistent for both materials since the same constitutive model is employed in the simulation.

The extrusion trial data falls within the range of billet temperatures spanning from 480°C to 520°C for both materials. Notably, for both materials, when the temperature falls between the red line and the orange line, visible cracks become apparent on the extrudates. Furthermore, when the temperature resides between the orange line and the green line, microcracks are observed on the extrudates. In the case of A613, when the initial billet temperature is lower than the green line, it results in the attainment of a favorable extrudate surface. From these observations, it can be concluded that the temperature during the extrusion process exerts a significant influence on the surface crack condition.



Table 5-8 Summary of the extrusion profile surface quality of A612 and A613 at different extrusion speeds extruded by 25 mm flat die, **green** means good surface, **orange** means micro crack, **red** means visible cracks.

A612 (0.6% Cu)		A613 (0.9% Cu)	
Actual billet T (°C)	Speed(mm/s)	Actual billet T (°C)	Speed(mm/s)
495	20	486	5
491	22	492	10
493	24	512	15
486	26	505	20
495	28		
495	31		

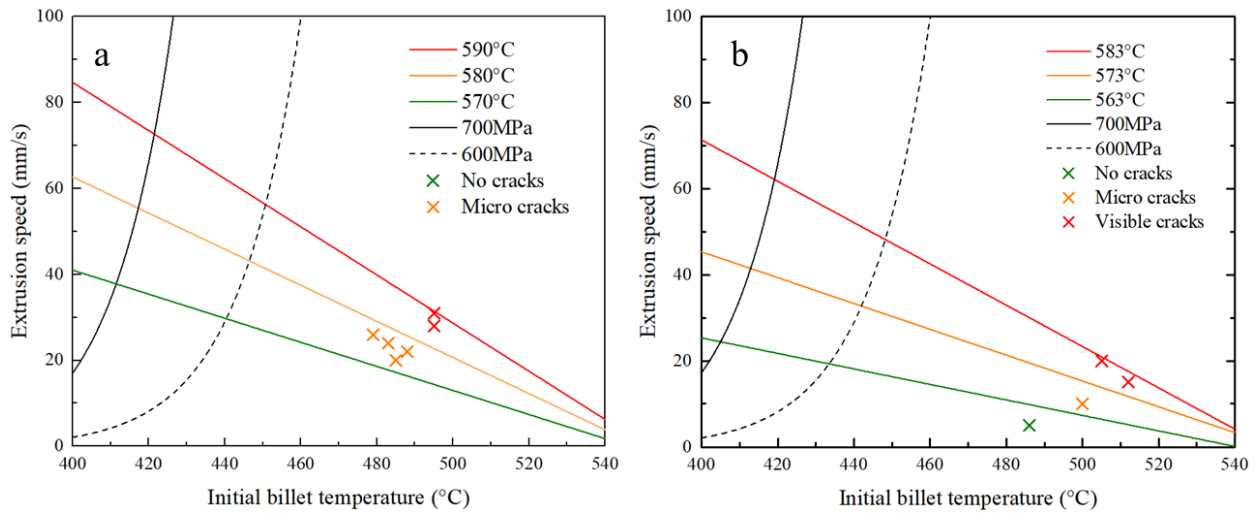


Figure 5-55 Model predicted ELDs (lines and curves) and experimental observations of surface morphology conditions (“x”) at the back of the extrudates extruded using the 25 mm flat die with: (a) material A612 and (b) material A613.

For all three materials, the temperature limit line was established as the solidus temperature minus 20°C, below which it is anticipated to achieve a favorable extrudate surface during the extrusion process. A comparative analysis of these limits is presented in Figure 5-56. It is evident that as the Cu content rises, the temperature limit line descends. The progressive increase in Cu content within the AA6xxx alloy results in a reduction of the available extrusion workspace.

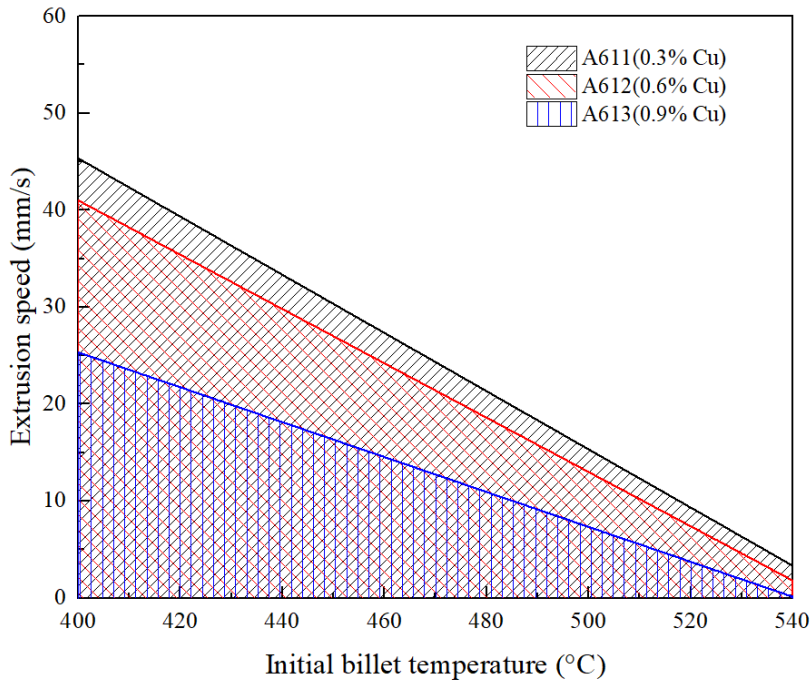


Figure 5-56 Comparison of the model predicted ELD for three materials with different Cu additions extruded using the 25 mm flat die.

## Chapter 6 Summary, Conclusions, and Future Work

### 6.1 Summary

The main objective of this research was to understand how the additions of Cu to AA6xxx alloys, die geometries and extrusion ratios affect the extrudability of the material using both experiments and numerical modelling. The modelling work has been done using a commercial FEM code DEFORM<sup>TM</sup> to calculate the temperature and stress distribution during the extrusion process.

The research focuses on AA6xxx materials with three Cu additions: A611 with 0.3% Cu, A612 with 0.6% Cu, and A613 with 0.9% Cu. The dies with different extrusion ratios are 12 mm flat die with an extrusion ratio of 70:1 and 25 mm flat die with an extrusion ratio of 17:1. The dies with the same extrusion ratio (17:1) but different die bearing geometries are: 25 mm flat die, zero-bearing die, 12 mm choked die (1° choked angle), and 35 mm choke die (3° choked angle).

The experimental work consisted of conducting three extrusion trials using the fully instrumented extrusion press at Rio Tinto Alcan's Arvida facility located in Jonquiere, Quebec. Subsequently samples were prepared from the extrudates for surface and microstructure examination. Three extrusion trials were performed in total. First is on the effect of extrusion ratios. One billet temperature (500°C) and a series of extrusion speed were chosen for both the 12 mm flat die and the 25 mm flat die. The second trial is on the effect of die geometries and one billet temperature (500°C), and a series of similar extrusion speeds were chosen for each die geometry. The third trial is on the effect of Cu contents and one billet temperature (500°C), and different extrusion speeds were chosen for the A612 and A613 materials by using the 25 mm flat die and

the 35 mm choked die. The surface cracking morphology, roughness, and microstructure of the extrudates were examined using SEM, 3D profilometer and microscope respectively.

For the modelling part, mesh sensitivity, friction coefficient justification and model verification were conducted first. Then the numerical simulation was used to help construct the extrusion limit diagrams to see how the extrusion ratios, die geometries and the Cu contents affect the extrudability. The stress and the temperature in the extrusion process using different die were also analyzed.

## **6.2 Conclusions**

Experimental work and numerical modelling have been successfully utilized in this research to investigate the effect of extrusion ratios, die geometry and Cu contents on surface morphology and surface cracking. The following conclusions can be drawn from the analysis that has been done:

### *Effect of die geometry*

1. For the trials using dies with different die bearing geometries and the same extrusion ratio, the 25 mm flat die and zero-bearing die exhibit surface cracks at relatively lower extrusion speeds, with cracks appearing from the middle of the extrusion process at a certain speed. In contrast, the 12 mm choked die shows cracks at higher extrusion speeds, while the 35 mm choked die avoids surface cracks even at the maximum extrusion speed of 40 mm/s. Die bearing geometry, in particular the introduction of a choke angle, had a significant effect on the tendency for cracking with the critical speed increasing in the sequence flat and zero bearing, 12 mm choke and 35 mm choke.

2. Numerical modelling indicates that the introduction of a choke angle changes the stress state at the die corner: the flat and zero bearings introduce a tensile stress along the extrusion direction, the 12 mm choke results in a reduced tensile stress and the 35 mm choke produces a compressive stress covering most of die bearing.
3. Although a simple bar was extruded for different die geometries, the stress and temperature conditions that lead to surface cracking is summarized, which provides guidance for more complex extrusion.

#### *Effect of Cu additions*

1. Hot compression tests reveal that the flow stress curves of AA6xxx alloys with different Cu additions do not exhibit a significant difference. DSC tests show that as the Cu content increases, the solidus temperature of the material increases slightly.
2. For the trials for the materials with different Cu additions, when using a flat die, materials with higher Cu content exhibited larger surface cracks at the same extrusion speed, whereas the samples produced using a choked die did not show any surface cracks, regardless of the Cu content.
3. A higher Cu content in AA6xxx alloys results in a relatively thick PCG layer when using the 35 mm choked and 25 mm flat dies.
4. Numerical modelling shows that when the temperature during the extrusion process reaches  $\sim 0.95T_{\text{homologous}}$ , surface cracks (micro cracks) start to occur regardless of the die geometries, which provides guidance for more complex extrusion.

#### *Effect of extrusion ratios*

1. By examining the extrudate surfaces from the dies with different extrusion ratios, it can be seen that with higher extrusion ratio, the extrudates tend to show surface cracks at a much lower extrusion speed.
2. The simulation results show that at the same extrusion speed, the predicted maximum temperature at die corner is much higher for the smaller extrusion ratio due to the more severe deformation. However, the predicted stress that the material experiences is not significantly different for both dies.

#### *Extrusion limit diagram*

1. Extrusion limit diagrams were constructed based both the experimental and simulation results using the temperature as a criterion.
2. The extrusion limit diagrams show the effect of die geometry, Cu content, and extrusion ratio on the extrudability. Choked die, low Cu content and high extrusion ratio are preferred regarding extrudability.

### **6.3 Future Work**

1. For all extrusion trials, only one starting billet temperature was chosen for this work. The constructed extrusion limit diagrams are also based on limited extrusion trial data and work for a small range of billet temperatures. In order to expand the extrusion limit diagram and provide guidance for choosing extrusion parameters over a large range of billet temperatures, trials at varying billet temperatures need to be done.
2. This study focused on the surface morphology of the extrudates extruded by dies with different extrusion ratios, dies with different die bearing geometries, and materials with

different Cu additions. However, the influence of these parameters on the mechanical properties of the extrudates has not been studied yet.

3. The effect of Cu on the intermetallic particles and dispersoids in the microstructure also needs to be studied systematically in the future to help understand the microstructure changes in the extrudates.

## References

- [1] Corporate Average Fuel Economy Britannica, (n.d.). <https://www.britannica.com/topic/Corporate-Average-Fuel-Economy> (accessed October 31, 2022).
- [2] Aluminium applications – Transport, (n.d.). <https://www.aluminiumleader.com/application/transport/> (accessed October 31, 2022).
- [3] 2015 North American Light Vehicle Aluminum Content Study.pdf, (n.d.).
- [4] Aluminium, (n.d.). <https://www.riotinto.com/products/Aluminium> (accessed October 31, 2022).
- [5] M.W. mwayland@mlive.com, 2015 F-150: Ford's aluminum pickup exceeds 700-pound weight reduction, increases performance, Mlive. (2014). [https://www.mlive.com/auto/2014/07/2015\\_f-150\\_fords\\_alumimnum\\_pic.html](https://www.mlive.com/auto/2014/07/2015_f-150_fords_alumimnum_pic.html) (accessed October 31, 2022).
- [6] CA95065611.pdf, (n.d.). <https://www.autonews.com/assets/PDF/CA95065611.PDF> (accessed October 31, 2022).
- [7] N. Hashimoto, Application of Aluminum Extrusions to Automotive Parts, (n.d.).
- [8] R.S. Rana, R. Purohit, S. Das, Reviews on the Influences of Alloying elements on the Microstructure and Mechanical Properties of Aluminum Alloys and Aluminum Alloy Composites, 2 (2012) 7.
- [9] G. Djukanovic, Aluminium Alloys in the Automotive Industry: a Handy Guide, Alum. Insid. (2019). <https://aluminiuminsider.com/aluminium-alloys-automotive-industry-handy-guide/> (accessed November 1, 2022).
- [10] P. Mukhopadhyay, Alloy Designation, Processing, and Use of AA6XXX Series Aluminium Alloys, Int. Sch. Res. Not. 2012 (2012) e165082. <https://doi.org/10.5402/2012/165082>.
- [11] I. Iwayama, T. Kuwabara, Y. Nakai, Y. Takaki, S. Kitamura, H. Saito, 6056 Aluminum Alloy Wire for Automotive Fasteners, (n.d.) 5.
- [12] Aluminium Alloy - Commercial Alloy - 6082 - T6~T651 Plate, (n.d.). [https://www.aalco.co.uk/datasheets/Aluminium-Alloy\\_6082-T6~T651\\_148.ashx](https://www.aalco.co.uk/datasheets/Aluminium-Alloy_6082-T6~T651_148.ashx) (accessed November 1, 2022).
- [13] A through process model for high strength Al-Mg-Si-Cu extrusion alloys.pdf, (n.d.).
- [14] G. Al-Marableh, Effect of heat treatment on the distribution and volume fraction of Mg<sub>2</sub>Si in structural aluminum alloy 6063, Met. Sci. Heat Treat. 48 (2006) 205–209. <https://doi.org/10.1007/s11041-006-0071-5>.
- [15] O. Reiso, Extrusion of AlMgSi Alloys, (n.d.) 15.
- [16] Direct Chill (DC) casting [SubsTech], (n.d.). [https://www.substech.com/dokuwiki/doku.php?id=direct\\_chill\\_dc\\_casting](https://www.substech.com/dokuwiki/doku.php?id=direct_chill_dc_casting) (accessed November 1, 2022).
- [17] C. Liu, Microstructure evolution during homogenization and its effect on the high temperature deformation behaviour in AA6082 based alloys, University of British Columbia, 2017. <https://doi.org/10.14288/1.0360654>.



- [18] P.I. Sarafoglou, A. Serafeim, I.A. Fanikos, J.S. Aristeidakis, G.N. Haidemenopoulos, Modeling of Microsegregation and Homogenization of 6xxx Al-Alloys Including Precipitation and Strengthening During Homogenization Cooling, *Materials*. 12 (2019) 1421. <https://doi.org/10.3390/ma12091421>.
- [19] X. Dong, S. Amirkhanlou, S. Ji, Formation of strength platform in cast Al–Si–Mg–Cu alloys, *Sci. Rep.* 9 (2019) 9582. <https://doi.org/10.1038/s41598-019-46134-7>.
- [20] M. Puchnin, O. Trudonoshyn, O. Prach, F. Pešlová, Comparison of ABI Technique and Standard Methods in Measuring Mechanical Properties of Aluminium Al-alloys, *Manuf. Technol.* 16 (2016) 600–607. <https://doi.org/10.21062/ujep/x.2016/a/1213-2489/MT/16/3/600>.
- [21] J. Li, Q. An, S. Wu, F. Li, S. Lü, W. Guo, Relationship of Mg<sub>2</sub>Si morphology with Mg<sub>2</sub>Si content and its effect on properties of in-situ Mg<sub>2</sub>Si/Al–Cu composites, *J. Alloys Compd.* 808 (2019) 151771. <https://doi.org/10.1016/j.jallcom.2019.151771>.
- [22] X. Zhu, H. Yang, X. Dong, S. Ji, The effects of varying Mg and Si levels on the microstructural inhomogeneity and eutectic Mg<sub>2</sub>Si morphology in die-cast Al–Mg–Si alloys, *J. Mater. Sci.* 54 (2019) 5773–5787. <https://doi.org/10.1007/s10853-018-03198-6>.
- [23] J. Asensio-Lozano, B. Suárez-Peña, G.F. Vander Voort, Effect of Processing Steps on the Mechanical Properties and Surface Appearance of 6063 Aluminium Extruded Products, *Materials*. 7 (2014) 4224–4242. <https://doi.org/10.3390/ma7064224>.
- [24] L. Sweet, S.M. Zhu, S.X. Gao, J.A. Taylor, M.A. Easton, The Effect of Iron Content on the Iron-Containing Intermetallic Phases in a Cast 6060 Aluminum Alloy, *Metall. Mater. Trans. A.* 42 (2011) 1737–1749. <https://doi.org/10.1007/s11661-010-0595-6>.
- [25] S. Kumar, P.S. Grant, K.A.Q. O’Reilly, Evolution of Fe Bearing Intermetallics During DC Casting and Homogenization of an Al–Mg–Si Al Alloy, *Metall. Mater. Trans. A.* 47 (2016) 3000–3014. <https://doi.org/10.1007/s11661-016-3451-5>.
- [26] T. Gao, Y. Bian, K. Hu, K. Zhao, W. Zhang, X. Liu, Structural and morphological evolution of Fe–rich phases in Al–xMg–6Si–4Fe alloys, *Results Mater.* 3 (2019) 100036. <https://doi.org/10.1016/j.rinma.2019.100036>.
- [27] METALLURGY OF HEAT TREATMENT AND GENERAL PRINCIPLES OF PRECIPITATION HARDENING\*, (n.d.) 66.
- [28] S.G. Shabestari, H. Moemeni, Effect of copper and solidification conditions on the microstructure and mechanical properties of Al–Si–Mg alloys, *J. Mater. Process. Technol.* 153–154 (2004) 193–198. <https://doi.org/10.1016/j.jmatprotec.2004.04.302>.
- [29] D.J. Chakrabarti, D.E. Laughlin, Phase relations and precipitation in Al–Mg–Si alloys with Cu additions, *Prog. Mater. Sci.* 49 (2004) 389–410. [https://doi.org/10.1016/S0079-6425\(03\)00031-8](https://doi.org/10.1016/S0079-6425(03)00031-8).
- [30] T. Sheppard, *Extrusion of Aluminium Alloys*, Springer US, Boston, MA, 1999. <https://doi.org/10.1007/978-1-4757-3001-2>.
- [31] Y. Birol, The effect of homogenization practice on the microstructure of AA6063 billets, *J. Mater. Process. Technol.* 148 (2004) 250–258. <https://doi.org/10.1016/j.jmatprotec.2004.01.056>.

- [32] W. Yuna, Z. Jianfeng, L. Hengcheng, W. Yongjin, W. Yuping, Effect of Homogenization Temperature on Microstructure and Conductivity of Al-Mg-Si-Ce Alloy, *J. Mater. Eng. Perform.* 25 (2016) 2720–2726. <https://doi.org/10.1007/s11665-016-2121-5>.
- [33] Y. Sun, D.R. Johnson, K.P. Trumble, P. Priya, M.J.M. Krane, Effect of Mg<sub>2</sub>Si Phase on Extrusion of AA6005 Aluminum Alloy, (n.d.) 5.
- [34] S. Ji, W. Yang, F. Gao, D. Watson, Z. Fan, Effect of iron on the microstructure and mechanical property of Al–Mg–Si–Mn and Al–Mg–Si diecast alloys, *Mater. Sci. Eng. A.* 564 (2013) 130–139. <https://doi.org/10.1016/j.msea.2012.11.095>.
- [35] L. Lodgaard, N. Ryum, Precipitation of dispersoids containing Mn and/or Cr in Al–Mg–Si alloys, *Mater. Sci. Eng. A.* 283 (2000) 144–152. [https://doi.org/10.1016/S0921-5093\(00\)00734-6](https://doi.org/10.1016/S0921-5093(00)00734-6).
- [36] R. Hu, T. Ogura, H. Tezuka, T. Sato, Q. Liu, Dispersoid Formation and Recrystallization Behavior in an Al-Mg-Si-Mn Alloy, *J. Mater. Sci. Technol.* 26 (2010) 237–243. [https://doi.org/10.1016/S1005-0302\(10\)60040-0](https://doi.org/10.1016/S1005-0302(10)60040-0).
- [37] Y. Han, K. Ma, C. Wang, H. Nagaumi, Precipitation behavior of dispersoids in Al-Mg-Si-Cu-Mn-Cr alloy during homogenization annealing, (n.d.) 8.
- [38] I. Sadeghi, M. Wells, S. Esmaili, Modeling homogenization behavior of Al-Si-Cu-Mg aluminum alloy, *Mater. Des.* 128 (2017). <https://doi.org/10.1016/j.matdes.2017.05.006>.
- [39] G. Xue, G. Zhong, S. Lin, H.-T. Li, X. Gui, L. Zhang, Study on Microstructure and Mechanical Properties of Al-Mg-Si-Cu Aluminium Alloy with High Ductility, *MATEC Web Conf.* 326 (2020) 03003. <https://doi.org/10.1051/mateconf/202032603003>.
- [40] P.K. Saha, *Aluminum Extrusion Technology*, ASM International, 2000.
- [41] Y. Mahmoodkhani, M.A. Wells, N. Parson, W.J. Poole, Numerical modelling of the material flow during extrusion of aluminium alloys and transverse weld formation, *J. Mater. Process. Technol.* 214 (2014) 688–700. <https://doi.org/10.1016/j.jmatprotec.2013.09.028>.
- [42] Z. Peng, T. Sheppard, A study on material flow in isothermal extrusion by FEM simulation, *Model. Simul. Mater. Sci. Eng.* 12 (2004) 745–763. <https://doi.org/10.1088/0965-0393/12/5/001>.
- [43] M. Schikorra, L. Donati, L. Tomesani, A. Tekkaya, Microstructure analysis of aluminum extrusion: Grain size distribution in AA6060, AA6082 and AA7075 alloys, *J. Mech. Sci. Technol.* 21 (2007) 1445–1451. <https://doi.org/10.1007/BF03177357>.
- [44] S. Ngermbamrung, Y. Suzuki, N. Takatsuji, K. Dohda, Investigation of surface cracking of hot-extruded AA7075 billet, *Procedia Manuf.* 15 (2018) 217–224. <https://doi.org/10.1016/j.promfg.2018.07.212>.
- [45] T. Funazuka, K. Dohda, N. Takatsuji, K. Takano, N. Sukunthakan, Effect of Temperature on Surface Cracking Defects in AA7075 Hot Extrusion, *Key Eng. Mater.* 926 (2022) 409–415. <https://doi.org/10.4028/p-6bfd8v>.
- [46] Z. Peng, T. Sheppard, Study of surface cracking during extrusion of aluminium alloy AA 2014, *Mater. Sci. Technol.* 20 (2004) 1179–1191. <https://doi.org/10.1179/026708304225022016>.
- [47] T. Sheppard, Temperature and speed effects in hot extrusion of aluminium alloys, *Met. Technol.* 8 (1981) 130–141. <https://doi.org/10.1179/030716981803276009>.

- [48] A.F. Arif, A.K. Sheikh, S. Qamar, M. Raza, K. Al-Fuhaid, PRODUCT DEFECTS IN ALUMINUM EXTRUSION AND ITS IMPACT ON OPERATIONAL COST, 2002.
- [49] Y. Wang, G. Zhao, X. Chen, X. Xu, Cracking behavior and prediction criterion of spray-deposited 2195 Al–Li alloy extrusion profile, *Int. J. Adv. Manuf. Technol.* 120 (2022) 5969–5984. <https://doi.org/10.1007/s00170-022-09103-5>.
- [50] X. Duan, X. Velay, T. Sheppard, Application of finite element method in the hot extrusion of aluminium alloys, *Mater. Sci. Eng. A.* 369 (2004) 66–75. <https://doi.org/10.1016/j.msea.2003.10.275>.
- [51] C. Bertoli, Optimization of Hybrid Extrusion Dies with Internal Cooling Channels, (n.d.) 183.
- [52] M.P. Clade, T. Sheppard, Extrusion limit diagrams containing structural and topological information for AA 6063 aluminium alloy, *Mater. Sci. Technol.* 9 (1993) 313–318. <https://doi.org/10.1179/mst.1993.9.4.313>.
- [53] J.H. Kim, J.T. Yeom, J.K. Hong, S.Y. Shim, S.G. Lim, N.K. Park, Effect of scandium on the hot extrudability of 7075 aluminum alloy, *Met. Mater. Int.* 16 (2010) 669–677. <https://doi.org/10.1007/s12540-010-0823-z>.
- [54] L. Donati, L. Tomesani, The effect of die design on the production and seam weld quality of extruded aluminum profiles, *J. Mater. Process. Technol.* 164–165 (2005) 1025–1031. <https://doi.org/10.1016/j.jmatprotec.2005.02.156>.
- [55] S. Bai, G. Fang, J. Zhou, Construction of three-dimensional extrusion limit diagram for magnesium alloy using artificial neural network and its validation, *J. Mater. Process. Technol.* 275 (2020) 116361. <https://doi.org/10.1016/j.jmatprotec.2019.116361>.
- [56] R.Y. Lapovok, M.R. Barnett, C.H.J. Davies, Construction of extrusion limit diagram for AZ31 magnesium alloy by FE simulation, *J. Mater. Process. Technol.* 146 (2004) 408–414. <https://doi.org/10.1016/j.jmatprotec.2003.12.003>.
- [57] M. Barnett, J. Yao, C. Davies, Extrusion limits for AZ alloys with Al contents <3%, Deakin University, 2003. [https://dro.deakin.edu.au/articles/conference\\_contribution/Extrusion\\_limits\\_for\\_AZ\\_alloys\\_with\\_Al\\_contents\\_3\\_/20545275/1](https://dro.deakin.edu.au/articles/conference_contribution/Extrusion_limits_for_AZ_alloys_with_Al_contents_3_/20545275/1) (accessed November 2, 2022).
- [58] D.H. Lee, Y.J. Kim, S.-H. Kim, B.G. Moon, S.H. Park, Extrusion limit diagram of AZ91–0.9Ca–0.6Y–0.5MM alloy and effects of extrusion parameters on its microstructure and mechanical properties, *J. Magnes. Alloys.* 10 (2022) 3447–3458. <https://doi.org/10.1016/j.jma.2021.06.002>.
- [59] C. Zhang, C. Wang, R. Guo, G. Zhao, L. Chen, W. Sun, X. Wang, Investigation of dynamic recrystallization and modeling of microstructure evolution of an Al–Mg–Si aluminum alloy during high-temperature deformation, *J. Alloys Compd.* 773 (2019) 59–70. <https://doi.org/10.1016/j.jallcom.2018.09.263>.
- [60] H. Liao, Y. Wu, K. Zhou, J. Yang, Hot deformation behavior and processing map of Al–Si–Mg alloys containing different amount of silicon based on Gleebe-3500 hot compression simulation, *Mater. Des.* 1980–2015. 65 (2015) 1091–1099. <https://doi.org/10.1016/j.matdes.2014.08.021>.
- [61] I. Schindler, P. Kawulok, V. Očenášek, P. Opěla, R. Kawulok, S. Rusz, Flow Stress and Hot Deformation Activation Energy of 6082 Aluminium Alloy Influenced by Initial Structural State, *Metals.* 9 (2019) 1248. <https://doi.org/10.3390/met9121248>.

- [62] S. Liu, Q. Pan, H. Li, Z. Huang, K. Li, X. He, X. Li, Characterization of hot deformation behavior and constitutive modeling of Al–Mg–Si–Mn–Cr alloy, *J. Mater. Sci.* 54 (2019) 4366–4383. <https://doi.org/10.1007/s10853-018-3116-4>.
- [63] *Crystallography and Crystal Defects*, 3rd Edition | Wiley, Wiley.Com. (n.d.). <https://www.wiley.com/en-us/Crystallography+and+Crystal+Defects%2C+3rd+Edition-p-9781119420163> (accessed November 1, 2022).
- [64] Y. Xu, H. Nagaumi, Y. Han, G. Zhang, T. Zhai, The Deformation Behavior and Microstructure Evolution of a Mn- and Cr-Containing Al-Mg-Si-Cu Alloy During Hot Compression and Subsequent Heat Treatment, *Metall. Mater. Trans. A.* 48 (2017) 1355–1365. <https://doi.org/10.1007/s11661-016-3881-0>.
- [65] Q. Yang, D. Yang, Z. Zhang, L. Cao, X. Wu, G. Huang, Q. Liu, Flow behavior and microstructure evolution of 6A82 aluminium alloy with high copper content during hot compression deformation at elevated temperatures, *Trans. Nonferrous Met. Soc. China.* 26 (2016) 649–657. [https://doi.org/10.1016/S1003-6326\(16\)64154-7](https://doi.org/10.1016/S1003-6326(16)64154-7).
- [66] X. Wang, J. Qin, H. Nagaumi, R. Wu, Q. Li, The Effect of  $\alpha$ -Al(MnCr)Si Dispersoids on Activation Energy and Workability of Al-Mg-Si-Cu Alloys during Hot Deformation, *Adv. Mater. Sci. Eng.* 2020 (2020) e3471410. <https://doi.org/10.1155/2020/3471410>.
- [67] M. Wang, Z. He, X. Wu, C. Li, G. Li, Deformation simulation of low-temperature high-speed extrusion for 6063 Al alloy, *J. Cent. South Univ. Technol.* 17 (2010) 881–887. <https://doi.org/10.1007/s11771-010-0571-8>.
- [68] H. Yi, J. Ding, C. Ni, J. Dai, Y. Tang, X. Chen, K. Song, X. Xia, Hot compression deformation behavior and processing maps of Al–0.5Mg–0.4Si–0.1Cu alloy, *J. Mater. Res. Technol.* 19 (2022) 4890–4904. <https://doi.org/10.1016/j.jmrt.2022.07.027>.
- [69] H. Zhang, G. Chen, Q. Chen, F. Han, Z. Zhao, A physically-based constitutive modelling of a high strength aluminum alloy at hot working conditions, *J. Alloys Compd.* 743 (2018) 283–293. <https://doi.org/10.1016/j.jallcom.2018.02.039>.
- [70] K. Li, Q. Pan, R. Li, S. Liu, Z. Huang, X. He, Constitutive Modeling of the Hot Deformation Behavior in 6082 Aluminum Alloy, *J. Mater. Eng. Perform.* 28 (2019) 981–994. <https://doi.org/10.1007/s11665-019-3873-5>.
- [71] G.R. Johnson, W.H. Cook, A Constitutive Model And Data For Metals Subjected to Large Strains, High Strain Rates and High Temperatures, (n.d.) 7.
- [72] C.M. Sellars, W.J.McG. Tegart, Hot Workability, *Int. Metall. Rev.* 17 (1972) 1–24. <https://doi.org/10.1179/imtlr.1972.17.1.1>.
- [73] A. He, G. Xie, H. Zhang, X. Wang, A comparative study on Johnson–Cook, modified Johnson–Cook and Arrhenius-type constitutive models to predict the high temperature flow stress in 20CrMo alloy steel, *Mater. Des.* 1980-2015. 52 (2013) 677–685. <https://doi.org/10.1016/j.matdes.2013.06.010>.
- [74] R.O. Smerd, Constitutive behavior of aluminum alloy sheet at high strain rates, (n.d.) 201.
- [75] G. Geng, D. Ding, L. Duan, H. Jiang, A modified Johnson-Cook model of 6061-T6 Aluminium profile, *Aust. J. Mech. Eng.* 20 (2022) 516–526. <https://doi.org/10.1080/14484846.2020.1721966>.

- [76] S. Yang, L. Sun, H. Deng, G. Li, J. Cui, A modified Johnson-Cook model of AA6061-O aluminum alloy with quasi-static pre-strain at high strain rates, *Int. J. Mater. Form.* 14 (2021) 677–689. <https://doi.org/10.1007/s12289-020-01556-x>.
- [77] G. Kugler, M. Knap, H. Palkowski, Turk, Estimation of activation energy for calculating the hot workability properties of metals, (2004) 6.
- [78] J. Van De Langkruis, W.H. Kool, S. Van Der Zwaag, Modification of a Thermomechanical Model to Predict Constitutive Behavior of Al-Mg-Si Alloys, *J. Mater. Eng. Perform.* 15 (2006) 632–639. <https://doi.org/10.1361/105994906X150876>.
- [79] N. Haghdad, A. Zarei-Hanzaki, H.R. Abedi, The flow behavior modeling of cast A356 aluminum alloy at elevated temperatures considering the effect of strain, *Mater. Sci. Eng. A.* 535 (2012) 252–257. <https://doi.org/10.1016/j.msea.2011.12.076>.
- [80] K.P.V. Namburi, A.F. Kothasiri, V.S.M. Yerubandi, Modeling and simulation of Aluminum 1100 alloy in an extrusion process, *Mater. Today Proc.* 23 (2020) 518–522. <https://doi.org/10.1016/j.matpr.2019.05.398>.
- [81] L. Li, J. Zhou, J. Duszczuk, Prediction of temperature evolution during the extrusion of 7075 aluminium alloy at various ram speeds by means of 3D FEM simulation, *J. Mater. Process. Technol.* 145 (2004) 360–370. <https://doi.org/10.1016/j.jmatprotec.2003.09.003>.
- [82] Q. Lin, Y. Li, Z. Wang, Numerical Simulation of Hot Extrusion Process of 2519 Aluminum Alloy Tubes, *Mater. Mechancial Eng.* 31 (2007) 79–82.
- [83] Y. Mahmoodkhani, M.A. Wells, L.M. Grajales, W.J. Poole, N. Parson, Modelling Grain Deformation during Extrusion of AA3003 using the Finite Element Method, (n.d.) 6.
- [84] Y. Zhao, B. Song, J. Pei, C. Jia, B. Li, G. Linlin, Effect of deformation speed on the microstructure and mechanical properties of AA6063 during continuous extrusion process, *J. Mater. Process. Technol.* 213 (2013) 1855–1863. <https://doi.org/10.1016/j.jmatprotec.2013.05.006>.
- [85] C. Zhang, G. Zhao, Z. Chen, H. Chen, F. Kou, Effect of extrusion stem speed on extrusion process for a hollow aluminum profile, *Mater. Sci. Eng. B.* 177 (2012) 1691–1697. <https://doi.org/10.1016/j.mseb.2011.09.041>.
- [86] C. Zhang, G. Zhao, H. Chen, Y. Guan, F. Kou, Numerical simulation and metal flow analysis of hot extrusion process for a complex hollow aluminum profile, *Int. J. Adv. Manuf. Technol.* 60 (2012) 101–110. <https://doi.org/10.1007/s00170-011-3609-7>.
- [87] Y. Mahmoodkhani, J. Chen, M.A. Wells, W.J. Poole, N.C. Parson, The Effect of Die Bearing Geometry on Surface Recrystallization During Extrusion of an Al-Mg-Si-Mn Alloy, *Metall. Mater. Trans. A.* 50 (2019) 5324–5335. <https://doi.org/10.1007/s11661-019-05437-0>.
- [88] D. Wang, C. Zhang, C. Wang, G. Zhao, L. Chen, W. Sun, Application and analysis of spread die and flat container in the extrusion of a large-size, hollow, and flat-wide aluminum alloy profile, *Int. J. Adv. Manuf. Technol.* 94 (2018). <https://doi.org/10.1007/s00170-017-1127-y>.
- [89] Y. He, S. Xie, L. Cheng, G. Huang, Y. Fu, FEM simulation of aluminum extrusion process in porthole die with pockets, *Trans. Nonferrous Met. Soc. China.* 20 (2010) 1067–1071. [https://doi.org/10.1016/S1003-6326\(09\)60259-4](https://doi.org/10.1016/S1003-6326(09)60259-4).
- [90] C. Hao, Z. Guoqun, Z. Cunsheng, G. Yanjin, L. Hui, K. Funjun, Numerical Simulation of Extrusion Process and Die Structure Optimization for a Complex Aluminum Multicavity

- Wallboard of High-Speed Train, *Mater. Manuf. Process.* 26 (2011) 1530–1538. <https://doi.org/10.1080/10426914.2011.551950>.
- [91] Z. He, H. Wang, M. Wang, G. Li, Simulation of extrusion process of complicated aluminium profile and die trial, *Trans. Nonferrous Met. Soc. China.* 22 (2012) 1732–1737. [https://doi.org/10.1016/S1003-6326\(11\)61380-0](https://doi.org/10.1016/S1003-6326(11)61380-0).
- [92] Y. Birol, The effect of homogenization practice on the microstructure of AA6063 billets, *J. Mater. Process. Technol.* 148 (2004) 250–258. <https://doi.org/10.1016/j.jmatprotec.2004.01.056>.
- [93] Metal Forming and Finite Element Method.pdf, (n.d.).
- [94] DEFORM\_2D\_V10.2\_manual.pdf, (n.d.).
- [95] L. Donati, L. Tomesani, M. Schikorra, N.B. Khalifa, A.E. Tekkaya, Friction model selection in FEM simulations of aluminium extrusion, *Int. J. Surf. Sci. Eng.* 4 (2010) 27–41. <https://doi.org/10.1504/IJSURFSE.2010.029627>.
- [96] V. Sanabria, Friction in Long Bearing Channels During Multi-hole Extrusion of Aluminum Alloy: Experimental and Numerical Investigations, (n.d.).
- [97] H.S. Valberg, Analysis of Metal Flow of Aluminum through Long Choked Die Channels, *Key Eng. Mater.* 424 (2009) 145–152. <https://doi.org/10.4028/www.scientific.net/KEM.424.145>.
- [98] J.D. Bryant, The effects of preaging treatments on aging kinetics and mechanical properties in AA6111 aluminum autobody sheet, *Metall. Mater. Trans. A.* 30 (1999) 1999–2006. <https://doi.org/10.1007/s11661-999-0010-3>.
- [99] G.K.-H. Kolb, S. Scheiber, H. Antrekowitsch, P.J. Uggowitzer, D. Pöschmann, S. Pogatscher, Differential Scanning Calorimetry and Thermodynamic Predictions—A Comparative Study of Al-Zn-Mg-Cu Alloys, *Metals.* 6 (2016) 180. <https://doi.org/10.3390/met6080180>.
- [100] A. Woźnicki, B. Leszczyńska-Madej, G. Włoch, J. Madura, M. Bogusz, D. Leśniak, Homogenization of Extrusion Billets of a Novel Al-Mg-Si-Cu Alloy with Increased Copper Content, *Materials.* 16 (2023) 2091. <https://doi.org/10.3390/ma16052091>.
- [101] E.A. Starke, Aluminum Alloys: Thermomechanical Processing, in: K.H.J. Buschow, R.W. Cahn, M.C. Flemings, B. Ilshner, E.J. Kramer, S. Mahajan, P. Veyssi re (Eds.), *Encycl. Mater. Sci. Technol.*, Elsevier, Oxford, 2001: pp. 118–121. <https://doi.org/10.1016/B0-08-043152-6/00026-7>.
- [102] Y. demirci, O. Keles, Z. Zorlu, S. Ayan, K.  akır, Peripheral Coarse Grain Formation in High Silicon Containing AlMgSi Alloys, in: 2013.
- [103] A.R. Eivani, H.R. Jafarian, J. Zhou, Simulation of peripheral coarse grain structure during hot extrusion of AA7020 aluminum alloy, *J. Manuf. Process.* 57 (2020) 881–892. <https://doi.org/10.1016/j.jmapro.2020.07.011>.
- [104] H. Zhao, L. Sun, G. Zhao, J. Yu, F. Liu, X. Sun, Z. Lv, S. Cao, Abnormal grain growth behavior and mechanism of 6005A aluminum alloy extrusion profile, *J. Mater. Sci. Technol.* 157 (2023) 42–59. <https://doi.org/10.1016/j.jmst.2023.02.013>.
- [105] *Comprehensive Materials Processing*, Newnes, 2014.
- [106] S.Y. Chang, L.C. Tsao, T.Y. Li, T.H. Chuang, Joining 6061 aluminum alloy with Al–Si–Cu filler metals, *J. Alloys Compd.* 488 (2009) 174–180. <https://doi.org/10.1016/j.jallcom.2009.08.056>.

- [107]H.-M. Helwig, F. Garcia-Moreno, J. Banhart, A study of Mg and Cu additions on the foaming behaviour of Al–Si alloys, *J. Mater. Sci.* 46 (2011) 5227–5236. <https://doi.org/10.1007/s10853-011-5460-5>.
- [108]P. Goik, A. Schiffl, H.W. Höppel, Formation of Peripheral Coarse Grain in Thin-Walled Al–Mg–Si Extrusion Profiles, *Metall. Mater. Trans. A.* 54 (2023) 3940–3956. <https://doi.org/10.1007/s11661-023-07144-3>.
- [109]V. Aryshenskii, F. Grechnikov, E. Aryshenskii, Y. Erisov, S. Konovalov, M. Tepterev, A. Kuzin, Alloying Elements Effect on the Recrystallization Process in Magnesium-Rich Aluminum Alloy, *Materials.* 15 (2022) 7062. <https://doi.org/10.3390/ma15207062>.